X-ray studies of young stellar sources and their jets

Dissertation
zur Erlangung des Doktorgrades
des Fachbereichs Physik
der Universität Hamburg

vorgelegt von

Peter Christian Schneider

aus Hamburg

Hamburg
2011

Gutachter der Dissertation:	Prof. Dr. J. H. M. M. Schmitt Prof. Dr. M. Güdel
Gutachter der Disputation:	Prof. Dr. P. H. Hauschildt Prof. Dr. D. Horns
Datum der Disputation:	04.03.2011
Vorsitzender des Prüfungsausschusses:	Dr. R. Baade
Vorsitzender des Promotionsausschusses:	Prof. Dr. J. Bartels
Dekan der MIN Fakultät:	Prof. Dr. H. Graener

Zusammenfassung

Eine der wichtigsten Fragen der Astronomie ist seit den Anfängen der astrophysikalischen Forschung unbeantwortet: Wie entstehen Sterne? Während sich im letzten Jahrhundert ein grobes Bild der Sternentstehung herauskristallisiert hat, sind die Details immer noch vage und oft kontrovers diskutiert. Inzwischen wissen wir, dass Sterne nur in den dichtesten Regionen der Galaxien entstehen, in denen Wasserstoff hauptsächlich in Molekularform vorliegt. Die niedrige Temperatur in diesen Regionen erlaubt es, dass die Gravitation die Oberhand erhält und ein gravitativer Kollaps stattfinden kann. Die "Geburt" eines Sternes ist jedoch nicht einfach zu beobachten, weil das sichtbare und infrarote Licht von der Geburtswolke, aus der der Stern entstanden ist, stark absorbiert wird. Protostellare Jets durchdringen die Geburtswolke und sind daher oft einfacher zu beobachten als die Sterne selbst. Sie sind einer der ersten Hinweise auf einen neuen Stern.

Ein Gesamtbild der Sternentstehung und Sternentwicklung wird sich nur durch eine Kombination von Beobachtungen in verschiedenen Wellenlängenbereichen, insbesondere unter der Berücksichtigung der Röntgenemission von Protosternen und ihren Jets, ergeben. Die Röntgenemission stellt oft das hoch energetische Ende des verfügbaren Spektrums dar und ist häufig mit der Existenz von magnetischen Feldern verknüpft. Für die Röntgenemission von Protosternen wird direkt ein Magnetfeld benötigt, wohingegen für die Röntgenemission von protostellaren Jets indirekt ein Magnetfeld benötigt wird, da dieses für die Entstehung der Jets notwendig ist. Wie im folgenden dargelegt, beschäftigt sich meine Arbeit mit beiden Arten von Röntgenemission.

In meiner Arbeit wurde eine *Chandra* Beobachtung der Sternentstehungsregion Cepheus A (Cep A) auf Röntgenemission von Protosternen und protostellaren Jets untersucht. Sieben Protosterne mit $L_X \gtrsim 10^{30}$ erg/s wurden detektiert, eine von diesen Quellen war vorher unbekannt. Diese neue Quelle liegt auf der Verbindungslinie zwischen zwei H_2 Emissionsgebieten und könnte daher der Ursprung des zugehörigen protostellaren Jets sein. Nur der westliche Teil dieses Jets (HH 168) emittiert diffuse Röntgenstrahlung über eine Ausdehnung von 0.1 pc. Die Röntgenemission ist allerdings räumlich versetzt gegenüber der optischen Emission. Unter der Annahme, dass der Aufheizungsprozess zu einem früheren Zeitpunkt stattfand, kann diese räumliche Verschiebung durch die lange Abkühlungszeit des röntgenemittierenden Plasmas erklärt werden.

Die Studie über den röntgenemittierenden Jet von L1551 IRS 5 (HH 154) zeigte, dass die Röntgenemission im Wesentlichen stationär ist, wohingegen optische Emissionsgebiete eine klare Eigenbewegung zeigen. Für die Röntgenemission konnten keine signifikanten Veränderungen in den Spektraleigenschaften und in der Luminosität festgestellt werden. Die Nähe zur Zentralquelle und das konstante Erscheinungsbild der Röntgenemission von HH 154 könnte mit der räumlichen Struktur des Jets zusammenhängen, welche wiederum mit der Jetkollimierung zusammenhängt.

Die Röntgenmorphologie des Jets des klassischen T Tauri Sterns DG Tau ähnelt der des Jets von L1551 IRS 5. Mittels meiner Analyse von Daten aus zwei verschiedenen Zeiträumen konnte gezeigt werden, dass auch für die innere Komponente des Jets von DG Tau der Großteil der Röntgenemission nicht mit der stellaren Position übereinstimmt. Diese innere Jetkomponente zeigt, wie die innere Komponente von HH 154, keine detektierbare Eigenbewegung.

Röntgenabsorptionsspektroskopie stellt eine Möglichkeit zur Untersuchung von nicht selbst röntgenemittierendem und damit kühlem Material dar. Diese Methode wurde von mir genutzt, um die Staubscheibe des nahen und aktiven M Zwergs AU Mic zu untersuchen. Die oberen Grenzen der absorbierenden Säulendichten, die aus dieser Untersuchung abgeleitet wurden, belegen, dass der innere Teil der Scheibe arm an Gas und kleinen Staubteilchen ist.

Abstract

One of the most important questions in astronomy is unanswered since the beginning of astrophysics: How do stars form? While a coarse picture emerged within the last century, the details are still vague and often controversially debated. We now know that stars form only in the densest parts of galaxies, where hydrogen is mostly in its molecular form. The temperature in these regions is low enough to allow gravity to overcome all other stabilizing forces so that a gravitational collapse can happen. The "birth" of a star itself is not readily observable as the natal core from which the star forms absorbs most visible and even infrared light. One of the earliest signs of new stars are their jets which escape the core and which are often easier to observe than the protostar itself.

Understanding the various processes involved in star formation and stellar evolution requires a multi-wavelength effort. A complete picture will only emerge by combining results from various energy ranges including the X-ray emission from protostars and their jets. X-rays often trace the high energy end of the available spectrum and are associated with some kind of magnetic field. X-ray emission from protostars directly requires at least a small scale magnetic field while the X-ray emission from protostellar jets indirectly requires a large scale magnetic field for the generation of the jets themselves. My thesis deals with both kinds of X-ray emission as described in the following.

In my thesis a *Chandra* observation of the high-mass star formation region Cepheus A was analyzed for X-ray emission from the protostars and from the protostellar jets. Seven protostars were detected in X-rays with $L_X \gtrsim 10^{30}$ erg/s. One of these sources does not have a known counterpart at other wavelengths and is located on the connecting line between two H_2 emission complexes. Therefore, this new source might be the driving source of the associated protostellar outflow. Only the western part of this jet (HH 168) shows diffuse X-ray emission on scales of approximately 0.1 pc. Notably, the X-ray emission of HH 168 is displaced with respect to the current working surface and the individual concentrations of X-ray emission appear to trace the radio emission in this region. Assuming that the heating happened earlier in the outflow history of HH 168, the spatial displacement can be explained by the long cooling time of the X-ray emitting plasma as indicated by our analysis.

A detailed X-ray study of another protostellar jet showed persistent X-ray emission almost over a whole decade. Three high spatial resolution X-ray observations of the jet from L1551 IRS 5 (HH 154) revealed that the majority of the X-ray emission is always located close to the driving sources. Neither significant spectral nor luminosity changes could be detected. This contrasts the behavior of such objects as observed in the optical, where individual emission complexes clearly show proper motion. The proximity to the driving source and the apparent constancy of the X-ray emission might be related to the flow geometry as individual plasma blobs heated by internal shocks would retain detectable space velocity. Thus, the X-ray emission could be related to the collimation process of the jet.

The X-ray morphology of the classical T Tauri star DG Tau is very similar to that of HH 154. Analyzing high spatial resolution X-ray observations from two epochs, it could be shown that the majority of the X-ray emission related to DG Tau's jet is separated from the stellar position. This inner jet component remains close to the star without any detectable proper motion and therefore resembles the X-ray morphology of HH 154.

Another application of X-ray observations is X-ray absorption spectroscopy to investigate rather cool material. This method was applied to the X-ray spectrum of the nearby active M dwarf AU Mic to study its edge-on debris disk. Upper limits on the amount of individual elements locked in gas or small grains in the disk could be placed. These limits support a scenario in which the inner part of the disk is largely void of gas and small grains.

Contents

Part I

Introduction

1. Star formation

In principle, star formation is simple: Gravitational contraction of the material in the interstellar medium by seven orders in length increases its density by 21 orders of magnitude. The resulting gravitationally bound object has an interior temperature high enough to burn hydrogen and is commonly known as a star. For some reason, nature is not as simple as this and the details of this process are complex. In addition, observations of forming stars are hampered by their dense envelope making direct observations unfeasible. Nevertheless, the initial and final stages, i.e., the molecular cloud from which the star forms and the pre-main sequence stars, are readily observable. Fundamental problems of star formation relate to the fact that this process is very inefficient and only a fraction of the available matter condenses into stars although free fall times are much smaller than the age of our own galaxy. On the other extreme, rotation and magnetic fields would entirely inhibit star formation, if they were conserved during the collapse. Thus, it is of fundamental importance to understand the interplay of these ingredients.

This thesis deals with different stages of the star formation process in particular with protostellar jets. The general interest in jets is twofold: Firstly, they might play an important role in the star formation process itself and, secondly, they are often easier to observe than the forming star itself. The scene for these jets are forming stars and the processes involved in star formation are briefly introduced. The focus is on the formation of single, low-mass stars but note that the number of stars forming in multiple systems increases with stellar mass. The processes leading to the formation of these multiple systems might indeed be important for star formation in general. Also note, that it is still under debate, how high-mass star formation differs from low-mass star formation.

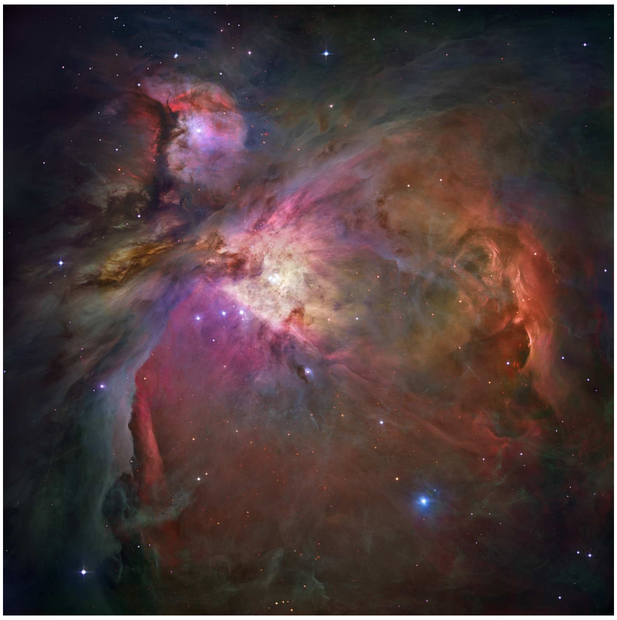

Figure 1.1: Composite image of the Orion nebula showing dust and gas illuminated by massive stars. The image was obtained by combining exposures in broad band filters and distinct emission lines from the HST ACS as well as the ESO MPI 2.2m La Silla WFI. Credits: NASA/ESA

1.1 Molecular clouds

Most stars form in transient structures called molecular clouds, where hydrogen is mostly in its molecular form in contrast to the inter-stellar medium (ISM) where it is mostly in its atomic form (Ferrière 2001). Isolated star-formation is very seldom and most stars form in clusters (Lada & Lada 2003; Adams & Myers 2001). The lifetimes of the molecular clouds are probably relatively short with estimated ages of $\lesssim 10$ Myr (Hartmann 2003). The nearest molecular cloud in which massive stars form is the Orion molecular cloud complex depicted in Fig. 1.1.

Compared to the ISM, molecular clouds have a high H_2 density of typically $10^4\,\mathrm{cm}^{-3}$ ($\approx$

Figure 1.2: The horsehead nebula located within the Orion molecular cloud. The illumination source σ Ori is located upwards in this picture. Reflected star light from the dust is shown in green, red is mainly hydrogen emission produced when the hydrogen ionized by the UV radiation recombines. The dark patches are due to the dust in the molecular cloud. Credits: ESO

10^{-20}g cm^{-3}) with a large spread. The spatial scales of these clouds range from less than 0.1 pc up to tens of parsec. They are usually hierarchically clumped with small structures of about 0.1 pc and 1 $M_\odot$ embedded in larger structures over a range of masses and sizes (several parsec and thousands of solar masses, Williams et al. 2000). The high density leads to a high cooling rate, and additionally, self-shielding and dust scattering prevent part of the background radiation to heat the molecules and grains, so that typical temperatures are usually as low as $10 - 20$ K (Larson 1985; Goldsmith 2001). Due to their dust content, molecular clouds are seen as dark clouds when viewed against a bright background such as distant stars in the galactic plane. This dust is also important for the formation of large amounts of molecules in these clouds. Whether background radiation or cosmic rays dominate the heating depends on the density, the spatial structure and the dust properties.

Although H_2 is the most abundant species in molecular clouds, it is not easily observed as its strongest transitions are in the mid-infrared and are not excited due to the cool temperatures. Therefore, CO and other molecular tracers are generally used to reveal the structure of the clouds. The observed distribution of clump masses is remarkably similar to the stellar initial mass function (IMF) and requires only scaling factors between 2 and 3 to match both distributions. However, observationally column densities instead of volume densities are measured and it remains unclear whether their interpretation is correct as discrepancies might also depend on the spatial scale (Shetty et al. 2010).

1.2 Fragmentation of the cloud and the formation of the core

In order to form stars, gravitation has to overcome the stabilizing forces at least in isolated parts of the molecular cloud. Early theories like the so-called Jeans' criterion (Jeans 1902), considered only gravitation and gas-pressure and did not include the effects of, e.g., turbulence or magnetic fields. Still, the Jeans' criterion is surprisingly successful and the predicted scales match that of more sophisticated theories within factors of only a few[1]. However, according to the Jeans' criterion, the observed masses of molecular clouds exceed the mass for gravitational collapse by far, and thus should form stars at a rate higher than generally observed (about a solar mass per year in the Milky Way, Robitaille & Whitney 2010). The fraction of gas actually forming stars in a molecular cloud is roughly between a few and 20 percent (Leroy et al. 2008; Evans et al. 2009); stars form only in the densest parts of the cloud and the majority of the gas remains in the filamentary structure.

Therefore, the cloud is in some way supported against collapse. Whether magnetic fields, radiation feedback or turbulence are most important for the regulation of the star forming efficiency is still unknown (see references in Price & Bate 2009). Su-

[1] The initial work of Jeans has been called the "Jeans swindle" due to some inconsistent assumptions (Binney & Tremaine 1987). However, a thorough treatment leads only to changes in the numerical constants by factors of a few so that the Jeans mass remains a good approximation (Larson 2003).

personic turbulence seems to be important at least on larger scales. It creates (isothermal) shocks compressing the gas to sufficiently dense regions for the gravitational collapse. On the other hand, the turbulence can also disrupt these regions again and might thereby regulate the star formation efficiency. This scenario, often referred to as gravoturbulent fragmentation, seems to be strengthened by numerical simulations which indeed show that supersonic turbulence can provide global support against the gravitational collapse. However, turbulence can also produce density enhancements in molecular clouds that allow for local collapse (Klessen et al. 2000). Although the kinetic energy of the turbulence is important on all scales in the cloud, the energy source of the turbulence is not clearly identified yet. Stellar feedback such as outflows or blast waves of supernovae might be important on a certain scale while the turbulent flow of the ISM might be important on larger scales (Mac Low & Klessen 2004).

The importance of magnetic fields is a fundamental problem of star formation and currently controversially debated (Bourke et al. 2001; Mouschovias & Tassis 2008; Crutcher et al. 2008, 2009, 2010; Mouschovias & Tassis 2010). Furthermore, the importance of magnetic fields might differ on different stages within the lifetime of a molecular cloud. While in the ISM with densities around $n \approx 1$ cm^{-3} the lack of self-shielding leads to high ionization fractions, the denser parts of the molecular cloud are only weakly ionized, so that ion-neutral collisions are sparse and the material does not couple efficiently to the magnetic fields leading to efficient ambipolar diffusion. Possibly, magnetic fields only shift the mass for the initial collapse to higher values (McKee & Ostriker 2007).

When an individual density enhancement in the molecular cloud is no longer supported against collapse by other forces, it further contracts while the central core does not exist yet. These clumps can have masses of or greater than a few hundred solar masses; their fragmentation leads to the formation of protostellar cores with initially very low masses. A typical structure to start the collapse is the so-called Bonnor-Ebert sphere (Bonnor 1956; Ebert 1955). This is the most massive, self-gravitating and isothermal sphere embedded in an ambient medium with a fixed boundary pressure that can remain in hydrostatic equilibrium (c_s is also assumed to be constant). The associated mass and size are

$$M_{BE} = \frac{1.2\, c_s^3}{G^{1.5}\rho^{0.5}}$$

and

$$l_{BE} = 0.48 \frac{c_s}{\sqrt{G\rho}}\,,$$

where ρ is the mass density, G is the gravitational constant and c_s is the local isothermal sound speed ($c_s = \sqrt{\gamma \frac{kT}{m}}$, k: Boltzmann constant, T: temperature, m: particle mass, γ: adiabatic index) and I have used $p = \rho c^2$. The corresponding Jeans values are higher but of the same order. The density profile of such a Bonnor-Ebert sphere is rather flat towards the center and falls off with increasing distance to the center r as r^{-2}. This profile often approximates observed prestellar cores (Kandori et al. 2005). Figure 1.3 shows a so-called Bok globule which is thought to be the isolated counterpart of dense clumps usually found in larger molecular clouds (e.g. Alves et al. 2001) and might repre-

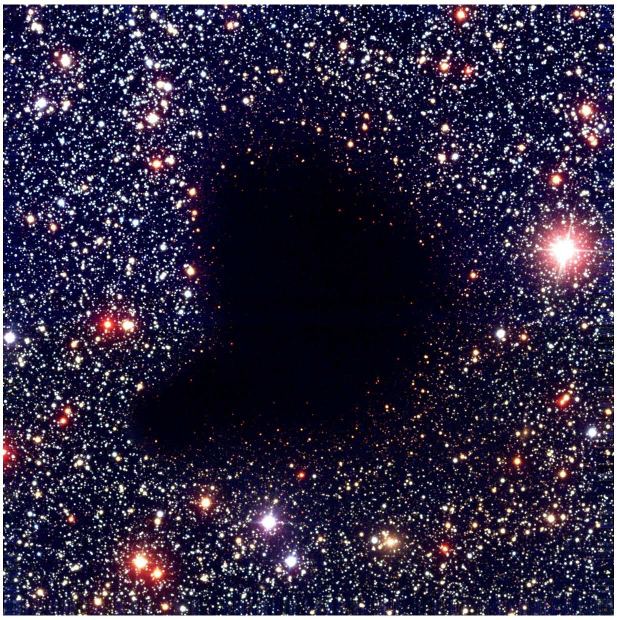

Figure 1.3: The image of Bok globule Barnard 68 nicely shows the obscuration of background light by the dust. This globule might constitute the remnant structure of a molecular cloud disrupted by stellar winds, strong UV radiation or supernova explosions and likely represents the initial stage for the formation of only very few stars. Credits: ESO

sent the simplest molecular structure in which stars can form. The hierarchical structure of the turbulence predicts that the motion becomes sub-sonic on scales comparable with the Jeans length or l_{BE} (≈ 0.1 pc). The resulting absence of shocks induced by the turbulence within this region might cause the smoothly varying density profiles of prestellar cores (Rosolowsky et al. 2008).

Rotation reduces the growth rate of unstable clumps but the sizes and masses which collapse are close to the Jeans or Bonnor-Ebert values. This is also the case when magnetic fields come into play; they also stabilize perturbations and might slow down the collapse (Heitsch et al. 2001) but the critical scales can still be approximated by the Jeans length.

The process ultimately determining the universal shape of the IMF is not clear yet. One explanation is that the protostars accrete their mass from a specific "predetermined" mass reservoir, which is mainly unaltered during their evolution. There are simulations showing that the accretion of mass in the immediate vicinity of the core leads to the observed IMF, indicating that the clump mass distribution is indeed the dominant factor determining the IMF (Chabrier & Hennebelle 2010). Another explanation is the so-called competitive accretion (Bonnell et al. 1997), where the initial objects have low masses and accrete the remaining mass from the cloud in competition with nearby cores during their subsequent evolution. This process also produces an initial mass distribution approximately similar to the observed one (Bate 2009). Furthermore, dynamical interactions might be important for the distribution of masses since this can lead to the ejection of cores from the dense clumps in which they formed (Bate et al. 2002).

In summary, all processes possibly contributing to the fragmentation of the cloud result in critical sizes for the collapsing clumps of the order of the Jeans' criterion and a characteristic distribution of their masses while only a small fraction of the total cloud is collapsing eventually. A typical structure for the initial clump could be the Bonnor-Ebert sphere and turbulence might initiate the collapse.

1.3 Core collapse

The basic properties of the protostellar collapse have already been described by Larson (1969): The gravitational energy released can initially be radiated away freely, thus the clump remains roughly isothermal and produces a strong central density peak. The central density structure approaches $\rho \propto r^{-2}$ almost independently of the initial conditions (e.g. Foster & Chevalier 1993). This is directly related to the fact that the free-fall time is proportional to $1/\sqrt{\rho}$, which dramatically enhances the density contrast in the absence of other forces. The protostellar object forms at the center being opaque and in hydrostatic equilibrium.

The details of the collapse are, not surprisingly, unclear as well and again depend on the importance of the magnetic field and the location where the collapse is initiated. There are two different scenarios for the collapse that differ mainly in the assumed initial clump configuration. In the so-called inside-out collapse, the clump is initially at rest and supported by magnetic pressure. Ambipolar diffusion reduces this support compared to gravity (Shu et al. 1987), thus eventually forming a centrally peaked structure, a so-called singular isothermal sphere (SIS) with a density structure $\rho \propto r^{-2}$, where magnetic fields in the center are virtually negligible (Shu et al. 1999). This unstable clump starts the collapse at its center and the collapse proceeds as a wave traveling outwards with the sound velocity. In the other scenario, the collapse starts at the outer radius and the initial structure can be approximated by a Bonnor-Ebert sphere in which gravity overcomes the supporting forces, e.g., initiated by larger scale turbulent motions. The collapse leads to an increasingly centrally peaked structure with a density profile $\rho \propto r^{-2}$. This density structure would be the starting point for the actual inside-out collapse, but this time the envelope is already in-falling when the core forms. In this scenario the initial in-fall velocities are supersonic and the accretion rates onto the core are higher than for the first process, but will decrease with time. Both pictures share the central peak which contains initially only a small mass and which accretes most mass from the envelope.

The two processes, also termed the slow and the fast mode of star formation by Larson (2003), might simply describe different stages during the formation process, i.e., the fast mode might approximate the inner part of the collapse when the first core forms while the slow mode applies to later times and the outer part of the collapsing clump. Gravitational collapse times approximately equal free fall times, which translates to 10^5 years once the core has formed.

The formation of the protostar, i.e., of a hydrostatic core, proceeds in two steps, one before and one after the dissociation of molecular hydrogen (Boss 1995). At densities above $\rho \gtrsim 10^{10}\,\mathrm{cm}^{-3}$ the first core becomes opaque and the central temperature increases so that the collapse slows down. The first core with a mass of about $10^{-2}\,M_\odot$ lives until its temperature rises above about $10^3\,\mathrm{K}$ and the opacity decreases because molecular hydrogen dissociates, which requires about 10^3 years. Then the second collapse starts and the density of the central part approaches a value of $1\,\mathrm{g\,cm}^{-3}$. This second core contains only about a tenth of the mass of the first one. Note that the formation of multiple systems can be initiated during any of these collapse phases, i.e., the first core can fragment into multiple cores if it rotates fast enough.

All collapse scenarios predict a stellar embryo containing intially only a small fraction of its final mass. Most of the mass has to be accreted during the subsequent phases from the in-falling envelope. Since the central part is approximately hydrostatic, the accreted matter produces an accretion shock on the surface and the luminosity of the just formed protostar is the so-called accretion luminosity

$$L_{acc} \approx \frac{G\,M_\star}{R_\star}\dot{M}_{acc}\,,$$

where $M_\star$ is the mass of the star, $R_\star$ is its radius and $\dot{M}_{acc}$ is the usually varying mass accretion rate. As the core is by definition optically thick, the accretion shock at the "surface" of the core heats the material, which in turn causes the core to expand until it reaches a radius of $\sim 4\,R_\odot$ and the radiation can be radiated away freely. This size is almost independent of the mass and preserved during most of the protostellar evolution phase. Stars with final masses below $8\,M_\odot$ start burning deuterium when they reach a mass about $0.2\,M_\odot$ during the protostellar accretion phase. More massive stars already start to burn hydrogen in this phase (Palla & Stahler 1991).

Since some amount of rotation is inherent in every realistic cloud, the developing structure departs from spherical geometry and a disk forms from which the matter is accreted onto the protostar. An important question in star formation is how the angular momentum of the accreted matter is lost as observations clearly show that protostars in later evolutionary stages, e.g. classical T Tauri stars, spin only with about 10% of their break-up speed which is less than expected from the strong contraction of the initial cloud and the conservation of angular momentum. Some theories which invoke instabilities within the disk, predict that accretion is more episodic, e.g., burst-like instead of continuous. The FU Ori like outburst sometimes observed for protostars, i.e., sudden increases in the accretion and an associated luminosity increase lasting typically for several decades, might relate to this episodic accretion process.

Protostellar outflows accompany almost all steps of star formation and have indeed been observed during the phases just described (Bachiller 1996). Their relative importance for the removal of angular momentum compared to, e.g., viscosity in the accretion disk, is still not clear. The details of these jets are presented in the next chapter and references to my work dealing with protostellar jets will be given there. Another possibility to remove angular momentum from the disk is the formation of spiral waves in the disk. They can transport angular momentum outwards in the disk, thus allowing the accretion of matter from the inner rim of the disk. In this scenario, the spiral waves are due to tidal disturbances or related to the same instabilities that might be responsible for the formation of planets in the protostellar disks.

During these phases of star formation, the protostar is still obscured by its envelope. This fact and the dominance of cool temperatures during the formation steps outlined above make infrared observations very valueable, and the different phases of star formation can be characterized by the peak of the observed emission as initially proposed by Lada (1987). The objects pertaining to the processes just described are the Class 0/I objects in this nomenclature. The very young objects with high accretion rates during the approximately first few 10^4 years are called Class 0 objects. They possess an in-falling envelope and their emission peaks at sub-mm wavelengths. Further evolved objects during their later accretion phase lasting about 10^5 years are termed Class I objects. They are most luminous in the far infrared. These objects show disk signatures and the accretion rate is much lower than during the Class 0 phase.

X-ray photons can, just as infrared light, pass through moderately massive protostellar envelopes, thus giving insight into the earliest stages of stellar magnetic activity. My work deals mostly with X-ray emission related to star formation and I focus on the X-ray properties of young stellar objects in the following. For very young protostars, however, only few reliable X-ray detections are available (e.g. Tsuboi et al. 2001; Hamaguchi et al. 2005; Getman et al. 2007, and references therein). It is still unclear whether these objects are in general intrinsic X-ray sources (Prisinzano et al. 2008) as it is observationally not easy to distinguish them from further evolved Class I objects, because their spectra differ only longwards of about $20\,\mu$m which is often not covered by observations. Furthermore, the strong absorption due to the in-falling envelope hampers detections. Due to the inability to safely distinguish the two classes observationally, they are often merged into Class 0-I. It seems likely that the hard X-ray emission ($E \gtrsim 2$ keV) of this Class 0-I is comparable to that of the more evolved Class II and III objects (Prisinzano et al. 2008). In chapter 5 a high resolution X-ray study of the Cepheus A star formation region is presented. The protostars in this region are probably in their main accretion phase described above.

1.4 Classical T Tauri stars

The protostellar core becomes a pre-main-sequence star when it has accreted approximately 90% of its final mass. A typical timeframe to accomplish this is 10^6 years. The protostellar envelope eventually disappears and the star appears on the so-called “birthline” in the Hertzsprung-Russel diagram, a locus of almost constant radius of around $4\,R_\odot$. Low-mass objects in this stadium are called classical T Tauri stars (CTTS). CTTS accrete at a rather low rate of approximately $10^{-8} \ldots 10^{-7}\,M_\odot$/yr from their circumstellar disk, which has only a marginal effect on their final stellar mass. The CTTS phase corresponds to Class II objects where most energy is radiated in the near-infrared and visible. The infrared colors of this class might resemble approximately those of Class I objects when viewed almost edge-on.

The absence of the dense envelope allows to observe regions closer to the star at shorter wavelengths ($\lambda \lesssim 1\,\mu$m) than before, thus enabling the most detailed studies of various processes of star formation such as accretion and jet launching. Examples of such studies include the inner hole of the accretion disk (Muzerolle et al. 2003), the UV and soft X-ray excess pertaining to the accretion process (Calvet & Gullbring 1998; Gomez de Castro & Lamzin 1999; Kastner et al. 2002; Güdel & Telleschi 2007) and the measurements of magnetic fields[2] (e.g. Johns-Krull 2009). X-ray emission in general is ubiquitous for CTTS and this class displays the youngest protostars suitable for X-ray grating spectroscopy showing, e.g, high electron densities possibly explainable by the accretion process (e.g. Günther et al. 2007). Although accretion and jet emission can contribute to the X-ray luminosity, the X-ray luminosity increases towards later evolutionary stages where these processes ceased (e.g. Preibisch et al. 2005). The cause of this pattern is not clear. Nevertheless, detailed X-ray studies of large samples of CTTS show that the most active stars have $L_X/L_{bol} \sim 10^{-3}$ and that there is a dependence of the X-ray luminosity on the stellar mass (e.g. the XEST survey of the Taurus molecular cloud, Güdel et al. 2007). The X-ray jet of the CTTS DG Tau is investigated in ch. 8.

1.5 Final pre-main-sequence evolution

Contracting for a few million years, the stars eventually become hot enough in their center to burn hydrogen. Until this stage, the star is considered a young stellar object. The new star has now settled on the main-sequence where low-mass stars remain for a long time ($\gtrsim 10^9$ years).

The time between the CTTS phase and the main-sequence during which the majority of the circumstellar disk disappears is often called the weak-line T Tauri star (WTTS) phase. WTTS correspond to Class III objects and do not show signs of accre-

[2]The first magnetic field detected for an object at an earlier evolutionary stage has been presented in Johns-Krull (2007).

tion or substantial amounts of circumstellar matter while some residual disk can be present. During this intermediate state, a so-called debris disk is often observed that is almost devoid of gas and consists mainly of grains. The collisions of larger bodies in these disk produce smaller grains giving raise to the name of these disks. Debris disks have typical lifetimes of about 10 Myr around solar-type stars and longer around stars of earlier spectral type, which might be related to the formation process of the grains, i.e., the location where planetesimals form. The grains are accreted onto the central object or blown out of the system depending on their individual properties like size and mass or orbital parameters. The solar system's Kuiper-belt is probably a remnant of such a debris disk. One of the nearest stars known to harbor a debris disk is AU Mic which is also a strong X-ray source. In ch. 9, a study of this object focusing on absorption features imposed onto the X-ray spectrum by the debris disk is presented.

Bibliography

Adams, F. C. & Myers, P. C. 2001, ApJ, 553, 744

Alves, J. F., Lada, C. J., & Lada, E. A. 2001, Nature, 409, 159

Bachiller, R. 1996, ARA&A, 34, 111

Bate, M. R. 2009, MNRAS, 392, 1363

Bate, M. R., Bonnell, I. A., & Bromm, V. 2002, MNRAS, 332, L65

Binney, J. & Tremaine, S. 1987, Galactic dynamics, ed. Binney, J. & Tremaine, S.

Bonnell, I. A., Bate, M. R., Clarke, C. J., & Pringle, J. E. 1997, MNRAS, 285, 201

Bonnor, W. B. 1956, MNRAS, 116, 351

Boss, A. P. 1995, ApJ, 439, 224

Bourke, T. L., Myers, P. C., Robinson, G., & Hyland, A. R. 2001, ApJ, 554, 916

Calvet, N. & Gullbring, E. 1998, ApJ, 509, 802

Chabrier, G. & Hennebelle, P. 2010, ArXiv e-prints

Crutcher, R. M., Hakobian, N., & Troland, T. H. 2008, ArXiv e-prints

Crutcher, R. M., Hakobian, N., & Troland, T. H. 2009, ApJ, 692, 844

Crutcher, R. M., Wandelt, B., Heiles, C., Falgarone, E., & Troland, T. H. 2010, ApJ, 725, 466

Ebert, R. 1955, Z $Astrophys.$, 37, 217

Evans, N. J., Dunham, M. M., Jørgensen, J. K., et al. 2009, ApJS, 181, 321

Ferrière, K. M. 2001, Rev. Mod. Phys., 73, 1031

Foster, P. N. & Chevalier, R. A. 1993, ApJ, 416, 303

Getman, K. V., Feigelson, E. D., Garmire, G., Broos, P., & Wang, J. 2007, ApJ, 654, 316

Goldsmith, P. F. 2001, ApJ, 557, 736

Gomez de Castro, A. I. & Lamzin, S. A. 1999, MNRAS, 304, L41

Güdel, M., Briggs, K. R., Arzner, K., et al. 2007, A&A, 468, 353

Güdel, M. & Telleschi, A. 2007, A&A, 474, L25

Günther, H. M., Schmitt, J. H. M. M., Robrade, J., & Liefke, C. 2007, A&A, 466, 1111

Hamaguchi, K., Corcoran, M. F., Petre, R., et al. 2005, ApJ, 623, 291

Hartmann, L. 2003, ApJ, 585, 398

Heitsch, F., Mac Low, M., & Klessen, R. S. 2001, ApJ, 547, 280

Jeans, J. H. 1902, Philosophical Transactions of the Royal Society of London. Series A, Containing Papers of a Mathematical or Physical Character, 199, pp. 1

Johns-Krull, C. M. 2007, ApJ, 664, 975

Johns-Krull, C. M. 2009, in IAU Symposium, Vol. 259, IAU Symposium, 345–356

Kandori, R., Nakajima, Y., Tamura, M., et al. 2005, AJ, 130, 2166

Kastner, J. H., Huenemoerder, D. P., Schulz, N. S., Canizares, C. R., & Weintraub, D. A. 2002, ApJ, 567, 434

Klessen, R. S., Heitsch, F., & Mac Low, M. 2000, ApJ, 535, 887

Lada, C. J. 1987, in IAU Symposium, Vol. 115, Star Forming Regions, ed. M. Peimbert & J. Jugaku, 1–17

Lada, C. J. & Lada, E. A. 2003, ARA&A, 41, 57

Larson, R. B. 1969, MNRAS, 145, 271

Larson, R. B. 1985, MNRAS, 214, 379

Larson, R. B. 2003, Reports on Progress in Physics, 66, 1651

Leroy, A. K., Walter, F., Brinks, E., et al. 2008, AJ, 136, 2782

Mac Low, M. & Klessen, R. S. 2004, Reviews of Modern Physics, 76, 125

McKee, C. F. & Ostriker, E. C. 2007, ARA&A, 45, 565

Mouschovias, T. C. & Tassis, K. 2008, ArXiv e-prints

Mouschovias, T. C. & Tassis, K. 2010, MNRAS, 409, 801

Muzerolle, J., Calvet, N., Hartmann, L., & D'Alessio, P. 2003, ApJ, 597, L149

Palla, F. & Stahler, S. W. 1991, ApJ, 375, 288

Preibisch, T., Kim, Y., Favata, F., et al. 2005, ApJS, 160, 401

Price, D. J. & Bate, M. R. 2009, MNRAS, 398, 33

Prisinzano, L., Micela, G., Flaccomio, E., et al. 2008, ApJ, 677, 401

Robitaille, T. P. & Whitney, B. A. 2010, ApJ, 710, L11

Rosolowsky, E. W., Pineda, J. E., Foster, J. B., et al. 2008, ApJS, 175, 509

Shetty, R., Collins, D. C., Kauffmann, J., et al. 2010, ApJ, 712, 1049

Shu, F. H., Adams, F. C., & Lizano, S. 1987, ARA&A, 25, 23

Shu, F. H., Allen, A., Shang, H., Ostriker, E. C., & Li, Z. 1999, in NATO ASIC Proc. 540: The Origin of Stars and Planetary Systems, ed. C. J. Lada & N. D. Kylafis, 193–+

Tsuboi, Y., Koyama, K., Hamaguchi, K., et al. 2001, ApJ, 554, 734

Williams, J. P., Blitz, L., & McKee, C. F. 2000, Protostars and Planets IV, 97

2. Protostellar jets

Protostellar outflows, driven by the forming protostar-disk system, have now been observed from the youngest Class 0 objects to the more evolved classical T Tauri stars. Figure 2.1 shows a nice example of a protostellar jet observed with the Hubble Space Telescope (HST). Such outflows might play an important role for star formation; they are connected to the angular momentum problem and contribute to the turbulence in molecular clouds. In addition, jets provide an important and universal diagnostic of the star formation process. They relate to the accretion process (energy conservation), to the magnetic fields (jet launching and jet collimation), to disk and stellar rotation (angular momentum conservation) and to the accretion disk structure (jet launching).

One part of the work presented in this thesis deals with the X-rays emission from protostellar jets while most prior research focused on the optical emission from the so-called Herbig-Haro (HH) objects. This chapter starts with a description of the morphology of protostellar jets to provide the basis for a brief overview over previous observations. It continues with a description of some of the theoretical ideas explaining how these jets are launched and a short collection of open questions.

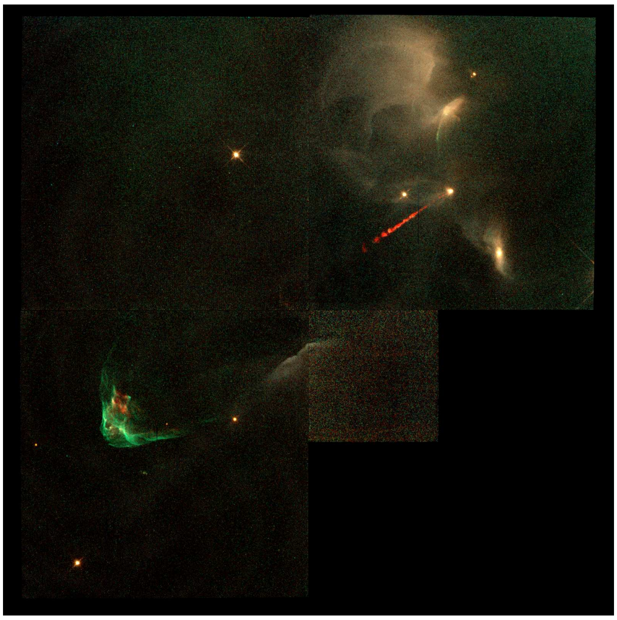

Figure 2.1: HST image of HH 34. A large bowshock is located at the bottom left with strong Hα emission (green). The [S II] emission (red) from the chain of knots traces the jet closer to the star; individual knots are ejected approximately every 15 years. Image credit: NASA.

2.1 Rendering protostellar jets visible

After some initial controversy about the nature of the non-stellar emission observed near star forming regions, e.g., whether the emission is star light reflected by dust, it is now commonly accepted that one kind of this nebular emission is produced in the post-shock cooling zones of super-sonic flows[1]. The shock heating happens either where the outflow interacts with the ambient medium (termination shock) or within the flow (internal shocks). Protostellar jets are supersonic as the escape velocity from the gravitational potential of the forming protostar, approximately 100 km s^{-1} for a 1 $M_\odot$ star depending on the actual launching point of the jet, exceeds the sound velocity of the ambient medium of roughly a few km s^{-1}. For a deeper understanding of these outflows, one first has to understand the heating and the cooling of these objects.

[1]Another example of nebular emission is an H II region ionized by the radiation of hot young stars.

2.1.1 Magnetohydrodynamics (MHD)

In order to derive the properties of a shock front, the dynamics of the plasma can often be described in the framework of hydrodynamics (HD) or, in the pres-

MHD equations (cgs-units)

Continuity equation	$\frac{\partial\rho}{\partial t} + \nabla\cdot(\rho\mathbf{v}) = 0$
Equation of motion (Euler equation)	$\rho\frac{d\mathbf{v}}{dt} + \rho\left(\mathbf{v}\nabla\right)\mathbf{v} = -\nabla\mathbf{p} + \mathbf{f}$
or Navier-Stokes equation (dissipative terms)	$\rho\frac{d\mathbf{v}}{dt} + \rho\left(\mathbf{v}\nabla\right)\mathbf{v} = -\nabla\mathbf{p} + \mathbf{f} + \mathbf{v}\rho\triangle\mathbf{v} + \frac{\mathbf{j}}{\mathbf{c}}\times\mathbf{B}$
Faraday equation (no resistivity)	$\frac{\partial\mathbf{B}}{\partial t} = \nabla\times(\mathbf{v}\times\mathbf{B})$
or magnetic differential equation (with resistivity)	$\frac{\partial\mathbf{B}}{\partial t} = \nabla\times(\mathbf{v}\times\mathbf{B}) + \eta\nabla^2\mathbf{B}$
Initially (this property is then preserved)	$\nabla\mathbf{B} = 0$
Pressure equation	$p = p(\rho, T)$

Table 2.1: $\rho = nm$: mass density, n: number density, m: mean molecular mass, $\mathbf{v}$: bulk velocity, p: pressure, $\mathbf{B}$: magnetic field, $\mathbf{j}$: electric current, $\mathbf{f}$: external force density including gravitation.

ence of magnetic fields, in the context of MHD. In general, HD considers the behavior of a fluid, i.e., a material without rigidity. In the astrophysical context, this fluid is usually a gas or a plasma. The essential assumption for the fluid description is that collisions between the constitutes of the fluid are sufficiently frequent, which means that the mean free path length is much smaller than the macroscopic length scale of interest so that the fluid can be described as a continuum. The MHD equations given in Table 2.1 can be found in various text books (e.g. Kulsrud 2005). The current $\mathbf{j} = \frac{c}{4\pi}\nabla\times\mathbf{B}$ and the electric field $\mathbf{E} = -\mathbf{v}/c\times\mathbf{B}$ are derived quantities in this description. These equations have to be complemented by an equation for the energy conservation.

2.1.2 Shocks

When the gradient of a hydrodynamic property such as the density increases beyond a specific point, the assumption of fluid-like behavior breaks down. This is exactly the case in a shock. However, the fluid description remains valid on both sides of the shock, and basic physical conservation laws, like mass and momentum conservation, relate the fluid properties on both sides of the shock. The region where the fluid description is not valid is usually small compared to the total volume of interest. It is therefore reasonable to assume that virtually no mass is directly contained in the shock and that all mass moving into the shock leaves the shock at the opposite side.

Additionally to the conservation laws, the values of the preshock gas and the shock velocity are needed to fully determine the postshock properties. The following relations from Hartigan (2003) apply only to the component normal to the shock front while the other velocity components remain unchanged. Assuming a constant polytropic index γ in the entire region, the compression factor of the shock in the absence of magnetic fields is given by

$$\begin{aligned} C = \frac{n_2}{n_1} = \frac{v_1}{v_2} &= \frac{\gamma+1}{\gamma-1+2M^{-2}} \\ &= 4\,, \end{aligned} \tag{2.1}$$

where the subscripts 1 and 2 denote the pre- and postshock properties, M is the Mach number of the flow ($M = v/c_s$) and the other variables have been described in Table 2.1. The second line describes the limit of high Mach numbers ($M \gg 1$) and an ideal gas ($\gamma = 5/3$), i.e., a so-called strong shock. For high Mach numbers, the temperature of the postshock gas can be approximated by

$$T_2 = \frac{2(\gamma-1)mv_1^2}{(\gamma+1)^2\,k_B} \tag{2.2}$$

$$= \frac{3mv_1^2}{16\,k_B} \approx 1.4 \times 10^5\, v_{100}^2\, \mathrm{K}\,,$$

where v_{100} is the initial velocity in $100\,\mathrm{km\,s^{-1}}$ and the second line again pertains to an ideal gas. Including magnetic fields complicates the structure of the equations, but in the simple case of negligible magnetic field perpendicular to the shock plane, one can define the fast magnetosonic speed by $v_F = \sqrt{c_s^2 + v_A^2}$, where v_A is the Alfvén velocity, i.e., the velocity of the magneto-sonic wave with equal amounts of kinetic and magnetic energy. Substituting M by v/v_F, eq. 2.1 remains approximately valid.

As a shock is supersonic, the postshock gas cannot communicate with the preshock material directly. Nevertheless, there are certain types of precursor by which the postshock gas can still interact with the preshock matter. The radiation from the postshock plasma can pre-ionize the preshock gas in a so-called radiative precursor. The energy, which would have been consumed by ionizing the preshock gas, now goes into heating. This increases the temperature of the postshock gas and the resulting postshock temperature appears hotter than expected for the actual shock velocity without radiative feedback. Another way of the postshock gas to interact with the preshock gas is by magnetic fields. This allows for so-called C-type (continuous) shocks where no jump in the hydrodynamic variables exists. The resulting emission region appears like that of a non-magnetic shock with a lower shock velocity.

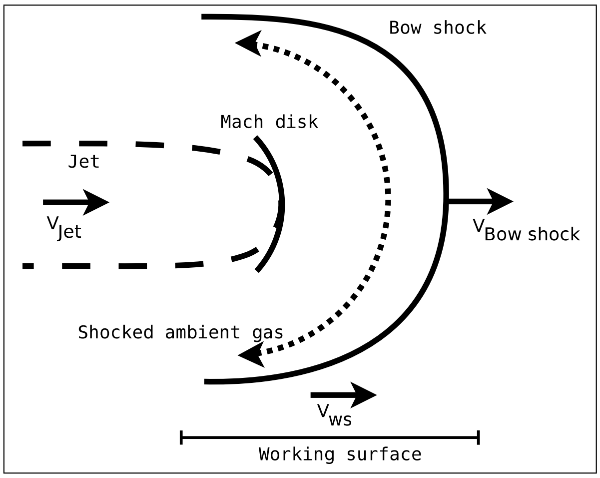

Figure 2.2: Cartoon of the working surface of a protostellar jet. The shock velocity of the Mach disk is $v_{Mach} = v_{jet} - v_{ws}$ (v_{ws} is the velocity of the working surface) and the shock velocity of the bowshock is $v_{bs} = v_{ws} - v_p$, where v_p is the velocity of the material ahead of the working surface with respect to the jet source.

2.1.3 Shocks in protostellar jets

When a steady supersonic flow encounters another fluid, as at the front of an astrophysical supersonic jet, usually two shocks form (see Fig. 2.2). In the so-called bow shock, the material in front of the jet is accelerated in the observatory frame. This shock is usually located where the outflow interacts with the ambient medium, or in less violent shocks, within the outflow where gas parcels with different velocities interact. The second shock is generated by the bow shock and moves back into the jet. In this so-called Mach-disk or jet-shock, the outflowing gas is decelerated and the region bounded by these two shocks is referred to as the working surface (Blandford & Rees 1974). The density contrast between the jet and the ambient medium determines if the bow shock or the Mach disk exhibit higher shock velocities. If the jet is denser than the ambient medium the shock velocity of the bow shock will be higher. Hartigan (1989) discussed how the surface brightness of both shocks depends on the jet velocity and the density ratio for radiative shocks; the bow shock is again brighter for denser jets. When the flow is not continuous, but episodic so that the bow shock can move faster than the replenishing flow, no Mach-disk will form.

2.1.4 Radiative shocks

A shock is called "radiative" when radiative cooling dominates over adiabatic cooling. Figure 2.3 shows the basic properties of such a radiative, collisional shock. It consists of a radiative precursor which may heat and potentially ionize the preshock gas, a shallow shock front region where the material is compressed, heated and potentially ionized by collisions, and a more extended cooling zone behind this shock front[2] where most of the observed emission comes from. A "typical" HH object radiates mostly in recombination lines and forbidden emission lines (FELs) such as [S II]. These lines are excited by the

[2]Ion and electron temperatures differ directly behind the shock and equilibrate later.

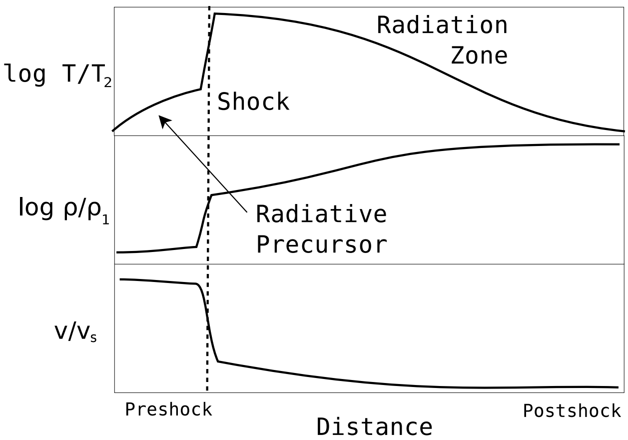

Figure 2.3: Sketch of the evolution of the hydrodynamic properties for a radiative shock. T_2 is the post-shock temperature immediately behind the shock, ρ_1 is the preshock density, v_s is the shock velocity, and v is measured relative to the shock front.

hot electrons of the postshock plasma. The length of the cooling zone can be approximated according to Reipurth & Bally (2001) by

$$d \approx 30 \left(\frac{100\,\mathrm{cm}^{-3}}{n}\right)\left(\frac{v}{100\,\mathrm{km\,s}^{-1}}\right)^4 \mathrm{AU}\,. \quad (2.3)$$

The details of the emission depend on (a) the shock velocity, (b) the magnetic field, and (c) the ionization of the preshock material. The latter point is related to the shock velocity as the radiative precursor can ionize the preshock material for shock velocities exceeding approximately $v_{shock} \gtrsim 110\,\mathrm{km\,s}^{-1}$ (Cox & Raymond 1985). Balmer-line emission is also emitted immediately behind the shock front as any neutral H atom entering the hot postshock gas has a relatively large chance to become collisionally excited before being ionized over a large range of shock conditions (Chevalier et al. 1980). Therefore, the Hα emission denotes the actual shock location. HH objects are usually optically thin with the possible exception of the UV range (Hartigan et al. 1999).

The highest shock velocities, and thus the highest excitation conditions, are found at the apex of the bow shock and subsequent lower shock velocities are found at larger distances from the jet axis as the shock becomes increasingly oblique for increasing distances from the jet axis. In the cooling zone, higher ionization species dominate the emission close to the shock front while lower excitation species are found at greater distances. E.g., [O III] would be located closer to the shock front than the [O I] emission. Hartigan et al. (1987) modeled the bow shock emission by sampling its shock-velocity structure with a series of 1D plane-parallel shock models and tabulated the line emission for a large range of jet parameters. These data have been successfully applied to a number of HH objects. However, discrepancies emerge when the shock velocity increases, in particular with line ratios involving the [S II] and Hα emission of high excitation HH objects (Raga et al. 1996).

2.1.5 Protostellar flows

Observations of protostellar jets usually show emission from many different shocks. Their evolution and interpretation depends on the flow properties and on the ambient medium through which they travel.

Although protostellar jets are magnetically collimated, they are essentially ballistic supersonic flows beyond some distance to the driving source. In general, the density of the ambient medium does not suffice to provide the required pressure for further collimation. Therefore, the flow becomes ballistic when the inertia of the plasma exceeds the decreasing magnetic forces beyond a certain distance from the driving source. At typical distances of roughly 100 AU, i.e. about an arcsec for the nearest observed protostellar jets, the ballistic approximation probably holds[3]. For these "non-magnetic" flows the opening angle 2α relates to the sonic Mach number M by

$$\sin\alpha = \frac{c_s}{v} = \frac{1}{M}\,, \quad (2.4)$$

as disturbances perpendicular to the flow cannot proceed faster than the local sound velocity. When the initial collimation due to helical magnetic fields is sufficiently strong, the high Mach numbers of protostellar jets naturally lead to the small observed opening angles even at large distances from the driving source.

2.2 Observations of protostellar jets

The pioneering works of Herbig (1950, 1951) and Haro (1952, 1953) identified that the nebulous emis-

[3] Collimation is observed at these scales, thus the magnetic field strength beyond this distance should be smaller than the inertia of the outflowing matter, see sect. 2.3.

sion lines, such as Hα, [O I] or [S II], are related to star formation. The continuous numbering of protostellar outflows as HH 1,2, ... etc. is reminiscent of these first works. Typical sizes of protostellar jets are a few tenth of a parsec in length and roughly 10^3 AU in size for their emission regions, e.g., individual knots.

As outlined in the previous chapter, the protostars accrete with the highest rates during their earliest evolutionary stages and the accretion declines with increasing age. The relation between outflows and accretion predicts that the mass-loss rate also decreases with increasing age of the protostar as the mass-loss rate is typically 10% of the accretion rate (Cabrit et al. 1990; Hartigan et al. 1995). This tight correlation observationally shows that the outflows are powered by accretion or are at least intimately connected with the accretion process. The fraction of jet driving sources decreases with stellar age; while probably all Class 0 objects drive protostellar outflows, this fraction significantly reduces towards CTTS. However, the substantial circumstellar envelope of the youngest protostars renders optical observations of their outflows close to the launching region virtually impossible. Therefore, the detailed studies of CTTS jets within the innermost few 10 AU of the launching zone currently provide the best observational constraints for jet launching models. Nevertheless, observations of jets from deeply embedded driving sources (Class I) in the IR indicate that their jets share many similarities with their older counterparts, indicating a similar launching mechanism (Ray et al. 2007; Garcia Lopez et al. 2010).

As this thesis partly deals with the X-ray emission of protostellar jets, selected properties of protostellar jets which can be measured by X-ray observations are compared to observations at other wavelengths in the following section. The molecular outflows often accompanying protostellar jets will not be discussed here as they represent the slowest part of the outflow and are thus unlikely (directly) related to the X-ray emission.

2.2.1 Imaging

As jets are dynamic objects, proper motion measurements provide insights into the heating process. A continually heated stationary emission region would indicate an overpressured outflow expanding out of a nozzle in contrast to a moving knot, which is not easily explained in such a scenario (Rubini et al. 2007). Eislöffel & Mundt (1998) measured the proper motion of protostellar jets in the Taurus star forming region and showed that space velocities of individual knots are typically 100-200 km s^{-1}. However, the measurement of the proper motion of individual knots is complicated by cooling and shock heating of individual parts of the knots. Therefore, these measurements require a very high spatial resolution in general as the cooling time of individual knots is comparable to the time on which ground-based observations are sensitive to position changes (roughly a few years). High-resolution observations of individual HH objects with the HST showed that typical velocities are indeed 100-200 km s^{-1} while the velocity dispersion between individual knots is rather low, e.g., the velocity dispersion between the knots in Fig. 2.1 is only about 25 km s^{-1}. In addition, the flow velocity decreases with increasing distance to the jet/flow axis, and the highest velocities have been measured for the knots which just peaked out of the dense shell surrounding the protostar (e.g. the jet associated with HH 34, Reipurth et al. 2002).

In a few cases, proper motion of X-ray emitting knots has been claimed, e.g., HH 154 (Favata et al. 2006) and Z CMA (Stelzer et al. 2009). However, the initial position of the knot is not clear for either of these two observations. Therefore, it is strictly speaking not known whether the observations show a moving knot or the in situ heating of plasma, i.e., exactly the problem that optical observations faced before the HST era. The results from the recent $Chandra$ DG Tau large program show that the outer X-ray emission region of DG Tau's jet indeed has a proper motion comparable to the motion of the optical knot, in contrast to the inner X-ray jet component (Güdel et al. 2010). In ch. 7 a third epoch X-ray observation of HH 154 is presented where no further motion of the claimed X-ray knot is found.

The inner parts of jets are often detected as radio sources as the emission at cm-wavelengths is not suspect to strong absorption. Additionally, these observations profit from the high angular resolution available at cm-wavelengths. These observation are able to trace the inner few 10 AU of the jets even for distant embedded sources. However, the nature of this radio emission, probably free-free (thermal) emission, is not entirely clear yet. Furthermore, the spectral index α which traces the spectral shape of the measured flux as $S_\nu \sim \nu^\alpha$ is subject to optical depth effects for protostellar jets (González & Cantó 2002). Moreover, the ionization effects the shape of the observed spectrum. Given these uncertainties, cm-radio observations provide high resolution images of the close vicinity of embedded sources and sometimes clearly show jet-like structures aligned with the outer larger scale jet. Even proper motion of individual emission structures has been detected (e.g. Rodríguez et al. 2005). Such radio observations proved to be of special importance for the articles on HH 154 (ch. 7) and Cep A (ch. 5).

There are also observations which resolve the cooling zone of the shock, e.g., HH 47 (Heathcote et al. 1996) or HH 34 (Reipurth et al. 2002). They show that the Hα emission which indicates the actual shock front and the [S II] emission from the cooling zone are spatially separated as expected from radiatively cooling shocks. Whether similar characteristics, i.e. the highest plasma temperatures at the apex and increasingly lower temperatures at increasing distances to the shock front, also apply to the X-ray portion of the jet is not clear yet. All observations to date were hampered by low count numbers. In ch. 7, a trend in the mean X-ray photon energy is found for HH 154, indicating that the cooling length of the X-ray emitting plasma might be longer than for the optical part. Chapter 6 shows an X-ray study of the cooling zone of HH 168 where no such clear trend was found. However, the emission region of HH 168 is much larger, and the densities are much lower than those of HH 154, thus it is not clear when and where the X-ray emitting plasma of HH 168 was initially heated.

2.2.2 Spectroscopy

Spectroscopic observations of protostellar jets often show line-shifts of 100-200 $\mathrm{km\,s^{-1}}$ for the emission coming from individual knots. These values are consistent with the proper motion measurements. On the other hand, the typical line-width which indicates the shock velocity is often only a few $10\,\mathrm{km\,s^{-1}}$, but again consistent with the low velocity dispersion derived from the proper motion of individual knots. There are a few cases where entrainment of ambient gas has been postulated, which might explain why the flows tend to decelerate with increasing distance to the driving sources. Due to the low surface brightness of protostellar jets, it is virtually impossible to measure line-shifts for the X-ray emission.

Near-infrared (IR) observations are able to trace the jets from deeply embedded sources closer to the actual launching region. Two typical regimes in which protostellar jets are observed in the near-IR are the high excitation lines of Fe such as [Fe II] and the molecular hydrogen emission, e.g. the 1-0 S(1) line at 2.122 μm. While the first lines trace material with $T \approx 10^4$ K, molecular hydrogen requires temperatures below approximately 3000 K to survive. If shock-heating is the excitation source for the H_2 emission, the shocks will be non-dissociative. This requires either low shock-speeds ($v_{shock} \lesssim 50\,\mathrm{km\,s^{-1}}$) or a magnetized but low-ionized medium in which a magnetic precursor can slowly heat the material by ambipolar heating ahead of the shock (C-shocks). Thus, H_2 emission is preferably found in the wings of the bow shock and should not be related to X-ray emitting plasma.

The near-IR lines of [Fe II] allow for higher plasma temperatures than H_2 and are therefore more valuable for investigating the environment of the X-ray emission. [Fe II] has density sensitive lines which can be used to measure electron densities and lines from the same upper level that can be used to determine the reddening (e.g. 1.257 μm and 1.644 μm). Itoh et al. (2000) applied this method to HH 154 and these values are of special importance for the X-ray analysis of HH 154 presented in ch. 7, where the evolution of the absorbing column density can be compared to the evolution of the X-ray photon energy. In the outer parts of the jets where the absorption is lower, also line ratios of [SII] ($\lambda\lambda$4068/4076 to $\lambda\lambda$10318/10337) can be used to determine the absorption (Miller 1968; Solf et al. 1988, who applied this method to HH 1). Knowing the absorption, line fluxes can be compared to shock models, and one can deduce the heating process (e.g. shock heating of the DG Tau jet, Lavalley-Fouquet et al. 2000).

Spatially resolved [Fe II] spectroscopy allows to map the kinematic structure of the jet close to the driving source (Pyo et al. 2002, 2003, 2005, 2009). With such observations one can measure the linewidth as a function of distance to the driving source. [Fe II] observations of HH 154 show a decreasing linewidth with increasing distance to the launching region. This indicates that collimation probably occurs within the innermost 100 AU. This spatial scale for the collimation region is comparable to measurements of jet widths as a function of distance (Garcia et al. 2001a).

The abundances within HH objects are approximately solar (Böhm & Matt 2001). The abundance of refractory elements, i.e., elements with high melting points, and in particular the abundance of Fe does not depend on the shock velocity, although one would expect that grains survive only low velocity shocks and would be destroyed by the UV radiation of stronger shocks. This can be interpreted as arising from a strong shock which all material in the HH flow experiences, or might relate to the launching region of the material. One can speculate that the stationary X-ray emission regions of HH 154 and DG Tau's jet (see ch. 7 and 8) are related to this "ubiquitous" strong shock. However note, that the abundance of refractory elements might increase with increasing distance to the driving source (e.g., Nisini et al. 2005).

For high velocity shocks, the peak emission falls into the UV regime. Strong UV lines trace the temperature range closest to that associated with the X-ray emission and can provide a detailed view on the heating process as lineshifts and widths are readily measurable in the (F)UV but not from avialable X-ray observations. The first detailed observations of the UV emission of HH objects have been obtained with the International Ultraviolet Explorer (IUE)[4]. High excitation lines such as C IV have been observed, but never indicated shock velocities in excess of 100 km s^{-1}. Neither the [N V] 1240 Å line nor O VI emission have been observed for the X-ray emitting HH 2, which points towards a rather low amount of plasma with $T \approx 3 \times 10^5$ K. The use of UV observations to study the inner parts of the jets is generally hampered by strong absorption even for moderate absorbing column densities (see Fig. 2.4). The strong absorption also applies to soft X-rays (E_{Photon} ≈0.5 keV), but is less pronounced than in the UV. Güdel et al. (2007) analyzed the spectral X-

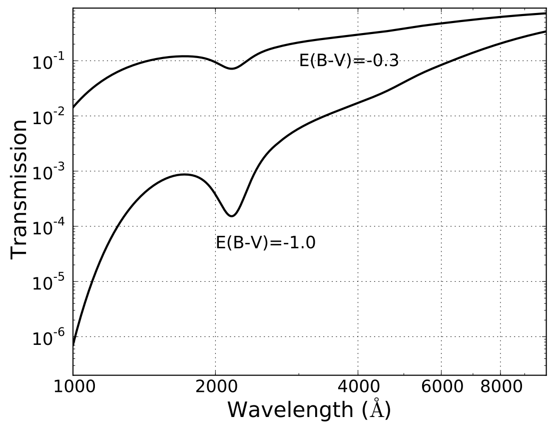

Figure 2.4: Extinction curves for E(B-V)=0.3 and E(B-V)=1.0 using the galactic extinction curve (Fitzpatrick 1999).

ray properties of jet driving sources and proposed that the soft X-ray emission from so-called Two Absorber X-ray (TAX) sources is generated within the jet while the abscence of soft X-ray emission from strongly obscured jet driving sources can be easily explained by the absorption.

One conclusion from the observations is that most HH objects have large space velocities, but, on the other hand, often resemble low excitation conditions as expected from shocks with velocities much lower than the flow velocity. There are two possible explanations for this morphology. One is a periodic, or at least pulsed, outflow creating internal shocks with velocities of approximately the amplitude of the velocity differences, thus the flow moves into a medium already set in motion by previous ejection periods. Another explanation are instabilities in the outflow, such as hydrodynamic Kelvin-Helmholtz instabilities which can cause oblique traveling shocks leading to smaller shock velocities than the flow speed (Raga & Cantó 2003). However, the detection of X-ray emission from protostellar jets (e.g. Pravdo et al. 2001; Favata et al. 2002) casts doubts about the absence of high velocity shocks since plasma temperatures above 10^6 K are required to emit the detected X-ray photons. In turn, this requires shock velocities in excess of 300 km s^{-1}. The origin of the X-ray emission is still not well understood. In a simple approach, Raga et al. (2002) explained the basic properties of strong shocks with

[4]In contrast to modern space based mission, IUE was controlled by astronomers visiting the control station in Villafranca del Castillo, Spain.

respect to X-ray emission. More detailed hydrodynamic simulations, including variations in the outflow velocity, have been performed by Bonito et al. (2004, 2010a,b). These simulations show that very high outflow velocities above 1000 $\mathrm{km\,s^{-1}}$ are required to produce the observed X-ray luminosity. However, most of the knots produced in these simulations will exhibit low space velocities compatible with observations.

Evidence for jet rotation has now been found for a few jets (Bacciotti et al. 2002; Coffey et al. 2004; Woitas et al. 2005; Coffey et al. 2007). However, it should be noted that the approaching and the receding lobes of the jet of ThA 15-28 appear to rotate in opposite directions. It is currently not clear yet, whether this indicates that the claimed rotation signatures more realistically represent upper limits of the "true" jet rotation or that the opposite rotation sense of the two lobes is real. Nevertheless, the observed rotation signatures would support current jet launching theories.

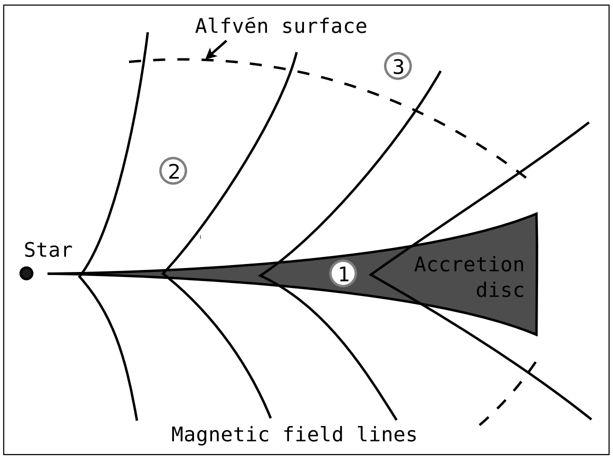

Figure 2.5: Sketch of the accretion disc with attached magnetic field lines. The energy density in the magnetic field has to be lower than the rotational energy in region 1 while it dominates the other forces in region 2. Beyond the Alfvén surface, the intertial forces of the matter dominate the magentic forces (region 3).

2.3 Launching protostellar jets

The small opening angle of protostellar jets close to their driving sources differs considerably from a largely uncollimated, pressure driven[5] stellar or coronal wind. In order to achieve the required collimation of outflows, magnetic fields are currently the most promising candidate and most work has focused on the launching of a wind from the protostellar accretion disk. However, some contribution from a stellar wind is currently not ruled out (e.g. RY Tau, Gómez de Castro & Verdugo 2007).

The basic idea of such a wind is that a "suitable" magnetic field is anchored to the Keplerian accretion disk[6], and the disk material, once loaded onto a magnetic field line, freely moves along the field line (like a "bead on a wire"). The rigid rotation of the magnetic field close to the disk surface and its inclination with respect to the disk surface force the material to flow outwards along the field lines. This happens once the disk material has been lifted off its Keplerian orbit as then the centrifugal force exceeds gravitation (Fig. 2.5). The Alfvén surface marks the position where the velocity of the plasma equals the Alfvén velocity. Up to this Alfvén surface the magnetic forces dominate the dynamics of the outflowing material and acceleration happens in this region. Beyond this surface, the inertia of the material exceeds the magnetic forces and causes the magnetic field to become increasingly helical with increasing height above the disk. This leads to the inward force collimating the outflow ("z-pinch": $F_{\mathrm{Lorentz}} \simeq \mathbf{j_z B_\phi}$). Such a wind can extract angular momentum from the accretion disc (Blandford & Payne 1982) and thereby regulate the accretion rate.

While this coarse picture is well established (more details can be found, e.g., in Spruit 1996; Pudritz & Ouyed 1999), many open issues remain. They partly relate to the term "suitable", i.e., to the origin of the magnetic field and its actual shape. Furthermore, the mass loading onto the field lines and the acceleration of the material including thermodynamic effects are currently not fully understood.

The term "suitable" is well defined for so-called cold disk winds, where the enthalpy for *accelerating* the wind is negligible. In this theory, it means that the strength of the magnetic field has to be lower than the rotational kinetic energy in the disk and that

[5]Pressure driven means that the wind is launched due to the hydrostatic stratification of the outer layers of the object and the "underdense" environment.

[6]Actually, there are feedback effects of the jet to the disk.

the inclination of the field lines with the disk has to be less than 60°. Whether the magnetic field is created by a turbulent dynamo within the disk or it is dragged inward from the ambient medium during the protostellar collapse is not clear. In any case, large scale fields have to be present, and some field lines have to open to infinity instead of connecting back to the disk. Outside the disk, the magnetic energy exceeds all other forces, i.e. the magnetic field is force-free. The field strength decreases with increasing distance to the disk and the gas loaded onto the field lines is accelerated until it reaches the Alfvén surface. Outside the Alfvén surface, the magnetic field is not force-free due to the inertia of the gas and begins to become wound-up, i.e., increasingly helical. Depending on the field configuration at large distances from the driving source, which again depends on the mass loading, the asymptotic collimation is either cylindrical or parabolic.

Mass loading of the open magnetic field lines transfers the radial plasma motion of the accretion process into the vertical one of the jets. However, the details of the mass loading which is actually a crucial parameter of the theory are not clear yet, but surely involve some vertical structure of the accretion disk.

The picture sketched above captures the essential part of the disk wind theory. However, more advanced models have been developed. They can be subdivided depending on the exact location in the disk where the wind is launched. Prominent examples are the X-wind (Shu et al. 1994) and cold/warm disk wind models. Cold vs. warm relates to the importance of the enthalpy for *accelerating* the wind; cold disk winds predict excessive terminal speeds and low outflow densities which are not consistent with observations (Garcia et al. 2001a,b). Warm disk winds currently appear to be capable of producing a jet compatible with the measurements, in particular with the observed speeds, the mass-loss rates and the rotation signatures (Ferreira et al. 2006). In these models, part of the heat produced within the disk, e.g., by turbulence, can be absorbed by the jet, and mass is lifted from the disk by the plasma pressure gradient. Whether the observation of X-ray emission from the inner parts of the jets is more related to the acceleration of the jets, to the collimation, or to something different is not clear yet. A stellar or coronal wind, or a wind ejected in the interaction zone between the stellar magnetic field and the disk magnetic field (X-wind) could also be responsible for the observed X-ray morphology.

2.4 Open questions

Protostellar jets are tightly related to the accretion process and to the configuration of the magnetic field. Therefore, the most fundamental questions relate to the launching process itself. Where is the jet launched? How is the outflow accelerated, how is it collimated? Are different launching mechanisms in operation? Answering these questions will greatly impact our knowledge of the star formation process.

Can we make use of the observed X-ray emission from protostellar jets to tackle these questions? The answer strongly depends on the nature of the observed X-ray emission. How are the high plasma temperatures achieved within protostellar jets? Strong shocks provide an attractive explanation, but indications for shock velocities sufficient for plasma heating to X-ray emitting temperatures have not been observed at other wavelengths. In any case, the X-ray emission traces an outflow component which has escaped detection in other wavelength ranges so far. It is clear that understanding the origin of this high velocity component will constrain the launching mechanism as it imposes a lower velocity limit to which the outflow engine should be able to accelerate the flow. Furthermore, the apparently stationary X-ray component within DG Tau's jet and HH 154 might pertain to some kind of base shock for which also indications at other wavelength exist. The shock location bears the potential to reveal the structure of the outflow close to the driving source as such a strong shock is not expected for a continuous or slowly varying outflows and approximately parabolic magnetic field configurations.

Bibliography

Bacciotti, F., Ray, T. P., Mundt, R., Eislöffel, J., & Solf, J. 2002, ApJ, 576, 222

Blandford, R. D. & Payne, D. G. 1982, MNRAS, 199, 883

Blandford, R. D. & Rees, M. J. 1974, MNRAS, 169, 395

Böhm, K. & Matt, S. 2001, PASP, 113, 158

Bonito, R., Orlando, S., Miceli, M., et al. 2010a, A&A, 517, A68+

Bonito, R., Orlando, S., Peres, G., et al. 2010b, A&A, 511, A42+

Bonito, R., Orlando, S., Peres, G., Favata, F., & Rosner, R. 2004, A&A, 424, L1

Cabrit, S., Edwards, S., Strom, S. E., & Strom, K. M. 1990, ApJ, 354, 687

Chevalier, R. A., Kirshner, R. P., & Raymond, J. C. 1980, ApJ, 235, 186

Coffey, D., Bacciotti, F., Ray, T. P., Eislöffel, J., & Woitas, J. 2007, ApJ, 663, 350

Coffey, D., Bacciotti, F., Woitas, J., Ray, T. P., & Eislöffel, J. 2004, ApJ, 604, 758

Cox, D. P. & Raymond, J. C. 1985, ApJ, 298, 651

Eislöffel, J. & Mundt, R. 1998, AJ, 115, 1554

Favata, F., Bonito, R., Micela, G., et al. 2006, A&A, 450, L17

Favata, F., Fridlund, C. V. M., Micela, G., Sciortino, S., & Kaas, A. A. 2002, A&A, 386, 204

Ferreira, J., Dougados, C., & Cabrit, S. 2006, A&A, 453, 785

Fitzpatrick, E. L. 1999, PASP, 111, 63

Garcia, P. J. V., Cabrit, S., Ferreira, J., & Binette, L. 2001a, A&A, 377, 609

Garcia, P. J. V., Ferreira, J., Cabrit, S., & Binette, L. 2001b, A&A, 377, 589

Garcia Lopez, R., Nisini, B., Eislöffel, J., et al. 2010, A&A, 511, A5+

Gómez de Castro, A. I. & Verdugo, E. 2007, ApJ, 654, L91

González, R. F. & Cantó, J. 2002, ApJ, 580, 459

Güdel, M., Audard, M., Bacciotti, F., et al. 2010, in Cool Stars 16

Güdel, M., Telleschi, A., Audard, M., et al. 2007, A&A, 468, 515

Haro, G. 1952, ApJ, 115, 572

Haro, G. 1953, ApJ, 117, 73

Hartigan, P. 1989, ApJ, 339, 987

Hartigan, P. 2003, Ap&SS, 287, 111

Hartigan, P., Edwards, S., & Ghandour, L. 1995, ApJ, 452, 736

Hartigan, P., Morse, J. A., Tumlinson, J., Raymond, J., & Heathcote, S. 1999, ApJ, 512, 901

Hartigan, P., Raymond, J., & Hartmann, L. 1987, ApJ, 316, 323

Heathcote, S., Morse, J. A., Hartigan, P., et al. 1996, AJ, 112, 1141

Herbig, G. H. 1950, ApJ, 111, 11

Herbig, G. H. 1951, ApJ, 113, 697

Itoh, Y., Kaifu, N., Hayashi, M., et al. 2000, PASJ, 52, 81

Kulsrud, R. M. 2005, Plasma physics for astrophysics, ed. Kulsrud, R. M.

Lavalley-Fouquet, C., Cabrit, S., & Dougados, C. 2000, A&A, 356, L41

Miller, J. S. 1968, ApJ, 154, L57+

Nisini, B., Bacciotti, F., Giannini, T., et al. 2005, A&A, 441, 159

Pravdo, S. H., Feigelson, E. D., Garmire, G., et al. 2001, Nature, 413, 708

Pudritz, R. E. & Ouyed, R. 1999, in Astronomical Society of the Pacific Conference Series, Vol. 160, Astrophysical Discs - an EC Summer School, ed. J. A. Sellwood & J. Goodman, 142–+

Pyo, T., Hayashi, M., Kobayashi, N., et al. 2002, ApJ, 570, 724

Pyo, T., Hayashi, M., Kobayashi, N., Terada, H., & Tokunaga, A. T. 2009, ApJ, 694, 654

Pyo, T., Hayashi, M., Kobayashi, N., et al. 2005, ApJ, 618, 817

Pyo, T., Kobayashi, N., Hayashi, M., et al. 2003, ApJ, 590, 340

Raga, A. C., Böhm, K., & Cantó, J. 1996, RMxAA, 32, 161

Raga, A. C. & Cantó, J. 2003, A&A, 412, 745

Raga, A. C., Noriega-Crespo, A., & Velázquez, P. F. 2002, ApJ, 576, L149

Ray, T., Dougados, C., Bacciotti, F., Eislöffel, J., & Chrysostomou, A. 2007, Protostars and Planets V, 231

Reipurth, B. & Bally, J. 2001, ARA&A, 39, 403

Reipurth, B., Heathcote, S., Morse, J., Hartigan, P., & Bally, J. 2002, AJ, 123, 362

Rodríguez, L. F., Torrelles, J. M., Raga, A. C., et al. 2005, RMxAA, 41, 435

Rubini, F., Lorusso, S., Del Zanna, L., & Bacciotti, F. 2007, A&A, 472, 855

Shu, F., Najita, J., Ostriker, E., et al. 1994, ApJ, 429, 781

Solf, J., Bohm, K. H., & Raga, A. 1988, ApJ, 334, 229

Spruit, H. C. 1996, ArXiv Astrophysics e-prints

Stelzer, B., Hubrig, S., Orlando, S., et al. 2009, A&A, 499, 529

Woitas, J., Bacciotti, F., Ray, T. P., et al. 2005, A&A, 432, 149

3. *Chandra* in context

The observations analyzed during the course of this work are almost exclusively X-ray observations, where the term X-rays means photons with energies between roughly 0.1 and 10 keV. I will therefore give a brief overview on the properties of current X-ray satellites focusing on the *Chandra* Observatory[1] operated for NASA by SAO[2] as my work is based mainly on the data from this satellite.

X-rays do not penetrate the earth's atmosphere and space based observations are therefore required to detect astronomical X-ray sources. Furthermore, the mirrors used for longer wavelength photons, i.e., optical telescopes, would absorb the X-rays instead of reflecting them, so that usually a so-called Wolter-type telescope is used. This kind of telescope uses grazing incidence reflection and a pair of parabolic and hyperbolic mirrors to focus the X-rays. In order to increase the effective area of Wolter-type telescopes, several mirrors are folded within each other (see Fig. 3.1). Beside the increased financial demand, the associated increase of the effective area has a severe drawback as an exact alignment of the individual shells is required for a sharp point spread function (PSF). However, this is technologically impracticable for a large number of shells and misalignment errors cause a wider PSF. Probably even more importantly, a solid mounting of the reflective surface is required to allow accurate shaping and to maintain this shape during the course of the mission. This, in turn, increases the weight of the X-ray telescope, requiring some compromise in trading effective area against angular resolution power. Today's most advanced X-ray telescopes, *Chandra* (see Fig. 3.2), XMM-Newton and Suzaku, differ in exactly this property. The *Chandra* Observatory has four accurately shaped, Iridium coated mirrors on a solid mount. XMM-Newton uses 57 nested shells and Suzaku employs at total of 175 shells. This results in a very sharp PSF in the central field of view (FOV) of *Chandra*, a less sharp PSF for XMM-Newton and an even worse PSF for Suzaku.

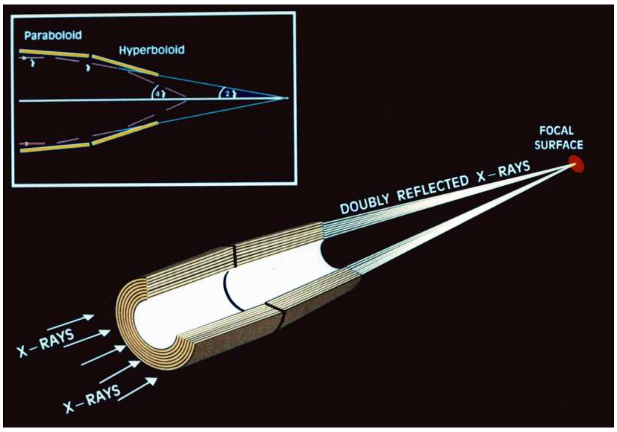

Figure 3.1: Lightpath through a Wolter-type telescope (Image courtesy: ESA).

The associated weight of the *Chandra* mirror and mirror support allows only one X-ray telescope to be carried on board the satellite, while XMM-Newton consists of three X-ray telescopes so that all detectors can operate simultaneously[3]. The *Chandra* focal plane detectors have to be changed by the Science Instrument Module (SIM). It harbors two different types of detectors, the Advanced CCD Imaging Spectrometer (ACIS) consisting of 10 Charged Coupled Devices (CDDs) and the High Resolution Camera (HRC) consisting of seven micro channel plates. The former provides an intrinsic energy resolution of about 50 - 100 eV, while the latter provides practically no intrinsic energy resolution. The HRC has a lower sensitivity than ACIS but, on the other hand, a smaller spatial pixel size.

The pixel size of the ACIS detector (0.492″) is too large to utilize the full resolving power of the superb mirrors of *Chandra*. The half-energy radius is

[1] `http://cxc.harvard.edu`

[2] Smithonian Astrophysical Observatory

[3] The RGS is designed as a reflection grating allowing to be operated in conjunction with the imaging CCDs.

$0.42''$ at $E_{photon} = 1\,\mathrm{keV}$, thus comparable to terrestrial optical observations under excellent seeing conditions without adaptive optics. The intrinsic energy resolution of ACIS allows to separate spatially close-by sources of largely differing spectra by energy filters and is therefore in some cases superior to the HRC-I (the imaging part of the HRC) despite its larger pixels. The power of this approach has been utilized for an analysis of the inner X-ray emission regions of the classical T Tauri star DG Tau in ch. 8.

For observations of faint X-ray sources, the exceptionally low background of the ACIS detector allows to measure source properties with unprecedented detail. Additionally, ACIS can be operated in the so-called `very faint` mode, which means that the 5×5 pixel island surrounding the brightest pixel are telemetered instead of the standard 3×3 pixel island. This allows an improved background reduction by a more robust identification of non X-ray photons, i.e., the particle background which often has a different signature than X-ray photons. The endpoints of particle tracks can resemble the energy distribution of "real" photons when one only considers the central 3×3 pixel island, but differ more strongly from real events when the 5×5 island is considered. Afterglow events result from cosmic rays depositing so much energy in consecutive pixel that a photon event is mimicked in several successive frames. These events are also almost completly identified and rejected in the `very faint` mode. The loss in "real" source photons is usually negligible (1-2%).

My studies of X-ray emission of protostellar jet sources are based on observations with ACIS which is the prime instrument for these studies, as it allows accurate spatially and spectroscopically resolved measurements of the source on a very low background level.

Both focal plane detectors can be used in combination with either the Low or the High Energy Transmission Grating (LETG and HETG). These transmission gratings disperse the incident light and greatly increase the energy resolution for point sources, albeit with a drastically reduced transmission efficiency of roughly 10%. In combination with the HRC-S (the spectroscopic part of the HRC), the LETG covers the 1.2-175 Å wavelength range. This enormous range can provide a strong handle on the absorption in the line of sight towards X-ray emission regions. This property of the LETG is utilized in the paper on AU Mic (see chapter 9), in which the absorption caused by the edge-on disk of AU Mic is investigated. A particular problem for this analysis was the lack of energy resolution of the HRC. As typical for transmission gratings, the individual diffraction orders are spatially superposed, leading to order confusion when the detector lacks sufficient intrinsic energy resolution to separate the individual orders. Another instrumental difficulty is the relatively high background count-rate which results from a weiring error during the assembly of the HRC-S detector. The other grating on-board of $Chandra$ is the HETG which provides two spectra of the highest currently available spectral resolution. However, the available wavelength ranges, covering in total 1.2 – 31 Å, are significantly smaller than that of the LETG.

Figure 3.2: The $Chandra$ X-ray observatory. Credits: NASA/CXC/SAO

4. Overview

My articles deal with the X-ray emission of pre-main-sequence stars, from a very young star and from protostellar jets. Therefore, the articles are ordered according to the (assumed) age of the objects[1] rather than to their chronological order.

Young stellar objects

Chapter 5 deals with the X-ray of Class 0-I objects in Cepheus A (Cep A), and these objects are probably the youngest ones studied in my thesis. Cep A is the second nearest high-mass star forming region. The central part of this region is crowed by different sources of often unknown nature, and the *Chandra* observation of this region has resolved some of the ambiguities. As expected from their evolutionary stage, the objects in this region are highly obscured, which complicates the interpretation of the data. Information from other wavelengths is used to construct a consistent scenario of the processes in this region, e.g., which sources are of stellar nature or relate to protostellar jets.

Protostellar jets

Chapter 6 deals with the X-ray emission of HH 168 which is located within Cep A. This HH object is covered by the same *Chandra* exposure as the central part of Cep A. Although the driving source of this HH object is not known yet, it is very likely that the driving source is also a Class 0-I object, qualifying this article to be presented second. The X-ray emission from this object was known from a previous XMM-Newton observation which indicated that the X-ray emission of HH 168 is extended. The distribution of the X-ray emitting plasma, however, could only be revealed by the new *Chandra* observation.

The subject of ch. 7 is the protostellar jet from L1551 IRS 5 which is another X-ray emitting jet from a very young driving source (probably Class I). The available two *Chandra* observations showed that the bulk of the emission is located close to its driving source in both exposures with differences mainly in the outer part of the jet. This is particularly interesting as shock heating requires the postshock gas to retain at least a quarter of its initial velocity. We obtained a third epoch *Chandra* observation to clarify the nature of this inner jet component and the results of the new observation are presented in ch. 7.

Chapter 8 deals with the X-ray jet of the 1-2 Myr old CTTS DG Tau. This jet is one of the most well studied protostellar jets. In the immediate vicinity of DG Tau, four different X-ray emission regions are located (outer X-ray jet, inner X-ray jet, counter-jet, DG Tau). The detailed analysis of the inner X-ray jet component confirms the claimed jet nature of the soft X-ray emission almost co-spatial with the stellar position.

Debris disks

Chapter 9 presents an application of X-ray transmission spectroscopy to debris disks. The oldest object studied in this thesis is the nearby active M-dwarf AU Mic with an estimated age of approximately 12 Myr. It possesses an edge-on debris disk, and the absorption signatures from the debris disk can, in principle, reveal the chemical composition of the small grains and gas in the disk.

In chapter 10 my work is summarized. A short outlook into the future is given which includes some of my ongoing projects further investigating the nature of the X-ray emission from protostellar jets.

[1] The X-ray emitting plasma within protostellar jets is typically much younger than their driving sources and the age of the associated power source is used for the ordering.

Part II

Publications

5. The *Chandra* X-ray view of the power sources in Cepheus A

P.C. Schneider, H. M. Günther, J. H. M. M. Schmitt
Astronomy & Astrophysics, 508, 321 (2009)

A&A 508, 321–327 (2009)
DOI: 10.1051/0004-6361/200912995

Astronomy & Astrophysics

The *Chandra* X-ray view of the power sources in Cepheus A

P. C. Schneider, H. M. Günther, and J. H. M. M. Schmitt

Hamburger Sternwarte, Gojenbergsweg 112, 21029 Hamburg, Germany
e-mail: [cschneider;hguenther;jschmitt]@hs.uni-hamburg.de

Received 27 July 2009 / Accepted 2 September 2009

ABSTRACT

The central part of the massive star-forming region Cepheus A contains several radio sources which indicates multiple outflow phenomena, yet the driving sources of the individual outflows have not been identified. We present a high-resolution *Chandra* observation of this region that shows the presence of bright X-ray sources with luminosities of $L_X \gtrsim 10^{30}$ erg s^{-1}, consistent with active pre-main sequence stars, while the strong absorption hampers the detection of less luminous objects. A new source has been discovered located on the line connecting H_2 emission regions at the eastern and western parts of Cepheus A. This source could be the driving source of HH 168. We present a scenario relating the observed X-ray and radio emission.

Key words. stars: pre-main sequence – stars: winds, outflows – X-rays: stars – stars: individual: Cep A:HW 2 – ISM: individual objects: Cep A East

1. Introduction

Stars form in collapsing molecular clouds. The largest clouds harbour very massive protostars in addition to the numerous late-type stars. Cepheus A is the second nearest high-mass star forming region at a distance of about 730 pc (Johnson 1957).

The Cep A region contains multiple outflows, e.g. large scale molecular outflows, extending several arcmin (~10^5 AU) from their driving source with velocities of a few 10 km s^{-1}. The complicated outflow geometry has been explained by dense condensations, which redirect the outflow (Codella et al. 2003; Hiriart et al. 2004), but can be also interpreted as independent outflows or by the evolution of a single outflow.

The line of sight towards the centre of Cep A suffers from strong absorption and hampers optical observations of the central sources. From reflected light measurements in the infrared (IR), Lenzen et al. (1984) derived $A_V \gtrsim 75$ while Goetz et al. (1998) estimated $A_V \gtrsim 200$ from their inability to detect the central radio source in their IR-images (assuming a B0-type star). Sonnentrucker et al. (2008) derive the hydrogen absorbing column density from the silicate absorption feature at 9.7 μm to range from a few 10^{22} cm^{-2} to higher than 10^{23} cm^{-2}. Therefore, only radio observations provide detailed maps of this region. Several distinct sources with different apparent sizes and spectral indices have been revealed by cm-wavelength observations (Hughes & Wouterloot 1984; Garay et al. 1996); we also use their nomenclature "HW1...9" to designate radio sources in that region (as sketched in Fig. 1).

The most radio luminous object of these HW-sources is HW 2, which probably harbours a B0.5–B2 star with a mass of about 15–20 $M_\odot$ (Hughes & Wouterloot 1984; Garay et al. 1996; Curiel et al. 2006). This source is usually refered to as the center of the Cep A region. A thermal radio-jet with a position angle of ~45° is present (Curiel et al. 2006), indicated by arrows in Fig. 1. It is probably related to (at least) one part of the large scale molecular outflow, which has a similar position angle and is directed towards HW 2. The jet contains knots moving with velocities of about 500 km s^{-1} as derived from high

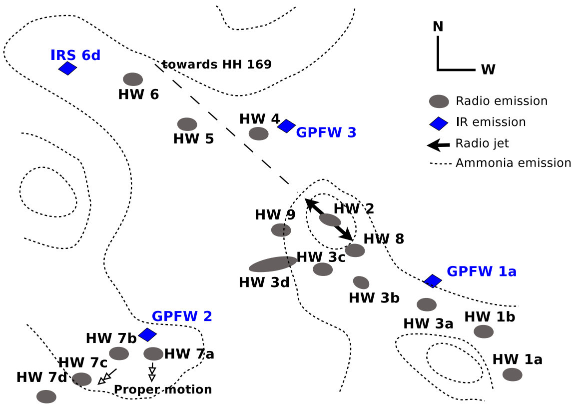

Fig. 1. Sketch of some emission sources in the Cep A region. See Fig. 2 for the exact location of the individual sources. The ammonia emission is sketched from the observations of Torrelles et al. (1993).

resolution cm-wavelength observations (Curiel et al. 2006). Some of the radio sources, located approximately in the direction of this jet at distances of a few 10 arcsec (HW 1, HW 4, HW 5 and HW 6), are likely shock-induced free-free emission components (with non-thermal contributions) powered by the HW 2 jet (Garay et al. 1996). There has been some debate on the interpretation of the observations very close to HW 2 itself. Some observations indicate the presence of a disk (e.g. HCO^+, SiO, CH_3CN, SO_2, 335 GHz continuum; Torrelles et al. 1996; Gómez et al. 1999; Patel et al. 2005; Jiménez-Serra et al. 2007; Torrelles et al. 2007, respectively), while signatures of radio emission explained by the presence of young stellar objects (YSOs) have also been found (Curiel et al. 2002; Brogan et al. 2007; Comito et al. 2007). Jiménez-Serra et al. (2007) show that disk signatures are present very close to HW 2, suggesting a disk with a size of about 600 AU.

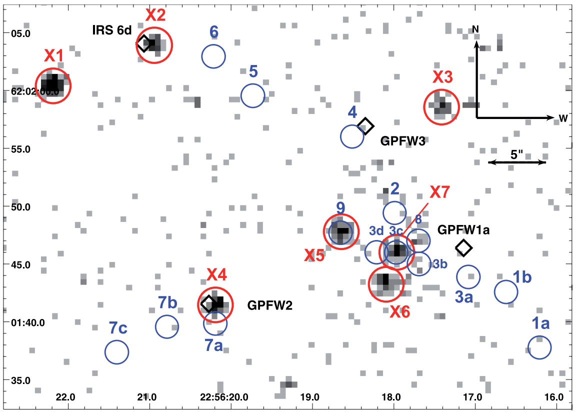

Fig. 2. X-ray image (1.5–9 keV) of the central region of Cep A. The radii of the blue circles designating the radio sources are 1.0 arcsec while that of the red circles naming the X-ray sources are 1.5 arcsec. Numbers indicate HW radio sources. The blacks diamonds are selected infrared sources.

The radio complex HW 3, located 3–4 arcsec south of HW 2 (see Fig. 1), constitutes an elongated structure oriented primarily in the east-west direction, which is resolved at higher resolutions. Due to their spectral properties and dense cores or association with masers, all subcomponents have been proposed to harbour an internal energy source; i.e., they could be associated with an YSO (e.g. Hughes 2001; Garay et al. 1996; Brogan et al. 2007). However, there is no consensus about their nature in the literature. In the vicinity of HW 3a, 3b and 3d water maser activity has been found (Cohen et al. 1984; Torrelles et al. 1998), while HW 3c has an associated submillimetre core (Brogan et al. 2007) and a composite spectrum, suggesting the presence of a jet (Hughes 2001). HW 3a breaks up into two time-variable components; one might be associated with an infrared source (GPFW 1a (diamond in Fig. 1): Goetz et al. 1998; Lenzen 1988; Garay et al. 1996; Hughes 1997). HW 3d also breaks up into at least four distinct objects in high-resolution observations.

HW 8 and HW 9, located close to HW 2 and HW 3 (a few arcsec distance), are two relatively compact radio sources, showing large variations in their flux densities and are therefore assumed to be associated with low-mass pre-main sequence stars (Hughes 2001; Garay et al. 1996).

HW 7 consists of several radio emission regions about 20″ south-east of HW 2. The main components b, c and d are aligned at a position angle of 107°, pointing towards just south of HW 2 at one of the HW 3 sources. Therefore, Garay et al. (1996) proposed that HW 3d drives an outflow directed towards HW 7, which is interpreted as shock induced radio emission. From their proper motion measurements of the individual components of HW 7, Curiel et al. (2006) propose that the driving source is located just north of the HW 7a component, mainly because HW 7a moves almost perpendicularly to the rest of the HW 7 sources due south. We identify this source with GPFW 2 (Goetz et al. 1998).

Just as radio waves, X-rays penetrate through a high absorbing column density and are therefore a useful tool to disentangle individual emission components. In the case of Cep A, B-type stars are potentially associated with the radio sources. They have a typical X-ray luminosity of $\sim 10^{30}$ erg s^{-1} for late B stars and up to $\sim 10^{32}$ erg s^{-1} for B0 stars (Berghoefer et al. 1997). The L_X/L_{bol} ratio increases from 10^{-7} for mid-B stars to higher values for A stars and later objects. A-type stars have X-ray luminosities of usually just below 10^{30} erg s^{-1} and later stars, even young M-dwarfs, can easily emit more than 10^{29} erg s^{-1} (Preibisch et al. 2005). Typical mean plasma temperatures for later-type stars are about 1.4 keV, while early-type stars can have relatively low temperatures of only a few 0.1 keV. A study of young O and B-type stars in the Orion nebula (Stelzer et al. 2005) showed that a second temperature component around 2 keV is mostly present in the early and mid B-type stars.

Although column densities above 10^{23} cm^{-2} almost completely absorb any soft stellar X-ray emission ($E < 1$ keV), higher energy photons remain detectable in the *Chandra* observation. Cep A was already observed by *XMM*-Newton (Pravdo & Tsuboi 2005). That observation found hard X-ray emission from the region around HW 2, but was not able resolve the individual sources due to the large point-spread function (PSF) of *XMM*-Newton; the authors speculate that deeply embedded protostars or high-velocity outflows might be responsible for the observed X-ray emission.

The focus of this article is to use *Chandra*'s high angular resolution to disentangle the sources in the central region of Cep A.

2. Observation, data processing and analysis

2.1. Observation

Chandra observed Cep A on 2008-04-08 for 80 ks with ACIS-I (Obs-ID 8898). The analysis was carried out using CIAO 4.1.2 and the science threads published at CIAO website[1]. The data was not reprocessed, i.e., standard parameters like pixel randomisation are applied to the data.

2.2. Processing

For point source analysis, the extraction regions were chosen to contain about 90% of the source photons (1.5 arcsec circles). The energy range for our analysis is 0.3 keV to 9.0 keV; we therefore define a low band from 0.3 keV to 1.5 keV and a high band from 1.5 keV to 9.0 keV. We used a background region which contains 72 photons in a circle of 11 arcsec radius (48 photons in the high band). The estimated background within the extraction regions of the individual sources is therefore about 1.3 counts in total, 0.9 photons of them in the high band. To derive the statistical significance of a source at a specific position, i.e., the probability to find a source at a given position by chance, we run a source detection algorithm (`celldetect`) on the central field of view (three arcmin radius), where the PSF is still narrow. In this region 34 (25) sources with a S/N value above 3(4) are present (not to be mistaken as the significance of the source[2]). The source with the lowest S/N discussed in the following is found by the source detection algorithm at $S/N = 1.7$. Within the 3 arcmin radius 68 sources were then found. Corrected for the chip gaps, statistically fewer than 0.01 sources are expected within the extraction region at any position specified a priori.

XSPEC v12.3.1x (Arnaud 1996) was used to estimate the plasma properties of the individual sources. For the spectra an absorbed plasma emission model (APEC, Smith et al. 2001) was chosen. Errors denote 1σ confidence ranges and quoted X-ray

[1] http://cxc.harvard.edu/ciao/
[2] http://cxc.harvard.edu/ciao/download/doc/detect_manual/index.html

Table 1. X-ray properties of X-ray, radio and infrared sources in the region around HW 2/3.

Source ID	Radio ID	Infrared ID	RA	Dec	Counts[a]	Median energy[b]	Temperature kT (keV)	Absorption 10^{22} cm^{-2}	Luminosity $\log L_X$ (erg s^{-1})	Radio flux (mJy)	Spectral index	Infrared mag[c]
X1		IRS 6b	22:56:22.2	+62:02:00.5	137	2.3	2.0–3.0	1.4–2.2	30.7–30.9	–		8.4
X2		IRS 6d	22:56:20.9	+62:02:04.0	44	4.2	2.0[e]	10–18	30.9–31.1	–		11.1
							1.0[e]	20 – 32	32.0–32.3			
X3		?[d]	22:56:17.4	+62:01:58.6	36	4.3	2.0[e]	10–18	30.9–31.1	–		
							1.0[e]	17–26	31.8–32.1			
X4		GPFW 2	22:56:20.2	+62:01:41.4	64	3.9	0.9–1.7	11–32	31.2–32.3	–		15.6
X5	9		22:56:18.6	+62:01:47.8	60	4.1	0.7–1.3	20–38	31.8–33.4	3.0	–0.2	
X6			22:56:18.1	+62:01:43.2	50	5.5	2.0[e]	32–50	31.5–31.8	–		
							1.0[e]	61–83	33.1–33.4			
X7	3c		22:56:18.0	+62:01:46.0	60	6.4	2.0[e]	62–106	32.1–32.5	3.7	0.4	
							(1.0[e]	127–175	34.0–34.5)[f]			
	1a		22:56:16.2	+62:01:37.8	2		–		<29.8 (30.5)	2.2	–0.6	
	1b		22:56:16.6	+62:01:42.6	2		–		<29.8 (30.5)	2.9	–0.3	
	2		22:56:19.0	+62:01:49.4	<4		–		<30.0 (30.7)	7.5	0.7	
	3a	GPFW 1a?	22:56:17.1	+62:01:43.9	1		–		<29.6 (30.3)	0.2	–	14.7
	3b		22:56:17.7	+62:01:45.0	6	4.6	–		29.9 (30.6)	5.0	0.0	
	3d		22:56:18.2	+62:01:46.0	3		–		<29.9 (30.6)	7.7	0.3	
	4	GPFW 3	22:56:18.5	+62:01:56.0	1		–		<29.6 (30.3)	4.4	–0.2	12.6
	5		22:56:19.7	+62:01:59.5	1		–		<29.6 (30.3)	1.3	–0.5	
	6		22:56:20.2	+62:02:03.0	0		–		<29.2 (29.9)	3.8	–0.3	
	7a		22:56:20.2	+62:01:39.9	2		–		<29.8 (30.5)	9.6	–0.1	
	7b		22:56:20.8	+62:01:39.6	1		–		<29.6 (30.3)	2.8	–0.4	
	7c		22:56:21.4	+62:01:37.4	0		–		<29.2 (29.9)	3.8	–0.4	
	7d[g]		22:56:21.9	+62:01:36.5	1		–		<29.7 (30.4)	2.4	–	
	8		22:56:17.7	+62:01:47.0	9	6.2	–		30.1 (30.8)	<0.12	–	
		IRS 6c	22:56:17.5	+62:01:51.1	1		–		<29.6 (30.3)	–		8.5[h]

[a] Including a background of 1.3 cts; [b] in keV; [c] *K*-band; [d] visible in the Goetz et al. (1998) IR-images; [e] fixed; [f] this value is unlikely high for a stellar source, see Sect. 3.2.2; [g] data from Hughes & Wouterloot (1984); [h] *L*-band.

luminosities are dereddened luminosities in the 0.3–10.0 keV band.

2.3. Data analysis

In Fig. 2 an overview of the central region of Cep A in the high band is shown. All X-ray sources are visible; no source in this region is present only in the low band. The locations of radio sources and infrared point-like sources are also indicated (cf. sketch in Fig. 1). We summarise the properties of the X-ray sources (detected with a S/N ratio above 3 by `celldetect`) in Table 1, where cross-IDs, position, plasma parameters, radio fluxes and infrared luminosities for the detected X-ray sources and limits for the non-detections are given. Infrared magnitudes were taken from Lenzen et al. (1984) for the IRS sources and from Goetz et al. (1998) for the GPFW sources; radio fluxes are from Garay et al. (1996). The source position is either given by the location of the respective radio source or by the detection algorithm. The source positions were slightly (<0.4 arcsec) adjusted to contain a larger number of counts for X5 and X6 (only towards the south). The large extinction towards the centre of Cep A (Sonnentrucker et al. 2008) absorbs the low-energy X-ray emission from embedded stars and only the high band remains observable. A plasma with an equilibrium electron temperature of 1 keV still radiates 13% of its energy-loss (3% of the photons) in that band. A source with a large fraction of low energy photons would be a foreground object, while an object with only high energy photons is either located within the cloud or a background object.

Due to the strong absorption, only a relatively low number of counts is available for the individual sources. Figure 3 illustrates the uncertainties of the basic plasma parameters derived for the four most luminous X-ray sources. From this figure it is clear that a more detailed spectral analysis of sources with even fewer counts does not lead to additional insights, since the errors in the parameters already span about an order of magnitude. The spectra of all sources can be characterised by strong absorption. Virtually any low energy X-ray emission is absorbed, except for X1. This source is absorbed by a column density about an order of magnitude lower than all other X-ray sources. In the case of stars, the detected X-ray emission represents the high energy component of the plasma. Those sources (X3, X6 and X7) with the highest median photon energies do not sufficiently restrict the plasma temperature. Best fit temperatures well above 10 keV are unlikely for the dominating plasma component of (quiescent) stellar sources. Plasma temperatures above 10 keV are rare even for large flares. Therefore, an estimate for the temperature of the hot plasma component is needed, whenever a reasonable fit value is not available. The high temperature component of B-type stars is usually around 2 keV (Stelzer et al. 2005). We use this as an estimate of the plasma temperature. For comparison we also give the values for $kT = 1.0$ keV. The fits of those sources with a relatively high count number show similar values. Both temperatures are commonly found for pre-main sequence stars and therefore can be used as an estimate of the plasma temperature almost independently of spectral type. The unabsorbed luminosity depends strongly on the adopted absorption (see Fig. 3 for examples). We therefore give only the range of luminosities corresponding to the lowest and the highest absorption columns (1σ). For those sources without a reasonable temperature value, a temperature of $kT = 2$ keV was assumed and used to estimate the absorption and the unabsorbed X-ray

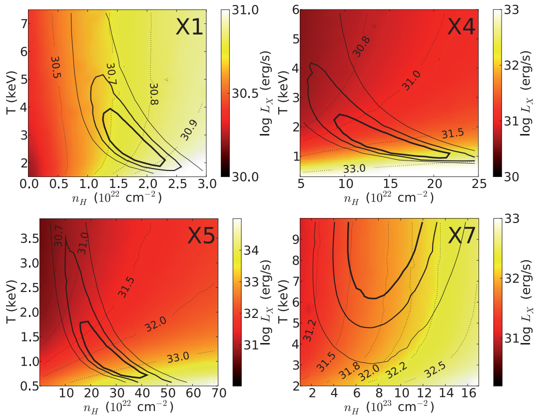

Fig. 3. Confidence ranges of the important spectral properties of the four brightest sources. The X-ray luminosity is displayed colorcoded and as dotted contours. The range of spectral parameters differs between the sources.

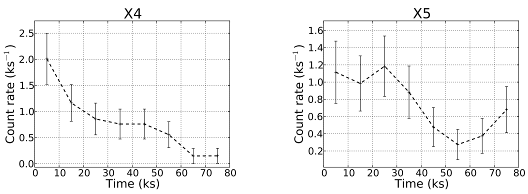

Fig. 4. X-ray lightcurves for the sources X4 and X5 (10 ks binning).

luminosity; the derived values for $kT = 1$ keV are given in brackets.

The lightcurves of the individual objects (Fig. 4) show some variability, but no flare can be clearly recognised. Usually, flares are also associated with an increase in the median photon energy. Due to the lack of any detected soft emission and the low number of counts, such a signature is not significantly seen except, possibly, in the source X4, which show a monotonic decrease in X-ray luminosity resembling the decay phase of a large flare. During the first half of the observation the photons exhibit a higher value of the mean energy ($kT \approx 4.4$ keV, 46 photons) than during the second half ($kT \approx 4.0$ keV, 18 photons).

Upper limits on the X-ray flux of the non-detected radio sources are estimated by assuming a plasma temperature of $kT = 2.0$ keV (1.0 keV) and an absorbing column density of $n_{\rm H} = 10^{23}$ cm^{-2}. The maximum source count rate was chosen to be such that for the given limiting X-ray luminosity in 90% of the realisations the number of detected photons would be higher than observed. A typical source count number of three photons corresponds to $L_{\rm X} = 4.8 \times 10^{29} (2.2 \times 10^{30})$ erg s^{-1}.

There appears to be no correlation between X-ray and radio luminosity for the sources. The X-ray detected radio sources are neither the radio brightest ones nor outstanding in terms of their spectral indices.

3. Results and individual sources

We group the sources depending on their association with radio and infrared emission, starting with the non-detection of the prominent radio source HW 2 (see Figs. 1 or 6 for a sketch).

3.1. The non-detection of HW 2

The central component of the HW 2 emission is not significantly detected in X-rays, only one photon is observed within a radius of 1 arcsec, where 0.6 photons are expected from the background. Enlarging the extraction region to a radius of 1.5 arcsec also increases the count number to three but overlaps with a source towards the north-east (whose photons are not included). Therefore, the number of source photons is very likely no more than two. Taking the absorption column density for the region of HW 2 from Sonnentrucker et al. (2008) of 1.3×10^{23} cm^{-2}, the upper limit for the X-ray luminosity of HW 2 is 8×10^{29} erg s^{-1}, assuming a plasma temperature of 2.0 keV. This luminosity is about two orders of magnitude lower than that of a typical mid B-type star since a luminosity of up to $\sim 10^{32}$ erg s^{-1} is reasonable for massive stars. In this case, the absorbing column density needs to be $> 2 \times 10^{24}$ cm^{-2} with the other parameters as in the first case to explain the non-detection of HW 2; this value would correspond to $A_V \gtrsim 1000$ according to Vuong et al. (2003). We infer that the absorbing column density towards HW 2 needs to be above a few times 10^{23} cm^{-2} to hide any X-ray emission from the presumed B-type star with a 2 keV plasma component.

3.1.1. The HW 2 jet in X-rays?

The proper motion of the resolved radio jet of HW 2 is about 500 km s^{-1} (Curiel et al. 2006) and therefore sufficient to produce X-rays, when ramming into a medium at rest. Interpolating the apparently linear motion of the radio emitting knots to the date of the *Chandra* observation (year 2008), we expect the two outer knots at a separation of 2.0 arcsec south-west and 1.8 arcsec north-east from HW 2, respectively (see Fig. 6). Unfortunately, the radio source HW 8 is located exactly where the south-west knot is predicted. Although no definite explanation for the nature of this highly variable radio source is known, it is likely a pre-main sequence star and also the emitter of the weak X-ray emission at this position. This interpretation is supported by the high median energy of the excess emission. A plasma produced by a shock speed of 500 km s^{-1} needs to be very luminous to account for the observed hard emission, because the peak of the emission is absorbed and only the highest energy tail remains observable.

At the position of the north-eastern X-ray emission neither radio nor infrared sources are known. The seven photons at exactly the expected position of the radio knot are softer than the south-western ones (median energies of 4.4 keV and 6.2 keV). Assuming that (at least) the north-eastern X-rays are indeed produced by shocks, what does this imply for the shock luminosity? The velocity of the radio components (500 km s^{-1}) gives a plasma temperature of $kT = 0.3$ keV using the formula of Raga et al. (2002). The absorption is unknown, but assuming a value of $n_{\rm H} = 4 \times 10^{23}$ cm^{-2}, which is on the same order as the value derived by Sonnentrucker et al. (2008) and compatible with the value found for HW 3c, implies a luminosity of 10^{35} erg s^{-1}. Such a high luminosity would require a very efficient process transforming kinetic energy into X-ray emission. For a plasma temperature, on the other hand, of 1.2 keV, the luminosity drops by four orders of magnitude, but requires a high velocity component ($v \sim 1000$ km s^{-1}), embedded in the material observed at radio wavelengths. Such an onion-like structure has been seen in DG Tau (Bacciotti et al. 2002). Using the Günther et al. (2009) formula for the mass loss $\dot{M}$ (Eq. (6)), we find $\dot{M} \approx 2.5 \times 10^{-5}\ M_\odot\,{\rm yr}^{-1}$ for the lower temperature and five orders of magnitude smaller for the higher temperature. While the first value is probably too high, the lower value can be easily achieved by pre-main sequence stars like HW 2. The possibility that the source is a positional chance coincidence is below 1% (see Sect. 2.2).

The relatively low median energy of the weak excess X-ray emission at exactly the position of the north-eastern radio knot points to shock-induced emission, but requires a higher shock-speed than the velocity of the radio knots. Otherwise the required luminosity is implausibly high. Therefore, either these X-ray photons are caused by an unknown embedded pre-main sequence star, located at the opposite position of HW 8 with respect to HW 2, or these photons are indeed caused by the fastest component of the HW 2 jet.

3.2. Sources associated with radio sources

The following X-ray sources are associated with radio emission components.

3.2.1. HW 9 and HW 8

The X-ray source X5 clearly coincides with the radio source HW 9. The derived absorbing column density is a few times higher than the value derived by Sonnentrucker et al. (2008), compatible with circumstellar matter as expected for the early evolutionary stage of this star. The X-ray light curve shows a variation in the count rate of a factor of three (see Fig. 4). Although the shape of the lightcurve does not resemble that of large flare events, such variations are typical for young active stars. The unabsorbed luminosity of 5×10^{32} erg s^{-1} is on the high side for massive stars but not implausible. All these properties support the idea that HW 9 is of stellar origin (probably of spectral type B), which is in line with the expectations from radio observations (Hughes et al. 1995; Garay et al. 1996).

At the location of HW 8 a clear photon excess is found (see Sect. 3.1.1). The nine photons at the expected position have a very high value of the median energy (6.2 keV) and suggest an interpretation in terms of an embedded pre-main sequence star. Its X-ray luminosity would be 10^{30} erg s^{-1} for an absorbing column density of 10^{23} cm^{-2} and $kT = 2.0$ keV.

3.2.2. HW 3b/c (X7)

The identification of the radio counterpart of X7 is not clear, but it is located closest to HW 3c. Therefore, we favour an association with HW 3c, which is also associated with SMA 875 μm emission (Brogan et al. 2007). From the X-ray point of view HW 3c can be characterised by an even higher absorbing column density than HW 9 (X5). The unabsorbed luminosity, assuming a plasma temperature of $kT = 1.0$ keV, is unreasonably high for a stellar source or a shocked outflow. Consequently, we favour a model with a higher temperature and less absorption and consequently lower X-ray luminosity. No X-ray photon with an energy lower than 5 keV has been detected. The iron line emission complex around 6.7 keV contributes a large fraction of the observed emission indicative of hot plasma, arguing for a thermal emission component rather than a power-law spectrum. The radio component 3b also shows a weak excess X-ray emission of six photons with a lower value of the median energy than HW 3c.

In particular, a subcomponent of HW 3d was suspected to be a protostar, driving a jet with a position angle of about 100° (Garay et al. 1996; Torrelles et al. 1998; Goetz et al. 1998), and therefore a candidate for driving the large scale east-west outflow. This source is not detected in X-rays, possibly HW 3d constitutes only shock induced radio emission without any stellar core. HW 3a is located further westwards than the other HW 3 radio sources, and might be associated with an infrared source (GPFW 1a, Goetz et al. 1998) without any significant excess X-ray emission. Still, the same arguments presented in the discussion of the non-detection of HW 2 (Sect. 3.1) apply here: Low-mass YSOs cannot be detected with the available observation, if the strong absorption towards HW 3c is also present towards the other HW 3 components.

3.3. Sources with infrared counterparts

In the field presented in Fig. 2 four X-ray sources can be identifies with infrared sources.

3.3.1. X4

This source is probably associated with the infrared source GPFW2 (Goetz et al. 1998), which lies at the tip of the radio complex HW 7. Rodríguez et al. (2005) analysed the proper motions of the individual knots of the HW 7 radio emission complex and postulated that the driving source is located close to the position of X4. We follow this interpretation and regard the radio emission of the HW 7 emission complex as shock heated material (as also proposed by Garay et al. 1996; Goetz et al. 1998). The X-ray source itself is absorbed less than those sources close to HW 2 and HW 3. The average luminosity of $L_X \approx 10^{31}$ erg s^{-1} is very high for a low-mass star, but the lightcurve shows a continuous decrease in count rate during the observation (Fig. 4). We interpret it as the decay phase of a strong flare, supported by the lower mean energy of the photons in the second part of the observation (see Sect. 2.3). Therefore, the quiescent luminosity of this object is probably significantly lower than the value derived here, thus also a low-mass star can produce the observed X-ray emission.

3.3.2. X1, X2 and X3

The X-ray source X1 exhibits the lowest values for the median energy and the fitted absorbing column density ($n_H = 1.6 \times 10^{22}$ cm^{-2}). Its X-ray luminosity of 6×10^{30} erg s^{-1} is relatively low in this sample, but still about ten times higher than the median luminosity of the sources in the *Chandra* Orion Ultra Deep project, where a star forming region (Trapezium region) in the Orion Nebula cloud was observed for 730 ks (COUP Getman et al. 2005); only a tenth of the COUP sources exceed this value. X1 is also visible in the infrared images of Lenzen et al. (1984) as IRS 6b. These properties point to an object located on the near side of the cloud.

The source X2 is located in the direction of the north-eastern outflow of HW 2 and probably the infrared source IRS 6d. It is again deeply embedded, and the lower limit of the absorption is about 7×10^{22} cm^{-2}, which matches the expected value at that position. Its high X-ray luminosity ($L_X \gtrsim 3 \times 10^{30}$ erg s^{-1}) again points to an embedded massive protostar, the coincidence with the outflow is probably a projection effect.

X3 can be characterised by an absorbing column density on the order of a few 10^{22} cm^{-2} and a luminosity of 8×10^{30} erg s^{-1} for a temperature of 2 keV. It is again, most probably, a massive pre-main sequence star. In Fig. 4 of Goetz et al. (1998) this source seems to be also present as an infrared source, but is not noted as a source by these authors.

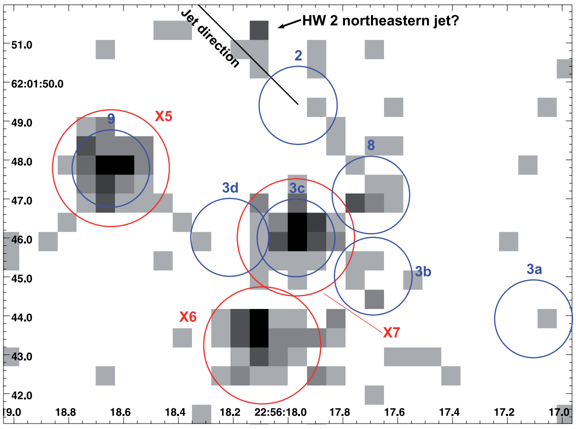

Fig. 5. Zoom into Fig. 2 for the region around HW 2 and HW 3. Large circles indicate X-ray sources and small circles are radio sources.

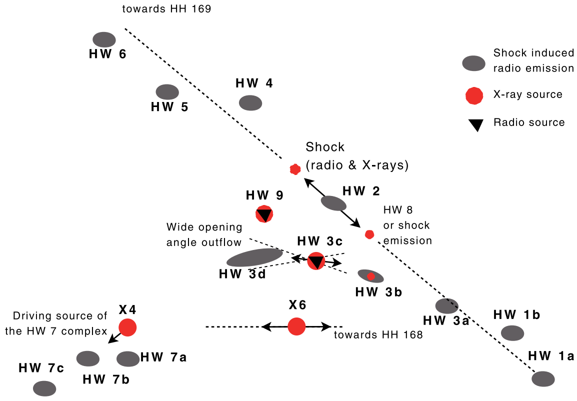

Fig. 6. Sketch of a possible scenario. Stellar sources are seen in X-ray and radio emission. The outer jets are mostly found in radio observations, while X-rays originate only close to the jet driving source.

3.4. Source without any counterpart (X6)

The most interesting source in the region unrelated to any radio or infrared source is X6. It is located 2.5 arcsec south of the HW 3 radio emission complex or about 5 arcsec south of HW 2. With a median energy of 5.5 keV, its X-ray spectrum is very hard pointing to a deeply embedded source. The minimum absorbing column density required to explain the spectrum is 3×10^{23} cm^{-2} for a fixed temperature of 2.0 keV. This source appears to be slightly extended towards the west, i.e., into the direction of HH 168, where an excess of about 3 photons is seen (see Fig. 5). The available data is not sufficient to exclude the presence of a second object close to the bulk emission causing the distorted structure of this source. Due to the low count number source variability cannot be excluded. This sources lies close to the connecting line of an H_2 emission complex in the west associated with HH 168 and an H_2 complex at the eastern side. Cunningham et al. (2009) estimated the distance of the connecting line to be 5–10 arcsec south of HW 2, which is exactly the value of X6. Thus, X6 is possibly driving the HH 168 outflow.

3.5. Non-detection of the other radio sources

From the radio sources which were suspected to harbour an internal power source (Garay et al. 1996), HW 2, 3a and 3d do not show up in X-rays. The non-detection HW 2 can be easily attributed to the extensive absorbing column density, and HW 3a might simply be too dim for a detection with the available data. It was suggested that this source is a low-luminosity star and thus probably does not reach an X-ray luminosity of a few 10^{29} erg s^{-1} as required for a detection; on the other hand, the radio flux density is higher than in HW 3c, which shows strong X-ray emission.

As B-type stars might potentially exhibit rather soft X-ray spectra, the *Chandra* observation cannot exclude the presence of such stars, since the required X-ray luminosity to shine through an absorbing column density of 10^{23} cm^{-2} for a temperature of only 0.3 keV is 3×10^{32} erg s^{-1} which might not be reached by the B-type star. Therefore, in the case of HW 3d, a B-type star can be related to the observed radio emission, although it is not detected in X-rays.

All other radio sources, in particular the HW 7 complex and HW 4, 5, 6 and 1a/b have been interpreted as shock emission (Garay et al. 1996). The non-detection in X-rays is therefore in line with the expectation for these radio sources.

4. Summary and conclusion

Our analysis of the high resolution X-ray observation of the central region of Cep A relates the detected X-ray sources with known radio and infrared sources of that region. Prior to the *Chandra* observation only very few radio sources had possible counterparts at other wavelengths. X-rays are thus the second energy regime in which more of these sources are detected.

In Fig. 6 a sketch of a possible scenario including X-ray and radio sources in the central region of Cep A is shown. This scenario differs in some respects from the Goetz et al. (1998) picture, but follows the main ideas presented there. The driving source for HH 169 and HH 174, located in the eastern part of Cep A, remains the precessing jet of HW 2 (Cunningham et al. 2009). Although HW 2 is undetected in X-rays, X-ray emission at the expected position of the radio knot within the HW 2 jet is compatible with this scenario. Unfortunately, HW 8 coincides with the expected position of the counter jet and hence prevents us from drawing any conclusion on the origin of the X-ray emission observed at that position. Also, none of the suspected sources in the vicinity of HW 2 are detected, which can be explained by a very high absorbing column density, but requires that *all* those sources are deeply embedded. IRS 6d is located approximately in the direction of the outflow and also shows X-ray emission (X2), but is probably unrelated to the outflow as its shape is consistent with a point-like source. Furthermore, the non-detection of any of the radio sources, which are located in the direction of the HW 2 jet (HW 1, 4–6), supports the shock interpretation of these radio sources.

The south-eastern radio complex HW 7 has been also interpreted in terms of shock action, supported by the detection of IR line emission at the tip of this emission complex. The individual components show proper motions pointing to a driving source close to HW 7a (Rodríguez et al. 2005), which we identify with X4 (GPFW 2), while Goetz et al. (1998) proposed HW 3d as the driving source. The X4 lightcurve resembles the decay phase of typical flares of active pre-main sequence stars (Fig. 4), which are known to eject powerful outflows.

For the westward directed outflow (HH 168), another driving source than HW 2 is probably needed, since the position angle of

HH 168 with respect to HW 2 differs significantly from that currently observed for its jet. The desired driving source might be HW 3c, the newly discovered X-ray source X6, or a combination of both. The source of this outflow was not discussed by Goetz et al. (1998), but Cunningham et al. (2009) state that HW 3c is a good candidate for the driving source as also a blue shifted eastward directed CO lobe emerges from the location of HW 3c. We speculate that the absence of X-ray emission from the radio complex HW 3d could be explained by interpreting these clumps (also located east of HW 3c) as dense condensations, heated by the outflow of HW 3c (thermal jet emission), while the weak X-ray emission at the position of HW 3b does indeed represent a star. An opening angle of approximately 20° (position angle of 90°) suffices to excite the individual clumps of the HW 3d complex. This model would be in line with the interpretation of Brogan et al. (2007), who detected submillimetre emission towards HW 3c, but not towards HW 3b or 3d. However, the origin of the water maser emission within the HW 3d complex remains unclear in this scenario. The X-ray source X6 has no counterpart at any wavelength and seems to be elongated towards the west. As it lies closer to the connecting line of HH 168 and its counter outflow, it could also be the driving source. If the opening of the HW 3c outflow is indeed as large as 20°, it is unlikely o drive the large scale outflow, which is more collimated, and X6 would be the natural candidate for driving HH 168.

In summary, the *Chandra* observation of Cep A detected two of three potential driving sources in the region. HW 3c and the driving source of the HW 7 complex (X4) show the characteristic X-ray properties of pre-main sequence stars. The source of the massive north-east outflow (HW 2) cannot be detected in X-rays, which is explained by the strong absorption towards that position. The X-ray source X6 provides a new candidate for the driving source of HH 168, for which observations at other wavelengths are highly desirable.

Note added in proof. After acceptance of this article Pravdo et al. (2009) published an analysis of the same X-ray data on astro-ph. Their results concerning the power sources of Cep A are compatible with ours, they also report the non-detection of HW 2, find the new X-ray source X6 (their source h10), and infer X-ray luminosities of $\log L_{\mathrm{X}} \gtrsim 31$ and plasma temperature above 1 keV for the central sources (see our Table 1).

Acknowledgements. This work has made use of data obtained from the *Chandra* data archive. P.C.S. acknowledges support from the DLR under grant 50OR0703. H.M.G. acknowledges support from the DLR under grant 500R0105.

References

Arnaud, K. A. 1996, in Astronomical Data Analysis Software and Systems V, ed. G. H. Jacoby, & J. Barnes, ASP Conf. Ser., 101, 17
Bacciotti, F., Ray, T. P., Mundt, R., Eislöffel, J., & Solf, J. 2002, ApJ, 576, 222
Berghoefer, T. W., Schmitt, J. H. M. M., Danner, R., et al. 1997, A&A, 322, 167
Brogan, C. L., Chandler, C. J., Hunter, T. R., Shirley, Y. L., & Sarma, A. P. 2007, ApJ, 660, L133
Codella, C., Bachiller, R., Benedettini, M., et al. 2003, MNRAS, 341, 707
Cohen, R. J., Rowland, P. R., & Blair, M. M. 1984, MNRAS, 210, 425
Comito, C., Schilke, P., Endesfelder, U., Jiménez-Serra, I., & Martín-Pintado, J. 2007, A&A, 469, 207
Cunningham, N. J., Moeckel, N., & Bally, J. 2009, ApJ, 692, 943
Curiel, S., Trinidad, M. A., Cantó, J., et al. 2002, ApJ, 564, L35
Curiel, S., Ho, P. T. P., Patel, N. A., et al. 2006, ApJ, 638, 878
Garay, G., Ramirez, S., Rodriguez, L. F., Curiel, S., & Torrelles, J. M. 1996, ApJ, 459, 193
Getman, K. V., Flaccomio, E., Broos, P. S., et al. 2005, ApJS, 160, 319
Goetz, J. A., Pipher, J. L., Forrest, W. J., et al. 1998, ApJ, 504, 359
Gómez, J. F., Sargent, A. I., Torrelles, J. M., et al. 1999, ApJ, 514, 287
Günther, H. M., Matt, S. P., & Li, Z.-Y. 2009, A&A, 493, 579
Hiriart, D., Salas, L., & Cruz-González, I. 2004, AJ, 128, 2917
Hughes, V. A. 1997, ApJ, 481, 857
Hughes, V. A. 2001, ApJ, 563, 919
Hughes, V. A., & Wouterloot, J. G. A. 1984, ApJ, 276, 204
Hughes, V. A., Cohen, R. J., & Garrington, S. 1995, MNRAS, 272, 469
Jiménez-Serra, I., Martín-Pintado, J., Rodríguez-Franco, A., et al. 2007, ApJ, 661, L187
Johnson, H. L. 1957, ApJ, 126, 121
Lenzen, R. 1988, A&A, 190, 269
Lenzen, R., Hodapp, K.-W., & Solf, J. 1984, A&A, 137, 202
Patel, N. A., Curiel, S., Sridharan, T. K., et al. 2005, Nature, 437, 109
Pravdo, S. H., & Tsuboi, Y. 2005, ApJ, 626, 272
Pravdo, S. H., Tsuboi, Y., Uzawa, A., & Ezoe, Y. 2009, ApJ, 704, 1495
Preibisch, T., Kim, Y.-C., Favata, F., et al. 2005, ApJS, 160, 401
Raga, A. C., Noriega-Crespo, A., & Velázquez, P. F. 2002, ApJ, 576, L149
Rodríguez, L. F., Torrelles, J. M., Raga, A. C., et al. 2005, Rev. Mex. Astron. Astrofis., 41, 435
Smith, R. K., Brickhouse, N. S., Liedahl, D. A., et al. 2001, ApJ, 556, L91
Sonnentrucker, P., Neufeld, D. A., Gerakines, P. A., et al. 2008, ApJ, 672, 361
Stelzer, B., Flaccomio, E., Montmerle, T., et al. 2005, ApJS, 160, 557
Torrelles, J. M., Verdes-Montenegro, L., Ho, P. T. P., Rodriguez, L. F., & Canto, J. 1993, ApJ, 410, 202
Torrelles, J. M., Gomez, J. F., Rodriguez, L. F., et al. 1996, ApJ, 457, L107
Torrelles, J. M., Gómez, J. F., Garay, G., et al. 1998, ApJ, 509, 262
Torrelles, J. M., Patel, N. A., Curiel, S., et al. 2007, ApJ, 666, L37
Vuong, M. H., Montmerle, T., Grosso, N., et al. 2003, A&A, 408, 581

6. Chandra observation of Cepheus A: The diffuse emission of HH 168 resolved

P.C. Schneider, H. M. Günther, J. H. M. M. Schmitt
Astronomy & Astrophysics, 508, 717 (2009)

A&A 508, 717–724 (2009)
DOI: 10.1051/0004-6361/200912890

Astronomy & Astrophysics

Chandra observation of Cepheus A: the diffuse emission of HH 168 resolved

P. C. Schneider, H. M. Günther, and J. H. M. M. Schmitt

Hamburger Sternwarte, Gojenbergsweg 112, 21029 Hamburg, Germany
e-mail: [cschneider;hguenther;jschmitt]@hs.uni-hamburg.de

Received 14 July 2009 / Accepted 25 August 2009

ABSTRACT

X-ray emission from massive stellar outflows has been detected in several cases. We present a *Chandra* observation of HH 168 and show that the soft X-ray emission from a plasma of 0.55 keV within HH 168 is diffuse. The X-ray emission is observed on two different scales: Three individual, yet extended, regions are embedded within a complex of low X-ray surface brightness. Compared to the bow shock the emission is displaced against the outflow direction. We show that there is no significant contribution from young stellar objects (YSOs) and discuss several shock scenarios that can produce the observed signatures. We establish that the X-ray emission of HH 168 is excited by internal shocks in contrast to simple models, which expect the bow shock to be the most X-ray luminous.

Key words. stars: winds, outflows – X-rays: ISM – Herbig-Haro objects – ISM: jets and outflows – ISM: individual objects: HH 168

1. Introduction

Star formation is intimately linked to accretion and outflow phenomena. Early in the formation process, the collapsing proto-star is deeply embedded and therefore invisible, yet, powerful outflows emerge from these systems. At a later stage, the accretion proceeds from a disk. For low-mass stars, the magnetically-funneled infall model explains many observed phenomena successfully, but, even in their case, the jet and wind driving mechanism remains elusive. Current theories expect mass loss to be driven by magneto-centrifugal disk winds, possibly with a stellar contribution. The physical mechanism, which accelerates and collimates the outflow also remains elusive. Jets have been observed at all stages of star formation over a wide mass range in different wavelength regions. HH 2 (Pravdo et al. 2001) and HH 154 (Favata et al. 2002; Bally et al. 2003; Favata et al. 2006) were the first massive, large-scale outflows discovered in X-rays. The latter object has already been observed twice, so that the proper motion of its X-ray emitting regions could be tracked. The proper motion of 500 km s^{-1} can explain the observed temperatures in terms of simple shock models of a thin gas ramming into the ambient medium. Examples of further evolved objects are the low-mass star DG Tau (Güdel et al. 2008b; Schneider & Schmitt 2008; Günther et al. 2009), where the X-ray emission from the jet is confined to the inner region of a few hundred AU and the intermediate mass Herbig Ae/Be star HD 163296 (Swartz et al. 2005; Günther & Schmitt 2009). Because of the low surface brightness of these jets and a lack of nearby young intermediate and high-mass stars, X-rays from their outflows have only been detected in very few cases.

Most models of high-energy emission in outflowing material adopt some type of shock. The interface between the outflowing material and the ambient medium seems to be a plausible heating source but evidence of additional X-rays produced close to the star is increasing. Thus, a more complex scenario might be required to explain the observed phenomena. Internal working surfaces within the outflow might be responsible for the heating, but they require rapidly moving components within the flow so that the velocity difference still provides enough energy to produce X-rays.

In the case of DG Tau, such a high velocity component has not been detected in UV, optical or IR observations. However, when compared to the outflow's total mass-loss this speculative high velocity component would constitute only a very small fraction of the total mass-loss and energy and, therefore, might have escaped detection (Schneider & Schmitt 2008; Günther et al. 2009).

This paper deals with the Cep A West region, where the outflow HH 168 is located. The central region of the complex, which presumably contains the jet driving source, will be analysed in a forthcoming article (Schneider et al. 2009). In the next section, we will provide a brief overview of the Cep A region and in the subsequent two sections the observation and results are presented. We then discuss the properties of the emitting plasma before we investigate possible scenarios explaining the observed X-ray emission.

2. The Cepheus A high-mass star-forming region

Cepheus A is the second nearest high-mass star-forming region at a distance of ~730 pc (Johnson 1957; Crawford & Barnes 1970, see Fig. 1 for an overview). Three Herbig-Haro objects (HH 168, HH 169, and HH 174) are located around the center of Cep A, where several distinct radio sources have been found (named HW 1-9; Hughes & Wouterloot 1984, HW 8 and HW 9 were detected by subsequent observations). Because of the strong absorption towards the center of Cep A ($A_V > 75$ mag) radio observations are the most suitable for imaging this region. In the IR wavelength range (e.g. 12.5 μm, Cunningham et al. 2009), none of the radio sources has been clearly detected and the region appears dark in Fig. 1.

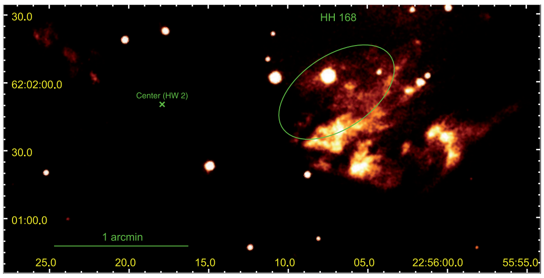

Fig. 1. SDSS[1] DR7 (Abazajian et al. 2009) *i*-band (7481 Å) image of the Cep A region. The ellipse indicates the soft X-ray emission. The diffuse object south of the ellipse is a reflection nebula probably excited by a source close to HW 2 or by HW 2 itself (Hartigan et al. 1986).

For the HH 169 and HH 174 outflows, HW 2 is currently the most promising candidate for the driving source, while it is unclear which source drives the HH 168 outflow, the possibilities being HW 2 and HW 3c, as well as an isolated region of star formation located at the eastern end of HH 168 (e.g., Cunningham et al. 2009).

The Cep A region also contains multiple molecular outflows. The extent of the large-scale outflows is on the arcmin scale with typical velocities on the order of a few 10 km s^{-1}. The multicomponent appearance of the outflow geometry can be interpreted in terms of dense condensations redirecting the outflow (Codella et al. 2003; Hiriart et al. 2004, and references therein), but multiple outflows or the evolution of a single outflow are also possible. The position angle of the northeast-southwest molecular outflow is consistent with the elongation of HW 2 at radio wavelengths. Observations of the gas dynamics, in particular of the H_2 gas (Hiriart et al. 2004), show a clear velocity gradient within the western H_2 structure (blueshifted at the eastern end and at approximately zero velocity at the western end).

The prominent HH object 168 is located west of the central sources of Cep A. Its kinematic lifetime is on the order of several 1000 years. The Hα, [S II], and [O III] images observed by the Hubble Space Telescope (HST, Hartigan et al. 2000) show that in the region of HH 168 no single type of shock can be responsible for the observed emission. In some of the bright regions, the location of H_2 emission downstream of the Hα emission is indicative of a shock-type that heats the material in front of the shock slowly without dissociating the H_2 molecules.

Radio emission has also been observed from a few regions within the HH object (Hughes & Moriarty-Schieven 1990). The radio brightest one is designated HW-object (without any number) by Hartigan & Lada (1985) and is located at the eastern end of HH 168. Four (or even five) small emitting regions have been resolved within this object (Rodríguez et al. 2005), all of them being time-variable on timescales of years. Furthermore, they have large proper motions (arguing against a stellar origin) increasing from east to west from 120 km s^{-1} to 280 km s^{-1}. The motion of these objects is directed westward which is approximately consistent with the direction of HH 168 itself.

Rodríguez et al. (2005) proposed that the luminosity changes of the individual sources might be caused by holes in a stream flowing around condensations and exciting the radio emission. These authors estimated an outflow speed of about 900 km s^{-1}, which still accelerates the radio-emitting objects. The spectral indices of these radio emitting objects within the HW object differ, pointing to different production mechanisms of the radio emission although simultaneous observations, as needed for time-variable sources, have not been carried out. One object seems to bare an ultra-compact, optically thick core, while another is consistent with shocked gas emission (Garay et al. 1996).

In this region, Hartigan et al. (2000) observed nine, approximately point-like, Hα emission components, which they related to young T Tauri stars, but Cunningham et al. (2009) found no point-like sources in their infrared images in this region, even though their sensitivity should be sufficient.

Using Hα images of HH 168, Lenzen (1988) measured the proper motions of individual knots ranging from 100 to 210 km s^{-1} (the HW-object in total has a velocity of 110 km s^{-1}). Raines et al. (2000) measured the HW object in [Fe II] 1.644 μm and found an object moving with a space-velocity of ~850 km s^{-1}, while the bulk of the [Fe II] emitting material moves only with 400 km s^{-1}. The Hα lines of the HW object, as well as the nearby knot E, extend from zero to −400 km s^{-1} (Hartigan et al. 1986).

Cunningham et al. (2009) proposed that the bright H_2 emission within HH 168 is caused by high-velocity material encountering already decelerated material, thus forming shocks (shock speeds possibly reaching 400 km s^{-1}). These authors further propose that the HW object is produced by two colliding winds, one producing the HH 168 object that is driven by a source close to HW 3c and the outflow of HW 2 that drives the eastern HH object.

In summary, there is no consensus about the nature of the observed objects in the literature. However, the large proper motion of some of those objects is sufficient for the production of X-rays by shocks.

The region of Cep A was observed with *XMM-Newton* by Pravdo & Tsuboi (2005) for 44 ks. They detected very soft diffuse X-ray emission at the position of HH 168 and constrained the total luminosity and temperature of the region. Due to the limited spatial resolution, they could not identify the precise location of the soft X-ray source(s). The diffuse X-ray emission HH 168 shows a temperature of $T = 5.8^{+3.5}_{-2.3} \times 10^6$ K absorbed by a column density of $n_H = 4 \pm 4 \times 10^{21}$ cm^{-2}.

3. Observation and data processing

The Cep A region was observed on 8 April 2008 for 80 ks with ACIS-I (ObsID: 8898). We used CIAO 4.1.2 to analyse the data, following closely the science threads published at the CIAO website[2]. We used the archival data without reprocessing the *evt*2 file; therefore, the standard parameters are applied to the data. The analysis is restricted to events with energies between 0.3 keV and 10.0 keV, i.e., the energy range with a reliable calibration.

For both, detection and spectral analysis, an estimate of the background is needed. The background for the X-ray emission related to HH 168 was estimated from two regions. The smaller one is a nearby ellipse of approximately the size of HH 168 ($a = 30''$, $b = 16''$) containing 557 events in the full energy range (30 photons in the 0.3–1.5 keV range, i.e., the range in which shock-induced X-rays are expected). The second region is more than seven times larger (60″ radius) and is located further off-axis to ensure that it is source-free, e.g., that no source is visible in the 2MASS images nor identified by any of the CIAO source-detection algorithms in that region); it contains

[1] http://www.sdss.org/

[2] http://cxc.harvard.edu/ciao/

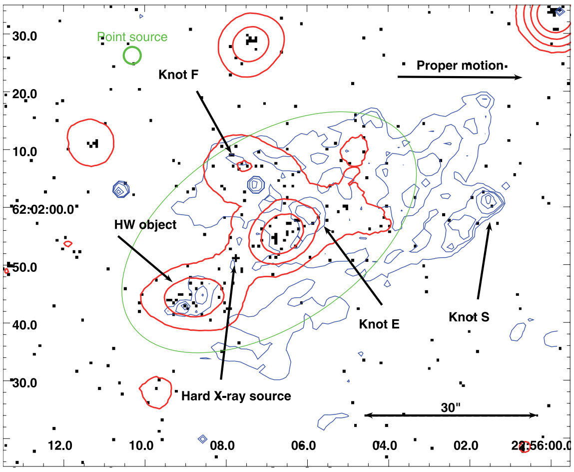

Fig. 2. The region around HH 168 in soft X-rays (energies between 0.3 keV and 1.5 keV). Single pixels show individual photon positions. The blue contour is the Hα emission from Hartigan et al. (2000), while the red contour shows the smoothed X-ray photon distribution which are multiples of four times the background rate. The proper motion of the HH object is directed toward the right.

261 photons in the 0.3–1.5 keV range. Both background estimates agree approximately in terms of their predicted count levels (5.7×10^{-3} cts/pixel for the large area, and 5.0×10^{-3} cts/pixel for the smaller one, in the 0.3–1.5 keV energy range). We use the average of both values to determine the estimated background. Their full range median energies coincide to within about 100 eV.

The spectral analysis was carried using XSPEC (Arnaud 1996) assuming an absorbed optically thin plasma emission model (APEC, Smith et al. 2001). We adopt 1σ errors throughout the paper.

4. Results

Figure 2 shows an overview of the HH 168 region in soft X-rays. In soft X-rays, `vtpdetect` of the *Chandra* CIAO 4 tools finds an extended source in the HH 168 region. We indicate the excess region by the green ellipse in Fig. 2, which approximately coincides with the lowest X-ray contour (red). In this region, there is an excess of 101 ± 13 photons over the expected background in the 0.3–1.5 keV range while no diffuse excess is present in hard X-rays (1.5–9.0 keV; see Table 1 for the number of detected counts and estimated background counts).

Within HH 168, approximately between the HW object and knot E, a hard, point-like X-ray source containing 10 photons is present (J(2000) = 22:56:07.8 +62:01:51.3). It can be characterised by a median energy of 2.6 keV and no X-ray photons below 1.5 keV. The estimated unabsorbed X-ray luminosity is 7.5×10^{29} erg/s assuming a plasma temperature of 1.4 keV and an absorbing column density of 3.5×10^{22} cm^{-2}. This model reproduces the median energy.

4.1. Morphology

The soft X-ray contour (starting at four times the background level) overlaps with the Hα contour, but lags behind the head of the Hα emission (e.g., knot S) by 20″. At the interface between the outflow and the ambient medium, only a very weak X-ray excess close to knot S is found. Within a circle of 5″ radius around knot S (the only Hα knot showing bow-shock characteristics), we detect 5 photons, where 2 are expected from the background.

No soft point-like source can be detected at a level above 1.1σ. At this detector position, one would expect that more than 95% of the photons from a point-source (with the observed soft spectrum) are located within a circle of radius of 1.5″ (in Figs. 2 and 3, we show these circles for comparison). The area with the highest photon density in that region contains six photons within the 1.5″ radius circle and lies within the highest contour in the middle panel of Fig. 3.

Three individual components with an enhanced diffuse emission are clearly visible within the large region, and are also indicated in Fig. 2 and shown in greater detail in Fig. 3 (Table 1 summarizes their properties). The location of the eastern one coincides with the HW-object found by Hughes & Wouterloot (1984) at cm-wavelengths, and the central one is located close to but offset to the east, the bright Hα knot E in the nomenclature of Hartigan et al. (2000), which shows also weak radio emission. The third component is located close to knot F, which also emits at radio wavelengths. There are further radio emission components at the western end of HH 168 showing equally strong radio emission but outside the X-ray contour of Fig. 2. On the other hand, all three regions with enhanced X-ray emission have radio components in their vicinity.

The low count density renders an estimate of the true size of the emission regions impossible. For the diffuse emission close to the HW-object and knot E, circular regions coinciding approximately with the second contour in Fig. 3 (4×10^{-2} cts/pixel, eight times the background level) were used to extract the photons of these two components. For knot F, we show the circle in Fig. 3.

Table 1. Diffuse X-ray emission in HH 168 (0.3–1.5 keV).

Component	Photons	Est. background photons	Median energy	Area arcsec^2
Ellipse	133	32.0	0.95 keV	1463
HW object	16	1.3	1.1 keV	61
Knot E	30	2.4	0.85 keV	108
Knot F	11	1.0	1.1 kev	44

The knot E region has an excess of 28 ± 6 photons (area 108 arcsec^2) and the region around the HW object has an excess of 15 ± 4 photons (area 61 arcsec^2). Close to knot F, the X-ray emission has an excess of 10 photons (area 44 arcsec^2). All of these regions are *not* compatible with single point-sources as we would expect only 2–3 photons outside a 1.5″ radius for the numbers at hand, in contrast to the observational result. However, it is possible that e.g., six of the photons in the knot E region are indicative of an active pre-main-sequence star. The emission close to knot F does *not* coincide with the position of the foreground star from which no X-ray emission is observed.

There is diffuse emission beyond the three individual emission components. Excluding the knots from the region defined by the ellipse, a clear excess of 48 ± 10 photons is found. We therefore regard the contours in Fig. 2 as real, although we do not claim that the shape of the contours represent the precise geometry of the emitting volume.

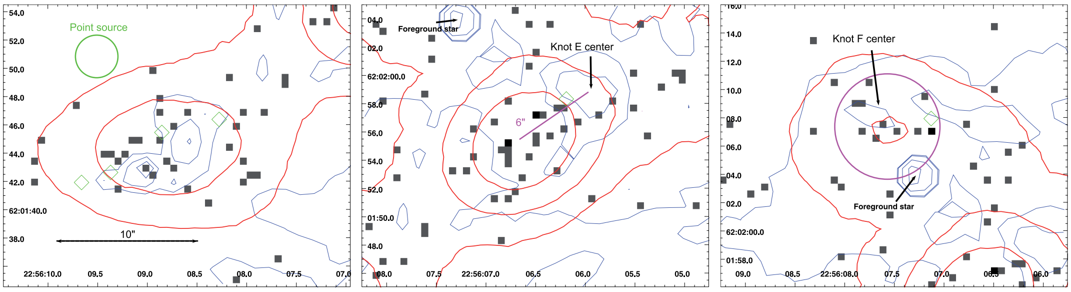

Fig. 3. Zoom into selected regions. In the *left panel*, the HW-object, in the *middle panel*, the region around knot E, and in the *right panel* the knot F region are shown. Squares denote individual photons. The red contours are the X-ray contours from Fig. 2. Hα emission is shown as blue contours and green diamonds designate radio sources from Rodríguez et al. (2005); Hughes & Moriarty-Schieven (1990).

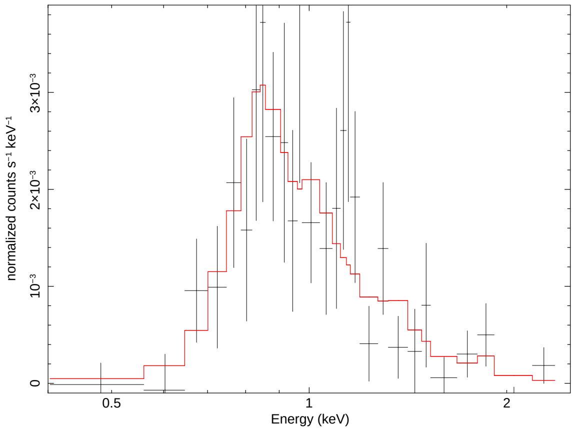

Fig. 4. Spectrum of the photons within HH 168. The fitted model is shown in red.

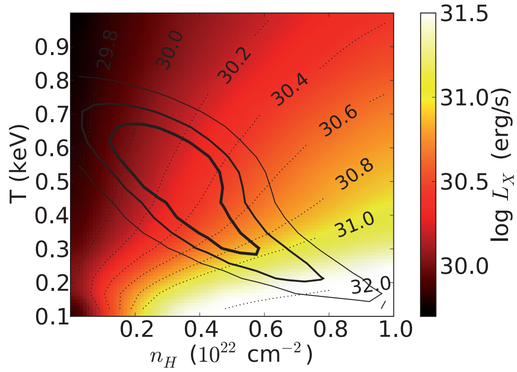

Fig. 5. Contours showing different confidence levels of the plasma parameters. The contours designate the 1σ, 90%, and 99% confidence levels. The X-ray luminosity is color coded and indicated by the dotted lines.

4.2. Spectral properties and energetics

Considering the energies of the photons within these three regions, we find slight differences between the median energies of the photons within the HW-object (1.1 keV) and the knot E photons (0.9 keV). A KS-test infers a probability of only 15% that both samples are drawn from the same distribution. On the other hand it is probable (60%) that the photons around knot E and those of the large-scale diffuse emission are drawn from the same distribution.

Ignoring for a moment this difference, we show in Fig. 4 the spectrum of the photons within the ellipse. The spectrum can be described well by an absorbed, thermal, optically thin plasma with $kT = 0.55 \pm 0.1$ keV and an absorbing column density of $n_{\rm H} = 3 \pm 1 \times 10^{21}$ cm^{-2}. These values are consistent with the *XMM-Newton* data of Pravdo & Tsuboi (2005). Using the conversion between $n_{\rm H}$ and $A_{\rm V}$ from Vuong et al. (2003), we find that $A_{\rm V} \sim 2$.

Using the best-fit values, the total unabsorbed energy-loss of the diffuse emission component in X-rays is about 1.7×10^{30} erg s^{-1}. Figure 5 shows the contours of several significance levels in the (kT, $n_{\rm H}$)-plane; this plot illustrates the dependence of the luminosity on the adapted spectral parameters. The energy-loss within the smaller components scales with their photon numbers ($L_{\rm X} \approx N/N_{\rm total} \cdot L_{\rm X}^{\rm total} = 5 \times 10^{29}$, 3×10^{29} and 2×10^{29} erg s^{-1} for knot E, the HW region, and knot F, respectively).

The difference in the median energy of the photons can either be caused by a different absorbing column density or by an intrinsically different temperature of the plasmas. In either case, one needs to approximately double either T or $n_{\rm H}$ to increase the median energy by 0.2 keV.

An estimate of the electron density $n_{\rm e}$ of the X-ray emitting plasma can be given by the volume emission measure (EM, provided by the fit) needed to achieve the observed flux by

$$n_{\rm e} = \sqrt{\frac{EM}{0.85 \cdot f\, V}}, \tag{1}$$

where V is the volume of the emitting region, f the filling factor, and the factor 0.85 reflects the solar ratio of electrons to H-atoms in an ionized plasma). The EM for the large region has a value of 6.4×10^{52} cm^{-3}, while it is a few 1×10^{52} cm^{-3} for the individual regions. Assuming spherical/ellipsoidal volumes, we find 4.2×10^{52} cm^3 for the entire area, 1.1×10^{51} cm^3 for the knot E region, and 4.6×10^{50} cm^3 for the HW region leading to densities of $n_{\rm e} = 1.3$ cm^{-3} for the large-scale emission and about 10 cm^{-3} for the smaller regions.

None of those objects exhibit significant variability in their light curves. However, the low number of counts is not sufficient to exclude minor variability (factor ~2) within 10 ks.

5. Is the emission really diffuse?

The appearance of a diffuse emission component can in principle be mimicked by a superposition of a large number of discrete sources as Cep A is a young star-forming region. We therefore assume in this section that a great number of YSOs produce the soft X-rays, and highlight the problems of this scenario. We concentrate on the 0.3–1.5 keV energy range to which the hard X-ray source does not contribute.

1. For the entire region of HH 168, not even one pixel contains three photons. Assuming that the individual sources contribute only 5 photons each, then 20 of these sources are needed. Lowering the significance of the source-detection algorithm as far as possible, only 26 sources are detected with a mean count number of about two. Thus, a higher number of discrete sources (>50) is required to explain the soft X-ray emission with point sources.
2. The relatively small absorbing column density should also ensure that pre-main sequence stars are detectable in the IR and possibly also as Hα sources. Taking the saturation limit of $L_X/L_{bol} \approx 10^{-3}$, we find that a single highly active mid-M dwarf would produce a single X-ray photon at a distance of 730 pc. Thus, about 100 M-dwarfs are needed within the HH object to account for the total luminosity. A mid M-dwarf has an apparent V-magnitude of about 20 assuming that $A_V = 2$. Thus, even in the unlikely case that only M-dwarfs and later objects are present in HH 168, at least some should have been detected with the available observations. Furthermore, the X-ray emission does not seem to be concentrated in the shallow strip as the peaks in Hα. For the enhanced emission close to the knot E, we note that the X-ray emission is offset from the bright Hα emission and the potential position of the YSOs.
3. No diffuse hard X-ray emission ($E > 1.5$ keV), expected to be present in low-mass pre-main-sequence stars, is observed. The median plasma temperature of the sources in the Orion nebula cloud (COUP: Preibisch et al. 2005; Getman et al. 2005) is more than a factor of three higher than the best-fit temperature of the diffuse HH 168 emission. Taking the median count number of the COUP sources, the expected count number of this "normal" stellar source would be about 10 photons for the absorption and distance of Cep A. The highest photon density within the HH 168 area contains six photons within the 95% region of a point source.
4. The probability of finding a YSO in the HH 168 region can be estimated using the stellar surface density of the Cep A region derived by Gutermuth et al. (2009) from mid-infrared imaging. Assuming a uniform distribution of their sources, we derive a probability of about 0.2% of finding one source within a 1 arcsec^2 region. The stellar surface density also matches approximately that of the Trapezium region in Orion, which was studied during the COUP project with a 25 times higher X-ray sensitivity than the observation of Cep A. From the surface density of the 1616 COUP X-ray sources, we estimate a probability of about 0.5% of finding one X-ray source within 1 arcsec^2. Both values correspond to less than one expected source within the three individual components, while two (five) sources are expected within the large source ellipse. These numbers are too low to account for the luminosity of the object.

We regard a stellar population of only M-dwarfs and later objects without any hard X-ray emission, as an unlikely source of the observed diffuse X-ray emission. The shape of the emitting region (located within the Hα contour) and the apparent softening of the outflow from east to west, are not explained. However, a limited number of weak discrete sources cannot be excluded. We therefore conclude, that the vast majority of the emission is indeed diffuse.

6. Are the X-rays produced in shocks?

A solution for the heating of the observed hot plasma is shock heating. In this section, the properties of the observed X-ray emission are related to those expected from shocks.

6.1. X-ray emission from shocks

The observed X-ray emission is produced by plasma with temperatures of around or above 10^6 K. Because shocks are the ultimate origin of this hot plasma (ignoring possible contributions by coronal emission of unresolved stars in this region) we recall some relations between properties observable at other wavelengths and X-rays.

From the strong shock jump condition, the temperature T of the plasma is

$$T \approx 1.5 \times 10^5\ \mathrm{K} \left(\frac{\upsilon_{bs}}{100\ \mathrm{km\,s^{-1}}}\right)^2, \tag{2}$$

where υ_{bs} is the velocity of the pre-shock material in the shock rest-frame and the cooling distance d_{cool} can be found by the interpolation formula of Heathcote et al. (1998)

$$d_{cool} \approx 2.2 \times 10^{16}\ \mathrm{cm^{-2}} n_0^{-1} \left(\frac{\upsilon_{bs}}{100\ \mathrm{km\,s^{-1}}}\right)^{4.5}, \tag{3}$$

which depends on the pre-shock particle number density n_0 and has a ~20% accuracy within the 150–400 km s^{-1} range (Raga et al. 2002). Furthermore, the mass flux rates for quasi-stationary shock configurations can be calculated from the thermal energy kT and the EM according to Günther et al. (2009) to be

$$\dot{M}_{shock} \approx 2.7 \times 10^{-11} \frac{M_\odot}{\mathrm{yr}} \left(\frac{EM}{10^{52}\ \mathrm{cm^{-3}}}\right) \left(\frac{0.33\ \mathrm{keV}}{kT}\right)^{1.75}. \tag{4}$$

6.2. Are the spectral properties consistent with shocks?

The range of possible plasma temperatures (see Fig. 5) reaches from 0.1 keV to 0.6 keV. The corresponding shock speeds are 280 km s^{-1} and 680 km s^{-1}, respectively; speeds in that range have been deduced in this region. The proper motion of individual knots is ~300 km s^{-1} and possibly even higher (Raines et al. 2000), the emission line width might be as great as 400 km s^{-1} (Hartigan et al. 2000) and Rodríguez et al. (2005) speculate about inhomogeneities in the outflow moving with 900 km s^{-1}. A superposition of flows with different shock speeds might also result in the observed spectrum.

The observed low absorption is compatible with the detection of NIR and Hα emission in that region. Differences in the absorbing column density have not been investigated with the available observations, although, a uniform absorbing column density is unlikely.

The derived densities (assuming a filling factor f of unity) are about a factor 1000 lower than those estimated from optical emission lines (Hartigan et al. 2000), but the thermal pressure P of the hot plasma ($P = nkT$, k Boltzmann's constant) and that of the optically observed material ($T \sim 10^4$ K and $n \sim 10^4$ cm^{-3})

differ by only a factor of ten. To avoid the low pressure of the X-ray plasma, a filling factor f of less than a tenth is mandatory.

Alternatively, the hot ions might represent a co-spatial component of a denser and cooler gas, which is not yet thermalised. In collision-dominated plasmas, a few mean free path lengths are sufficient to arrive at a Maxwellian energy distribution. The mean free path l for collisions with neutrals of number density n is

$$l = (n\pi a_0^2)^{-1} \approx 10^{16} n^{-1}\ \mathrm{cm}^{-2}, \tag{5}$$

where a_0 is the Bohr radius of the hydrogen atom (Lang 1999). For typical densities of $n = 10^3$ cm^{-3}, a hot ion population would thermalise within a few AU. Thus, we cannot expect to find two distinct populations in a given volume in the abscence of heating and we reject this scenario. Therefore, either the X-ray emission is produced in only a thin surface layer of gas filled bubbles, possibly at the interface between the driving flow and the ambient medium, or in smaller individual knots such as the Hα or radio features within HH 168 (Hartigan et al. 2000; Rodríguez et al. 2005).

With an estimate of the density of the X-ray emitting plasma, we can derive the cooling time of the material by

$$\tau = \frac{3kT}{n_\mathrm{e}\Lambda(T)} = 1.6\times10^{13} n_\mathrm{e}^{-1}\ \mathrm{s\,cm^3} = 5\times10^5 \left(\frac{n_\mathrm{e}}{\mathrm{cm^3}}\right)^{-1}\ \mathrm{yr}, \tag{6}$$

where we assumed for the cooling function $\Lambda(T) = 8\times10^{-23}$ erg cm^3 s^{-1} and the best-fit model value $T = 0.55$ keV. Thus, only for densities of $n_\mathrm{e} \sim 10^3$ cm^{-3} are the cooling time and the kinematic lifetime of the outflow of the same order, since typical timescales for the age of the outflow are in the range of several 1000 years.

Only for densities above $n_\mathrm{e} \sim 10^5$ cm^{-3} is the cooling time sufficiently short for the plasma to remain within around 730 AU (an arcsec) of its heating location assuming a proper motion of $0.1''$ yr^{-1}. Otherwise, the timescale for the cooling is so long that the position of the plasma is not necessarily close to the location where the heating occurred.

If we assume that the HW object and the knots E and F are currently heated by ongoing shocks, so that we observe the post-shock cooling zone, we can calculate the mass loss according to Eq. (4), as $\approx 10^{-10}$ $M_\odot$ yr^{-1}.

The total X-ray luminosity of HH 168 is an order of magnitude larger than the X-ray jet of DG Tau (which is a pre-main-sequence star of less than one solar mass) and in-between those of HH 2 and HH 80/81. In those cases, the mechanical energy of the outflow is by far sufficient to power the X-ray emission, which is probably also true for HH 168; although the kinetic energy of the outflow is not known, that of the molecular outflow alone exceeds the required energy by a few orders of magnitude.

Thus, we conclude that all spectral properties are consistent with shock heating and the properties derived from other wavelengths.

6.3. Comparison with HH 2 and HH 80/81

Soft X-ray emission within similar HH objects has also been detected from HH 2 (Pravdo et al. 2001), HH 80/81 (Pravdo et al. 2004), and HH 210 (Grosso et al. 2006). Their temperatures ($kT \sim 0.1$ kV) and association with an HH object are very similar to HH 168. The density $n_\mathrm{e} \approx 50$ cm^{-3} of the X-ray emitting material is for HH 2 and HH 80 higher than the values of HH 168. In these cases, the brightest X-ray emission components are correlated with bright Hα emission knots exhibiting bow-shock-like structures.

Therefore, the heating most probably occurs in these objects because of an interaction of the outflow with another medium. This might be the ambient medium or a low-density bubble produced by a protostellar object as suspected by Pravdo et al. (2004) because of the presence of a hard X-ray source between the soft X-ray emission components. For HH 168, the X-ray emission is not located at the head of the outflow where bow-shock structures are observed (Hartigan et al. 2000), but a hard X-ray source within in the soft diffuse X-ray emission is also present. The large-scale diffuse emission found in the case of HH 168 is not present in any of the other sources, which are extended on the scale of a few arcsec.

For HH 2 and HH 80/81, the X-ray emission correlates approximately with radio emission knots in the sense that a radio component is located close to the X-ray emission, while there are also radio knots without X-ray emission. Knot E in HH 168 might be an exception of this rule.

7. Location of shocks

Where should we expect the shocks heating the plasma to the observed X-ray emitting temperatures to be located? Because of the long cooling time of the X-ray emitting material, the observed X-ray emission might have been heated some time ago.

7.1. Shocks at the head of the outflow

The natural position of strong shocks is the head of the outflow since there the velocity difference is largest, but the bulk of the X-ray emission is located in the eastern part of the Hα emission (see the X-ray contours in Fig. 2). If HH 168 is bounded by a shock front sufficiently strong to reach X-ray emitting temperatures, only a small offset is expected, because some time is needed to reach the ionisation equilibrium. For a density of 10^3 cm^{-3}, we checked the timescale with a shock code that explicitly calculates the ionisation timescale (Günther et al. 2007) and find, that the shock would produce O VII, whose line emission dominates plasmas of the observed temperature, within 30 AU. The calculation scales inversely with the electron density so that even for a lower electron density of a few 10 cm^{-3}, the ionisation equilibrium is reached after less than thousand AU (less than one arcsec). This value is much smaller than the observed offset between the X-ray emitting material and the Hα contour.

The brightest Hα knot (knot S, see Hartigan et al. 2000) shows the characteristic properties of a bow shock with the ambient medium, but has, at most, only weak excess X-ray emission (three photons above the estimated background). A stronger absorption at this part of the outflow than at the eastern end of HH 168 might reduce the observed flux. Doubling the absorption would decrease the count rate by a factor of four rendering the detection of soft X-rays virtually impossible, but a lower shock velocity or a smaller radius of the obstacle would also result in a smaller amount of material being heated to X-ray emitting temperatures and thus a reduction in the observed flux.

The shocks might have been more energetic in the past, so that in case of a low plasma density ($n_\mathrm{e} \lesssim 10^3$ cm^{-3}) the observed material was heated much earlier in the outflow history and the luminosity at the current shock front (in particular knot S) is below the detection limit. The shape of the X-ray emission might then represent the "shock history" of the outflow.

7.2. Shocks within the HH-object

Since most of the X-ray emission is observed within the outflow, another explanation for the observed features is presented.

There has been some speculation about a high velocity component (~900 km s^{-1}) within HH 168 (Raines et al. 2000; Rodríguez et al. 2005), which is sufficiently fast to produce X-ray emission within HH 168 when encountering denser and slower material, such as a thin bubble expanding from the hard X-ray source between the HW object and knot E similar to the scenario proposed by Pravdo et al. (2004) for HH 80. The individual X-ray components are not aligned in the east-west direction of the large-scale outflow, but a single precessing jet (as proposed for the eastern HH objects, Cunningham et al. 2009) with an opening angle of only 20 degrees can reach all X-ray and radio components (assuming a driving source at Cep A East). A deflection of the outflow at high density clumps or different outflows might also explain the morphology. Therefore, the same high velocity flow heating the HW-object might also heat the material close to knot E and knot F.

The highest X-ray luminosity is observed close to knot E and might be a remnant of strong shocks in that region. The relatively low density of the X-ray emitting material and its lower median energy compared to the HW object, support a scenario in which the heating happened earlier and the currently emitting material is not at the position of its heating.

The strongest radio emission is detected at the HW-object, the region closest to the driving source of the HH 168 outflow, (or harbouring the driving source itself, Garay et al. 1996). Goetz et al. (1998) and Cunningham et al. (2009) speculate that the outflow might be deflected somewhere around the HW-object, or that two outflows (those of HW 2 and HW 3c) collide at this position. It is possible that the heating of the plasma happens somewhere near or within the HW-object and the X-ray emission westwards is from cooling plasma. In this scenario, the difference between the median energy of the HW-object and the knot E photons reflects the cooling of the material, and a density of a few 100 cm^{-3} is necessary to explain the softening of the photons by radiative losses. The lack of significant X-ray emission at the western end of the HH-object would be naturally explained in this scenario. The weak X-ray emission close to knot S is then, if real, caused by small shocks of the outflowing material with the ambient medium.

However, the correlation of the optically observed material (in particular Hα emission), the radio emission and the brightest X-ray emission points to a similar heating mechanism for all of these features. The electron density estimated from the radio observations is about a hundred times higher than that estimated from X-rays but another factor of ten lower than calculated for the material radiating in forbidden emission lines. This would imply a pressure balance, if less than a tenth of the observed volume is filled with a hot plasma. Thus, the observed X-ray emission probably traces the (former) location of strong shocks that in the mean time decelerated explaining the offset between Hα and X-ray emission seen in knot E, and on a smaller scale within the HW object. The diffuse X-ray emission, which is also present between the individual knots, is probably very thin plasma heated earlier in the outflow history and cooling slowly.

7.3. A reverse shock

Another possible way of explaining the offset between the Hα emission and the X-ray emission are reverse shocks. Some time ago, two shock fronts originated in the head of the outflow, one moving in the primary direction of the flow, and the other traveling backwards relative to the bulk material. At any given point in time, the reverse shock appears similar to internal working surfaces, which are caused by intrinsic inhomogeneities in the jet, but its post-shock cooling zone can be found towards the head of the outflow. In this case, the X-rays of the HW object or knot E are the sign of an extended cooling zone. At some distance to the shock, the matter cools to Hα emitting temperatures. This scenario is attractive, because it can explain the observed offset between X-ray emission and Hα contours, although, we would expect at least some optical emission close to the actual shock front.

7.4. An expanding bubble filled with hot plasma

For a cooling time on the order of the kinematic lifetime of the outflow and a launching point somewhere in the region of the radio sources in Cep A East, it is possible that the X-ray emitting material might be heated closer towards the centre where the absorption is higher and thus the heating source may remain undetected in X-rays by current observations.

On larger scales ($l \gtrsim 1$ parsec), bubbles filled with a very thin ($n_e < 1$ cm^{-3}) and hot ($kT \sim 1$ keV) X-ray emitting gas have been found (Townsley et al. 2003; Güdel et al. 2008a). The minimum electron densities in the case of HH 168 are close to these values. However, the proposed B stars in Cep A East have a lower mass-loss and slower wind speeds than the O type stars usually needed to fill the large bubbles. Furthermore, in all other cases the X-ray emitting gas seems to be channeled by surrounding H_2, while in this case, the H_2 emission shows signatures of strong interaction with the ambient medium (bow shocks, Cunningham et al. 2009) co-spatial with the X-ray emission. However, HH 168 might be a kind of a transition object, where a low density plasma, heated either within the outflow or close to the driving sources, survives in a bubble blown out by earlier outflow episodes.

8. Summary

The *Chandra* observation of HH 168 confirms the presence of diffuse soft X-ray emission within HH 168 as seen by XMM-*Newton*. The spectral properties of both observations agree well. The higher angular resolution of the *Chandra* observation clearly shows the diffuse character of the emission and discards YSOs as the origin of the X-rays. Furthermore, the substructure within the X-ray emission shows a good correlation with the optical and radio "knots". Although this correlation has been seen in other HH objects such as HH 2 and HH 80/81, the bulk of the X-ray emission in the case of HH 168 is not at the location of bow shocks. Instead, the X-rays are displaced towards the driving sources against the outflow direction by several thousands of AU. We regard this as evidence of internal shocks probably powered by a high velocity component within the large-scale outflow. The X-ray emitting plasma correlates with Hα emission but is displaced from the Hα knots. This points, in combination with the low density of the X-ray emitting plasma, to cooling plasma heated by the same outflow component leading to the currently observed Hα emission. The detection of diffuse emission apparently unrelated to the knots is indicative of a thin hot plasma heated by earlier shock events.

Note added in proof After acceptance of this paper an article dealing with the same X-ray data appeared in Pravdo et al. (2009). However, these authors concentrate on the central region of Cep A. Their results concerning the spectral properties and the location of the X-ray emission of HH 168 are compatible with ours.

Acknowledgements. We thank the referee, Dr. M. Güdel, for his valuable comments which improved the paper. This work has made use of data obtained from the *Chandra* data archive and the SDSS (http://www.sdss.org/). P.C.S. acknowledges support from the DLR under grant 50OR0703. H.M.G. acknowledges support from the DLR under grant 50OR0105.

References

Abazajian, K. N., Adelman-McCarthy, J. K., Agüeros, M. A., et al. 2009, ApJS, 182, 543
Arnaud, K. A. 1996, in Astronomical Data Analysis Software and Systems V, ed. G. H. Jacoby, & J. Barnes, ASP Conf. Ser., 101, 17
Bally, J., Feigelson, E., & Reipurth, B. 2003, ApJ, 584, 843
Codella, C., Bachiller, R., Benedettini, M., & Caselli, P. 2003, MNRAS, 341, 707
Crawford, D. L., & Barnes, J. V. 1970, AJ, 75, 952
Cunningham, N. J., Moeckel, N., & Bally, J. 2009, ApJ, 692, 943
Favata, F., Fridlund, C. V. M., Micela, G., Sciortino, S., & Kaas, A. A. 2002, A&A, 386, 204
Favata, F., Bonito, R., Micela, G., et al. 2006, A&A, 450, L17
Garay, G., Ramirez, S., Rodriguez, L. F., Curiel, S., & Torrelles, J. M. 1996, ApJ, 459, 193
Getman, K. V., Flaccomio, E., Broos, P. S., et al. 2005, ApJS, 160, 319
Goetz, J. A., Pipher, J. L., Forrest, W. J., et al. 1998, ApJ, 504, 359
Grosso, N., Feigelson, E. D., Getman, K. V., et al. 2006, A&A, 448, L29
Güdel, M., Briggs, K. R., Montmerle, T., et al. 2008a, Science, 319, 309
Güdel, M., Skinner, S. L., Audard, M., Briggs, K. R., & Cabrit, S. 2008b, A&A, 478, 797
Günther, H. M., & Schmitt, J. H. M. M. 2009, A&A, 494, 1041
Günther, H. M., Schmitt, J. H. M. M., Robrade, J., & Liefke, C. 2007, A&A, 466, 1111
Günther, H. M., Matt, S. P., & Li, Z.-Y. 2009, A&A, 493, 579
Gutermuth, R. A., Megeath, S. T., Myers, P. C., et al. 2009, ApJS, 184, 18
Hartigan, P., & Lada, C. J. 1985, ApJS, 59, 383
Hartigan, P., Lada, C. J., Tapia, S., & Stocke, J. 1986, AJ, 92, 1155
Hartigan, P., Morse, J., & Bally, J. 2000, AJ, 120, 1436
Heathcote, S., Reipurth, B., & Raga, A. C. 1998, AJ, 116, 1940
Hiriart, D., Salas, L., & Cruz-González, I. 2004, AJ, 128, 2917
Hughes, V. A., & Moriarty-Schieven, G. 1990, ApJ, 360, 215
Hughes, V. A., & Wouterloot, J. G. A. 1984, ApJ, 276, 204
Johnson, H. L. 1957, ApJ, 126, 121
Lang, K. R. 1999, Astrophysical formulae, ed. K. R. Lang
Lenzen, R. 1988, A&A, 190, 269
Pravdo, S. H., & Tsuboi, Y. 2005, ApJ, 626, 272
Pravdo, S. H., Feigelson, E. D., Garmire, G., et al. 2001, Nature, 413, 708
Pravdo, S. H., Tsuboi, Y., & Maeda, Y. 2004, ApJ, 605, 259
Pravdo, S. H., Tsuboi, Y., Uzawa, A., & Ezoe, Y. 2009, ApJ, 704, 1495
Preibisch, T., Kim, Y.-C., Favata, F., et al. 2005, ApJS, 160, 401
Raga, A. C., Noriega-Crespo, A., & Velázquez, P. F. 2002, ApJ, 576, L149
Raines, S. N., Watson, D. M., Pipher, J. L., et al. 2000, ApJ, 528, L115
Rodríguez, L. F., Torrelles, J. M., Raga, A. C., et al. 2005, Rev. Mex. Astron. Astrofis., 41, 435
Schneider, P. C., & Schmitt, J. H. M. M. 2008, A&A, 488, L13
Schneider, P. C., Guenther, H. M., & Schmitt, J. H. M. M. 2009, A&A, 508, 321
Smith, R. K., Brickhouse, N. S., Liedahl, D. A., & Raymond, J. C. 2001, ApJ, 556, L91
Swartz, D. A., Drake, J. J., Elsner, R. F., et al. 2005, ApJ, 628, 811
Townsley, L. K., Feigelson, E. D., Montmerle, T., et al. 2003, ApJ, 593, 874
Vuong, M. H., Montmerle, T., Grosso, N., et al. 2003, A&A, 408, 581

7. The X-ray puzzle of the L1551 IRS 5 jet

P.C. Schneider, H. M. Günther, J. H. M. M. Schmitt
Astronomy & Astrophysics, submitted (2010)

Astronomy & Astrophysics manuscript no. HH154m
December 10, 2010

The X-ray puzzle of the L1551 IRS 5 jet

P. C. Schneider[1], H. M. Günther[2], and J. H. M. M. Schmitt[1]

[1] Hamburger Sternwarte, Gojenbergsweg 112, 21029 Hamburg, Germany e-mail: cschneider/jschmitt@hs.uni-hamburg.de
[2] Harvard-Smithsonian Center for Astrophysics, 60 Garden Street, Cambridge, MA, USA e-mail: hguenther@head.cfa.harvard.edu

Received .. / accepted ..

ABSTRACT

Protostars are actively accreting matter and they drive spectacular, dynamic outflows, which evolve on timescales of years. X-ray emission from these jets has been detected only in a few cases and little is known about its time evolution. We present a new *Chandra* observation of L1551 IRS 5's jet in the context of all available X-ray data of this object. Specifically, we perform a spatially resolved spectral analysis of the X-ray emission and find that (a) the total X-ray luminosity is constant over almost one decade, (b) the majority of the X-rays appear to be always located close to the driving source, (c) there is a clear trend in the photon energy as a function of the distance to the driving sources indicating that the plasma is cooler at larger distances and (d) the X-ray emission is located in a small volume which is unresolved perpendicular to the jet axis by *Chandra*.

A comparison of our X-ray data of the L1551 IRS 5 jet both with models as well as X-ray observations of other protostellar jets shows that a base/standing shock is a likely and plausible explanation for the apparent constancy of the observed X-ray emission. Internal shocks are also consistent with the observed morphology if the supply of jet material by the ejection of new blobs is sufficiently constant. We conclude that the study of the X-ray emission of protostellar jet sources allows us to diagnose the innermost regions close to the acceleration region of the outflows.

Key words. stars: winds, outflows - X-ray: ISM - Herbig-Haro objects - ISM: jet and outflows - ISM: individual objects: HH 154 - ISM: individual objects: L1551 IRS 5

1. Introduction

During the early stages of star formation the protostar is deeply embedded and therefore usually invisible at optical wavelengths; only infrared and radio emission, and potentially hard X-rays, penetrate the dense circumstellar environment. Yet, outflows, detectable at various energy bands, escape the protostellar envelope announcing the birth of a new star. At later stages of stellar evolution, when the accretion proceeds from a disk and the star becomes visible in the optical, outflow activity is still observed. However, the driving mechanism of these outflows remains elusive; neither the acceleration nor the collimation of the outflow are currently fully understood, magneto-centrifugally launched disk winds, with a possible stellar contribution are currently debated (e.g. Ferreira et al. 2006).

The most spectacular manifestations of these stellar outflows are the condensations/shocked-regions termed Herbig-Haro (HH) objects. The proper motion of these knots within the outflows is generally in the range of a few 100 km s^{-1}. Protostellar jets are intrinsically dynamic objects; their evolution is observable on timescales of a few years and models with variable ejection velocities can successfully explain some features of these jets (e.g. Raga et al. 2010). In these models, the overtaking of small slow blobs by faster more recently emitted blobs leads to shock fronts with shock velocities on the order of the amplitude of the velocity difference.

HH objects with X-ray emission are a recently discovered phenomenon. Ten such objects have so far been detected among the hundreds of known HH objects; shock velocities around 500 km s^{-1} are required to heat material to X-ray emitting temperatures in terms of simple shock models. HH 2 (Pravdo et al. 2001) and HH 154 (Favata et al. 2002; Bally et al. 2003) marked the starting point of the X-ray discoveries. These outflows are driven by deeply embedded protostars (or their accretion disks). However, X-rays from the outflows are observed also from more evolved objects. The single classical T Tauri star DG Tau shows a complex X-ray morphology: There is the outer X-ray jet emission complex, the inner X-ray emission region located at a few 10 AU from the star and the stellar X-ray emission (Güdel et al. 2008; Schneider & Schmitt 2008; Günther et al. 2009).

In order to achieve high shock velocities within the jets, strongly varying outflow velocities are required to reach X-ray emitting temperatures. The models by Bonito et al. (2010b) require ejection velocities of a few 1000 km s^{-1} in order to be reconciled with the X-ray observations. Such high velocities have not been detected in UV, optical or IR observations. However, the space and shock velocities predicted by these models are only a fraction of the initial flow velocities and therefore compatible with the observations. Also, only a fraction of the total mass-loss and energy are probably required to explain the observed X-rays. Therefore, part of the high velocity material might have escaped detection. It is not clear, if the low number of detections is caused by the low X-ray surface brightness of these jets or if only a few outflows actually emit X-rays at all.

With our third epoch high-resolution *Chandra* observation of the L1551 IRS 5 jet (HH 154) we aim to determine the time-variability of the X-ray emission in order to constrain the origin of the X-ray emission. Our article is structured as follows: We introduce in the L1551 IRS 5 region in the next section. In sect. 3 the observations and the data analysis are described. We then proceed to our results (sect. 4), which are discussed in sect. 5. We review the implications of these results on current models in sect. 6 and close with a summary in sect. 7.

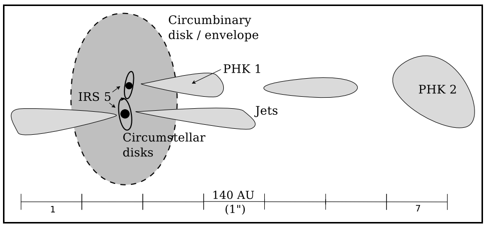

Fig. 1. Sketch of the region around the L1551 IRS 5 sources showing only a few components of the system (scales are only approximately preserved). Shown are the inner two [Fe ɪɪ] emission knots from Pyo et al. (2009). Note that the northern optical jet might actually be driven by the southern binary component (only one counter-jet is shown). The one arcsec wide stripes are used later in the article (sect. 4.2) and are shown here fore reference.

As proposed by Bonito et al. (2010b) throughout the text the term "knot" describes a region of enhanced emission while "blob" refers to a moving gas clump which is not yet shocked, i.e. not observable in X-rays.

2. L1551 IRS 5: Overview of previous observations

The Lynds 1551 (L1551) star forming region (Lynds 1962) is located at the southern end of the Taurus region at a distance of approximately 140 pc; Fig. 1 shows a sketch of the immediate region around IRS 5. Within this region, a number of protostellar objects and associated outflows have been found (e.g. Hayashi & Pyo 2009).

2.1. The L1551 IRS 5 sources

The term HH 154 describes the jet emanating from the sources collectively called L1551 IRS 5 (Strom et al. 1976). IRS 5 consists at least of a protostellar binary system and additional components are possible (see, e.g., the VLA data of Rodríguez et al. 1998). Each core is surrounded by its own circumstellar disk (~ 10 AU) and the complex is again embedded within a large envelope (~ 10000 AU; Fridlund et al. 2002). All central sources are hidden by substantial absorption of at least $A_V > 20$ mag, but probably as much as 150 mag (e.g. Snell et al. 1985; Campbell et al. 1988). Therefore, the masses of the protostars are uncertain, but from spectral mapping of the reflected light escaping the envelope Liseau et al. (2005) derived masses of 0.3 and 0.8 $M_\odot$. These masses are consistent with the total system mass of 1.2 $M_\odot$ derived by Rodríguez et al. (2003). The separation of the two sources, and consequently their jets, is only 0.35″ (50 AU). We will use the term IRS 5 for both sources jointly although most of the time the source of the northern jet is considered.

2.2. The L1551 IRS 5 jet (HH 154)

A double-lobed CO structure around L1551 IRS 5 was first detected by Snell et al. (1980). Subsequent high resolution optical and near-infrared observations revealed two separate, westwards directed jets emanating from the immediate region around the two VLA sources. They can be traced out to about 3″ (420 AU, e.g. Fridlund & Liseau 1998; Itoh et al. 2000), where they become indistinguishable (Fridlund & Liseau 1998; Pyo et al. 2003). The inner most part is only observable at radio wavelengths (e.g. Rodríguez et al. 2003). Since the northern jet is brighter and faster, it is believed to be responsible for the Herbig-Haro (HH) objects further downstream at distances between a few and 12″ (1700 AU). The jet inclination has been estimated to ~ 45° (Fridlund et al. 2005).

At a distance of about 3 arcsec away from IRS 5 proper-motion measurements of individual knots have been carried out on a baseline of 30 years, revealing substantial motion of individual knots; the inner knots show the highest space-velocities of up to 300 km/s (Fridlund et al. 2005; Bonito et al. 2008). These values are approximately consistent with highest (projected) blue shifted emission of up to 430 km/s (Fridlund et al. 2005). However, high-resolution near-infrared [Fe II] 1.644 μm observations of the inner part showed an emission complex which is virtually constant over four years (Pyo et al. 2003, 2005, 2009). The position-velocity diagrams (PVDs) show that the low-velocity component (LVC, $v < 200\,\mathrm{km\,s^{-1}}$) dominates the emission out to almost two arcsec, where the high-velocity component (HVC, $200\,\mathrm{km\,s^{-1}} < v \lesssim$ 450km/s) becomes dominant. High-resolution Hubble Space Telescope images taken in small band-pass filters (e.g., Hα, [S ɪɪ]) can be explained by a light jet (i.e., less dense than the ambient medium), hitting into a denser ambient medium (Fridlund & Liseau 1998; Hartigan et al. 2000). Spectroscopically, the outer knots show a line-width of 110 $\mathrm{km\,s^{-1}}$, densities from a few $10^3\,\mathrm{cm^{-3}}$ to $8\times10^3\,\mathrm{cm^{-3}}$ and an excitation rising with decreasing distance to IRS 5 (Liseau et al. 2005, and references therein). Concerning the nomenclature, the visual knots are designated F, E and D (in increasing distance from IRS 5, see Fridlund et al. 2005), the inner near-infrared knots are termed PHK 1...3 (Pyo et al. 2003) in increasing distance to IRS 5 (cf. Fig. 1). Knot D coincides with PHK 3 and knot F with PHK 2. Whether IRS 5 is also driving HH 28 and HH 29, which are located further downstream of HH 154, is not yet clear (Devine et al. 1999), possibly L1551 NE is their driving source.

Throughout the text we will use the term HH 154 for all outflow parts associated with the L1551 IRS 5 jet.

2.3. X-rays from HH 154

HH 154 was first discovered as an X-ray source by Favata et al. (2002) from an observation with *XMM*-Newton. Despite of the large PSF of *XMM*-Newton (~ 15 ″), the authors correctly concluded from the spectral properties of the photons that the X-ray emission cannot be associated with IRS 5 and proposed knot D as the source of the X-ray emission; knot D is the brightest optical knot and probably the current terminal working surface. Higher resolution *Chandra* observations (see Fig. 2) revealed that the X-ray source is actually located further inward towards IRS 5 at a distance of 0.5-1.0″ from IRS 5 (Bally et al. 2003). A second epoch *Chandra* exposure showed a somewhat different morphology of the X-ray emission being more elongated than the 2001 ACIS data. This elongation has been interpreted as a moving X-ray knot with a projected space velocity of about 330 $\mathrm{km\,s^{-1}}$ (Favata et al. 2006).

Based on their initial detection of X-rays from HH 2 Pravdo et al. (2001) proposed shocked, high-velocity knots as the explanation of the observed X-rays. The first analytical description of this process was presented by Raga et al. (2002) and Bonito et al. (2004) performed the first numerical hydrodynamic models with an emphasis on the X-ray emission. These models have been extended towards variable blob ejection velocities by Bonito et al. (2010a,b) and their analysis revealed that very fast blob velocities of more than 1000 km/s are needed in order to explain the observations by shock heating, i.e., by internal shocks occurring when fast blobs overtake slower ones. An ejection "period" of two years matched the X-ray observations best.

3. Observations and data analysis

Table 1 lists all the available X-ray observations of HH 154. We used the ACIS-S detector for the third epoch *Chandra* exposure, since the back-illuminated ACIS-S chip has a higher sensitivity at lower energies than the front-illuminated ACIS-I CCDs. With the VFAINT mode, this setup provides a similar sensitivity as the longest ACIS-I exposure for the energies at hand; and an even higher sensitivity for plasma at cooler temperatures as expected for individual knots moving outwards and cooling.

We used *CIAO* version 4.2 throughout the data analysis and followed the science threads on the *CIAO* webpage[1]. The ACIS-S observation was reprocessed to account for the VFAINT-mode[2]. We experimented with pixel randomization, but since the relevant scales are usually at least twice the detector pixel scale, the effect of pixel randomization is virtually negligible. We explicitly note in the text where we expect this assumption to be invalid.

In order to improve the astrometric accuracy, the three *Chandra* observations of HH 154 were aligned by calculating the centroids of the brightest sources detected by the *CIAO* tool `celldetect` and the photon events were reprojected so that the mean offset between these centroids vanishes. We use the offset obtained from the three brightest sources weighted by the square-root of their count-number. These sources are also members of the Taurus star forming region and located on the ACIS-S part of the CCD array. Using more sources (detected with S/N>3) and equally weighted or photon number weighted means changes the offset by less than 0.5 pixel (0.25″). Thus, relative positions are at least accurate to within one pixel (0.49″). For a cross-check of the positions we calculated the centroid positions of HH 154 using the photons within a circle of 2.5 pixel radius centered on the brightest emission peak in the energy range 0.5 - 3.0 keV. They coincide to within approximately 0.3″, well within our estimated accuracy. Note that these centroids should coincide only in case of a stationary source. We give distances relative to the radio position with respect to the nominal positions of the 2001 observation where the comparison sources show a good agreement with their optical positions but note that this position is accurate only within 0.5″.

We also retrieved the archival *XMM*-Newton data (Obs-ID 0109060301) from 2000 for a spectral cross-check and eleven exposures during March 2004 (Obs-ID 0200810201…0200811301), where HH 154 is located about two arcmin off-center for a luminosity check. SAS 9.0[3] was used for the analysis of the XMM-Newton data. We extracted the source photons within a circle of 15″ around the source position of HH 154 for the March 2004 exposures and derived the background from a nearby source-free region. We concentrated on the MOS data since the PN suffers high background levels (using standard filters only 40 ks PN on-time remain). However, both count-rates agree within their respective 1σ ranges. We converted the count rate to luminosity by assuming the same spectral properties as during the 2001 XMM-Newton observation.

[1]`http://cxc.harvard.edu/ciao/`
[2]`http://cxc.harvard.edu/ciao/threads/createL2/`
[3]`http://xmm.esa.int/sas/`

Table 1. Analysed X-ray observations of HH 154.

Date	Observatory	Setup	Obs-ID	exp. time
2000-09-09	XMM-Newton	–	0109060301	56 ks
2001-07-23	*Chandra*	ACIS-I	1866	80 ks
2004-03-…[a]	XMM-Newton	–	0200810201…	107 ks
2005-10-27	*Chandra*	ACIS-I	5381	98 ks
2009-12-29	*Chandra*	ACIS-S	11016	66 ks

[a]This dataset consists of 11 short exposure distributed over six days in March 2004 where HH 154 is off-axis by about 2 arcmin.

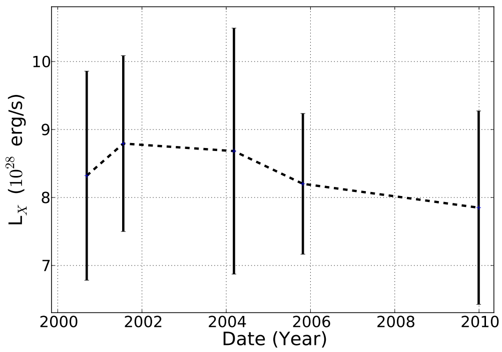

Fig. 3. Unabsorbed X-ray luminosity (0.5-10 keV) of HH 154 including the XMM-Newton data for the 2000 and 2004 data points. As the XMM-Newton data lacks sufficient spatial resolution to resolve the X-ray emission, the displayed luminosity pertains to the total observed X-ray emission for all datasets.

4. Results

The X-ray images of HH 154 in the 0.5–3.0 keV energy band for the three available *Chandra* observations are shown in Fig. 2. To extract photons we use an ellipse with a semi-axis lengths of 3.7″ and 2.3″, respectively, whose semi-major axis is aligned with the centroid in declination, i.e., which is aligned approximately with the jet axis and contains all photons attributable to the X-ray emission of HH 154. Using a nearby source free background region (no X-ray sources detected nor a 2MASS (Skrutskie et al. 2006) or SIMBAD[4] source known), the expected background ($E_{photon} = 0.5\ldots3.0$ keV) within the ellipse is 0.7 photons for the 2001 observation), 1.0 for the 2005 observation and 1.4 in the 2009 observation.

4.1. Energetics

We used XSPEC v12.5.0 (Arnaud 1996) for the spectral modeling and assumed that the observed material can be described by optically thin thermal plasma emission (APEC, Smith et al. 2001) and included absorption by neutral gas along the line of sight in our fits. We set the abundance to half the solar value (using Anders & Grevesse 1989) since the XEST survey of the Taurus region found on average a sub-solar metallicity (Güdel et al. 2007a).

Figure 3 shows the unabsorbed X-ray luminosity of HH 154 during the last decade. It clearly indicates that the luminosity in

[4]`http://simbad.u-strasbg.fr/simbad/`

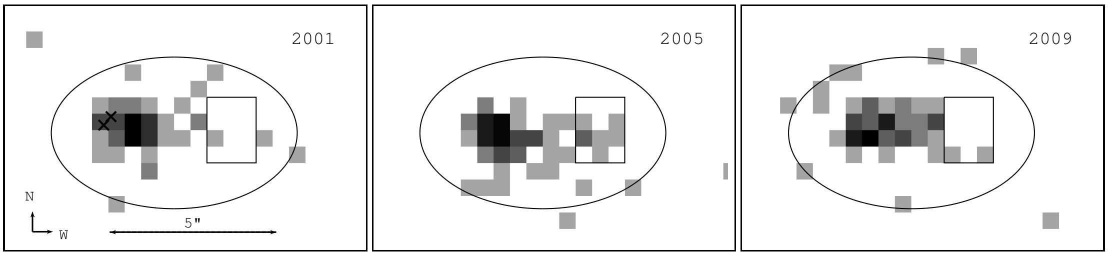

Fig. 2. The ellipse for the global plasma properties, also, the location of the 2005 "knot" is shown. The crosses indicate the position of the radio sources and their size approximately indicates the position uncertainty.

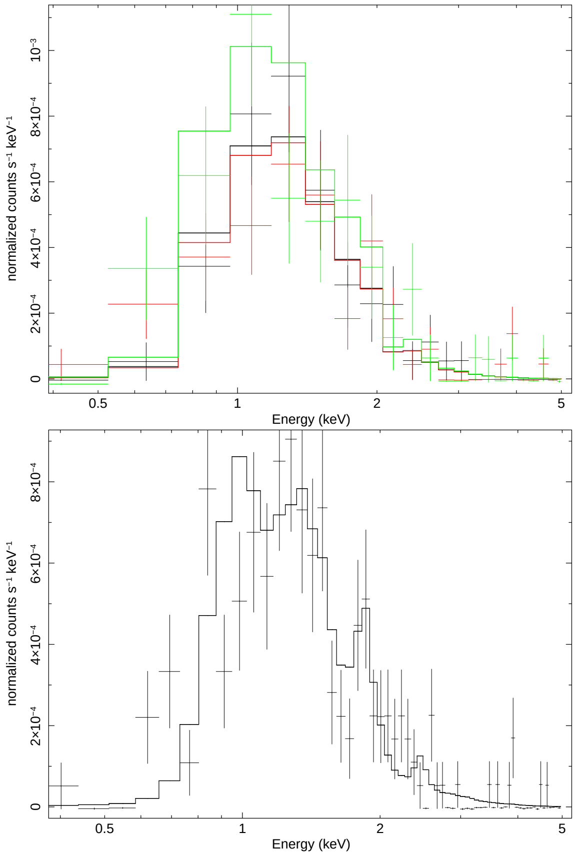

Fig. 4. Spectrum of all photons within the ellipse (see Fig. 2). **T**op: Individual spectra, **B**ottom: Co-added spectra (the Si-lines around 1.8 keV are clearly visible).

the the HH 154 region appears constant and deviations from the mean value do not exceed 22%.

4.1.1. Global plasma properties

The spectra extracted using the photons within the ellipse are shown in Fig. 4, however, we caution that the assumption of homogeneous plasma properties throughout the emitting region is probably not valid (see sect. 4.1.2). Averaging over different plasma properties leads to an unstable fit with two solutions describing the data reasonably well; the two possibilities are listed in Tab. 2 (top). One solution is only weakly absorbed and requires rather high plasma temperatures. Although this solution is statistically favored, we regard this solution as physically less plausible due to the following reasons. The Si lines at ~1.9 keV are not reproduced by this model but clearly present in the data (bottom panel of Fig. 4) and the low N_H value contrasts the high absorption derived for the region close to the driving sources ($N_H \gtrsim 10^{23}$ cm^{-2}) and along the jet axis ($N_H \gtrsim 8 \times 10^{21}$ cm^{-2}, e.g. Itoh et al. 2000; Fridlund et al. 2005). In the following, we will therefore concentrate on the fit solution I with higher absorption and lower plasma temperature. The plasma properties within the ellipse are compatible with each other for the individual exposures (1σ). The discrepancy between the values given by Favata et al. (2002) and our values results partly from the change of metallicity (the respective 1σ ranges overlap for solar metallicity).

In order to estimate an upper limit for the presence of cooler plasma, we added a second temperature component to the fit and fixed its temperature to 0.3 keV (0.2 keV). The 1σ upper limit on the luminosity of this cool component is 1.4×10^{29} erg s^{-1} (3.0×10^{29} erg s^{-1}) when the absorption is forced to the value of the one temperature fit which also agrees with the optical/near-infrared value. Allowing the absorption to vary, the luminosity of the low temperature component decreases as the absorption also decreases for this two temperature component fit.

4.1.2. Local plasma properties

For a quantitative comparison of the three *Chandra* observations we divide the region around HH 154 into ~ 1″ (2 ACIS pixels) wide spatial bins as indicated in Fig. 6. For a point source about 80% of the photons are located in these 1″ wide stripes. This procedure is essentially a projection of the photon number onto the flow-axes (i.e., the x-axis). Figure 6 shows the result for the individual exposures. Naturally, the exact values depend on the stripes used, therefore, we checked the results by shifting the stripes or using a different width of the stripes (about 90% of the photons of a point-source would be included in a three pixel wide stripe). Any property which depends crucially on the choice of the stripes is regarded as an unphysical artifact (Tab. 3).

The mean energy of the photons in the individual strips along the flow axis is displayed in Fig. 5 (top panel), showing a clear decrease of photon energy with increasing distance to the driving source.

The slope of the mean energy depends on the detector's spectral response and on the stripes used. However, the spectral softening with increasing distance is independent of the detector re-

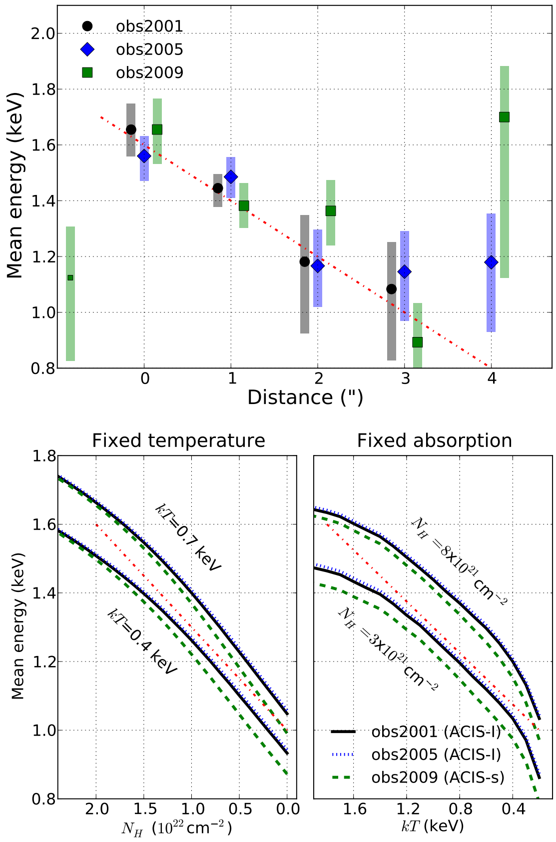

Fig. 5. Trend of mean energies, stripes are those of Fig. 6. Photons used within 0.5-3.0 keV. The red dash-dotted line is intended to guide the eye in the lower panel. **Top:** Thick symbols indicate data points with more than three photons while the smaller symbols refer to data points with fewer photons. Errors are obtained using the simulations of sect. 4.1.2. Distances are estimated with respect to the nominal center of the radio source in the 2001 observation but note that the absolute position uncertainty is approximately 0.5″. **Bottom:** Simulations for fixed temperature and fixed absorption along the jet axis.

Table 2. Plasma properties of HH 154 with 1σ errors. Spectra are binned to ~ 44 eV wide channels, i.e. about three times oversampling the intrinsic energy resolution of the ACIS detectors, we used c-stat and the energy range 0.5-5.0 keV. Unabsorbed fluxes (0.5-10. keV) are given.

	N_H (10^{22} cm^{-2})	kT (keV)	EM (10^{51} cm^{-3})	F_X (10^{27} erg/s)
Composite spectrum (ellipse)				
Solution I	1.1 ± 0.1	0.6 ± 0.1	7.9±2.2	$82.7^{+20.0}_{-21.8}$
obs2001^a			$8.6^{+2.6}_{-1.8}$	$89.7^{+24.3}_{-24.4}$
obs2005 ^{a}			$7.7^{+2.3}_{-3.4}$	$81.6^{+21.7}_{-21.8}$
obs2009 ^{a}			$7.4^{+2.2}_{-3.4}$	$77.6^{+21.4}_{-21.0}$
Solution II	0.2 ± 0.1	$1.8^{+0.3}_{-0.1}$	1.9±0.2	$18.4^{+2.1}_{-1.9}$
Individual spectra (ellipse)				
XMM (2000)	1.0 ±0.1	0.5 ±0.1	$8.4^{+3.6}_{-2.0}$	$89.7^{+29.2}_{-20.2}$
obs2001	$1.1^{+0.2}_{-0.3}$	$0.6^{+0.4}_{-0.1}$	$8.9^{+6.4}_{-5.3}$	$97.2^{+37.1}_{-33.2}$
obs2005	1.1 ± 0.2	0.6± 0.1	$7.8^{+3.5}_{-2.7}$	$79.8^{+28.7}_{-25.5}$
obs2009	1.0 ± 0.2	$0.6^{+0.2}_{-0.1}$	$7.0^{+3.5}_{-2.9}$	$73.4^{+32.7}_{-29.7}$
Composite spectra				
Eastern region	$1.4^{+0.2}_{-0.3}$	0.7±0.2	$6.6^{+2.7}_{-0.1}$	78.1
Western region	$0.6^{+0.3}_{-0.2}$	0.3±0.2	$0.4^{+0.9}_{-0.4}$	5.0

$^a N_H$ and kT fixed to values from co-added spectra

sponse since only relative changes within the same detector are compared.

For a cross check of the trend of the mean energy, we divided the emission region into a "eastern" and a "western" region so that the component close to the driving source(s) is associated with the "eastern" region and the outer part of the emission with the "western" region (these two regions essentially split stripes 2-7 into 2 separate regions); Table 2 lists the associated fit results. Since the total number of counts in the right region is only 42 when summed over all ACIS exposures ($E_{\rm photon}$ = 0.3–5.0 keV), we checked the results by fixing either the temperature or the absorption to the values obtained for the left part of the emission, this results in a decrease of the N_H value consistent with Fig. 5 and the temperature for the right emission component, respectively.

Figure 5 (bottom panel) shows the change required in either the plasma temperature or the absorption to explain the trend of the mean photon energy; fixing one parameter requires large changes of the other parameter ($N_H = 2 \times 10^{22} \rightarrow 0$ cm^{-2} or $kT = 1.2 \rightarrow 0.2$ keV).

The errors shown in Fig. 5 (top) were obtained by simulating spectra containing a specified number of photons and then calculating the mean energy range which contains 68 % of the trials. For photon numbers larger than ~20, the error (±0.1 keV) depends only very weakly on the number of photons; furthermore, the error depends only weakly on the assumed plasma properties for the spectra at hand.

4.2. Morphology along the jet axis

The structure of the X-ray emitting region observed in 2009 neither resembles the structure present in 2001 or 2005; it is more extended than the 2001 structure, but does not show excess emission as far downstream as the 2005 exposure. The emission region close to the driving source, which is also present in all previous exposures, is most notable. The new ACIS-S observation does not show a clear knot westwards (downstream) of the main emission component as suggested by the 2005 image and there is no X-ray emission even further downstream as would be expected for a moving knot of constant luminosity. Note that the ACIS-S exposure is more sensitive to low energy photons than the 2005 ACIS-I exposure and that, according to Fig. 6, the photons soften with increasing distance to the driving source. Therefore, any emission with comparable properties as the photons attributed to the "knot" should be detectable with the 2009 ACIS-S observation. Furthermore, there are no photons detected westward (downflow) of the 2005 recorded photons.

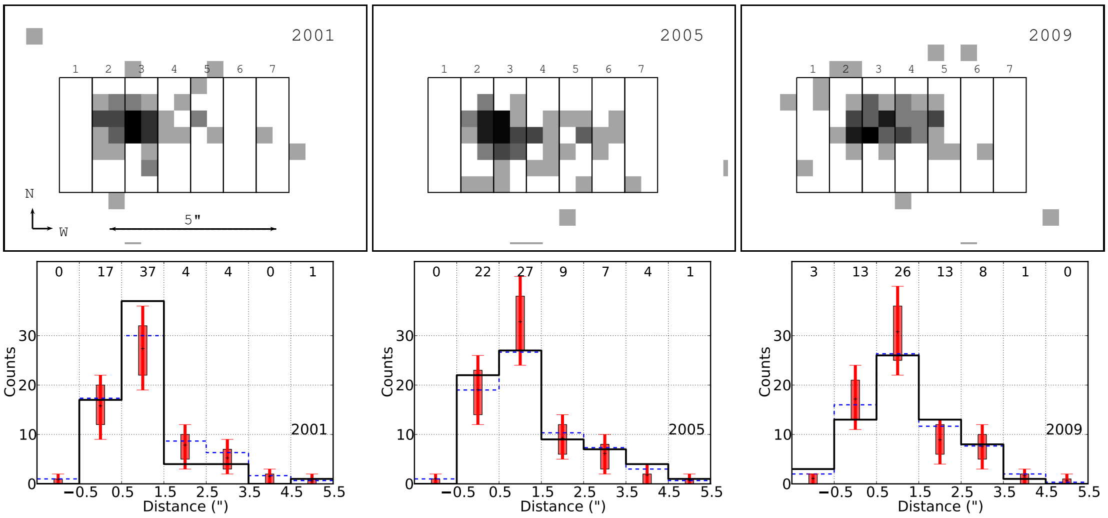

Fig. 6. One example of stripes (1″width) used to extract count numbers, mean energies and spectra. In the bottom row, the projection onto the outflow direction (here assumed to coincide with the x-axis) is shown, the thick black line is the measured photon number, the thin blue dashed line indicates the mean photon number ignoring differences in the efficiency of the individual exposures. The red bars indicate the expectation value for a constant emission, shown are the 70 % and 90 % probability ranges. Distances are given as in Fig. 5.

Table 3. Stripe properties (mean energy is in keV).

Observation		Stripe					
		1	2	3	4	5	6
2001	Counts	0	17	37	4	4	0
	Mean energy	–	1.7	1.4	1.2	1.1	–
2005	Counts	0	22	28	9	7	4
	Mean energy	–	1.6	1.4	1.2	1.1	1.2
2009	Counts	3	13	26	13	8	1
	Mean energy	1.2	1.7	1.4	1.4	0.9	1.7
		Stripes shifted by 0.5″					
2001	Counts	7	33	16	5	1	1
	Mean energy	1.7	1.5	1.3	1.2	1.2	1.0
2005	Counts	4	36	14	6	7	3
	Mean energy	1.8	1.5	1.4	1.2	1.0	1.6
2009	Counts	3	27	19	12	1	1
	Mean energy	1.2	1.6	1.3	1.1	1.2	1.7

Table 4. Spectral models for sect. 4.2.1

Model	N_H (10^{22} cm^{-2})	kT (keV)
Best fit values	1.1	0.6
Fixed temperature	0.0–2.0	0.5
Fixed absorption	0.6	0.3–1.2

4.2.1. Comparison of the *Chandra* observations

A direct comparison of the photon numbers is not possible due to (a) different exposure times and (b) different detector responses. Nevertheless, we show in Fig. 6 the mean photon number ignoring the differences in the sensitivity of the individual exposures. We note that all observations are compatible with this rough mean value using the error obtained by Gehrels weighting (Gehrels 1986).

For a more detailed comparison of the observations, a spectral model is constructed (not fitted) in each stripe. We experimented with models which use the overall best fit values and with models which reproduce the trend in the mean energies (see Fig. 5), they are listed in Tab. 4. As the predicted count numbers differ by less than one count, the statistical error overwhelms the error due to the unknown spectrum. Due to the different energy response of the 2001 ACIS-I and 2009 ACIS-S, the scaling factors relative to the 2005 observation are 0.83. . . 0.87 and 0.91. . . 1.20 depending on the assumed spectra (high photon energy and low photon energy, respectively).

The individual stripe models are normalized so that the total count number summed over the three ACIS observations in each stripe is conserved. Thus, the predicted total count number in a single stripe matches the observed value, which is statistically the best estimate for the model normalization for constant emission. Figure 6 exemplarily shows the result for the model with $kT = 0.5$ keV and variable absorption along the flow-axis (which is virtually indistinguishable from the model with constant absorption and variable temperature).

4.2.2. Time variable emission?

To test if the observations are statistically consistent with the hypothesis of constant emission, we perform Monte-Carlo simulations to estimate a confidence interval to accept or reject this hypothesis, i.e., to check if the observed photon distribution is an exceptional realization for a constant emitting region. Since neither the time when new blobs appear nor their speed is predicted by current theories, the location of a new blob is not known a priori. Therefore, the statistical significance of any count number enhancement in a given region depends on the number of independent regions in which such an enhancement would be considered a knot. Essentially any stripe in Fig. 6 can be regarded as a possible region for a knot, however, the result does not depend strongly on, e.g., the inclusion of stripes 1 or 7, although the general result does depend strongly on the set of stripes used. To ensure that our results are not biased by the particular selection of stripes, we repeated the simulation for different sets of stripes,

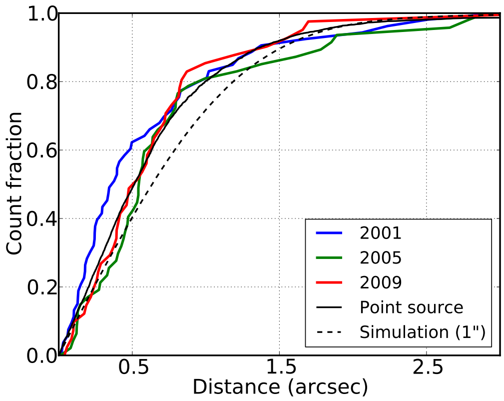

Fig. 7. Encircled count fraction perpendicular to the jet axis using essentially the photons within stripes 2 and 3 in Fig. 6. The MARX simulation shows a source with an extent of 1″for comparison.

which are two or three pixels wide and which have mutual offsets of one pixel.

One simulation involves a set of three new exposures simulated as new individual photon numbers for each stripe. These simulated photon numbers were based on the expected photon number in that stripe (sect. 4.2.1) and Poisson statistics. The individual likelihoods, i.e., the likelihoods to observed exactly the simulated photon number in a given stripe-observation combination, depend on the assumed expectation value for the photon number in this particular stripe. We derived this expectation value a posteriori from the simulated counts in a particular stripe using the relative efficiencies from sect. 4.2.1. The total likelihood for each simulation was then calculated as the product of the individual likelihoods. Thus, the fraction of realizations with a total likelihood better than the observed one can be interpreted as the probability for time variability. We find probabilities between approximately 50% and 96% depending on the exact stripes used. The lowest and the highest probability values were found for the three pixel wide stripes. Note that the favorable choice of stripes for the 2005 "knot" region is the driver for the high significance result. The corresponding stripe, considered on its own, has a significance for variability of more than 95 %. Also note that this approach does not include background events or other detector effects like alignment errors between the individual exposures.

In summary, the *Chandra* X-ray observations can be regarded as statistically compatible with time constant X-ray emission. However, the significance is poorly constrained as it depends crucially on the stripes used. The inability to find a clear sign for time dependence independent of the stripes used might be caused by the low number of counts since the 90 % confidence level easily covers a range almost twice as large as the value itself in the outer regions of the outflow. Therefore small scale time variability may be present, however, statistically time-dependent emission is not required. Note, however, that the "knot" region shows exactly the count number pattern expected from a transient knot.

4.3. Extent perpendicular to the flow direction

In order to check whether the *Chandra* exposures show evidence for an extent of the emission perpendicular to the jet axis, we have to take into account the exact position angle of the jet. Otherwise, the distribution of the photons around the jet axis would be artificially broader. We adopt a PA of 261° for the outflow (Pyo et al. 2009).

Since we know the absolute position of the jet axis only to 0.5″, we estimate its position by the mean position of the photons perpendicular to the jet axis. Figure 7 shows the distribution of the photons perpendicular to the jet axis for the photons approximately in stripes 2 and 3 in Fig. 6. Due to the slight inclination of the jet axis with the x-axis, both regions do not overlap exactly. This figure also includes a Marx[5] simulation of an extended (1″) source for comparison. From this figure it is evident that the X-ray emitting region is smaller than 1″– and possibly smaller than 0.5″. We adopt a maximum extent of 0.5″for the lateral source extent but note that a source size smaller than this value is possible. We also note that the superposition of a number of smaller emission regions can mimic the observed photon distribution, thus making the physical extent of the emission region smaller than 0.5″.

Figure 7 shows slight deviations between the individual exposures, whether these are due statistical fluctuations or due to intrinsic changes in the emission region is hard to judge since variations are most evident on sub-pixel scales where, even with pixel-randomization turned off, the photon locations within the individual detector pixel become important. The standard deviation of the photon distances to the jet axis are 0.65, 0.69, 0.59 pixel (which is 0.492″) for the 2001, 2005 and 2009 observation, respectively (energy range 0.5-3.0 keV), i.e., rather similar values; the standard deviation for a point source is 0.57. Therefore, we will concentrate in the following on changes of the plasma properties along the jet axis instead of changes perpendicular to it.

5. Discussion

The interpretation of the X-ray findings depends crucially on the required mass loss rate, shock velocity, plasma density and the cooling time of the X-ray plasma within the flow. Therefore, we start our discussion by deriving estimates for their respective values.

5.1. Mass loss rate and shock velocities

Using the formula given in Schneider & Schmitt (2008, eq. 2) for the massloss rate required to explain the observed X-ray emission we find $\dot{M}_{X-ray} \approx 1.5 \times 10^{-12}\, M_\odot\, \mathrm{yr}^{-1}$ or approximately a factor of 10 lower than the inner X-ray emission component of DG Tau. This formula assumes that the material observed with *Chandra* is shocked only once, which should be a relatively good approximation since high shock velocities are required to heat the material above $T \gtrsim 10^6$ K. According to Raga et al. (2002), shock velocities of approximately 700 km s^{-1} are needed to heat the material to the observed 0.6 keV close to IRS 5, while only v_{shock} ≈550 km s^{-1} is needed for the lower temperature at larger distances in case this outer X-ray emitting plasma is heated in situ and not the cooled down remnant of the inner X-ray component.

[5] `http://space.mit.edu/cxc/marx/`

5.2. Densities

The low densities of the HH flows cannot be directly measured with X-rays, however, we can derive a lower limit on the density assuming a certain emission volume. From our analysis of the source extent in sect. 4.2.1 and sect. 4.3. we assume that the emitting volume is extended perpendicularly to the jet axis by $0.5'' \hat{=} 70$ AU and along the jet axis by $2''$ and estimate that at least 80 % of the photons originate in this region. These estimate translates into a maximum volume of 5×10^{45} cm^{-3} for an inclination angle of 45°. For a filling factor of unity, the electron density of X-ray emitting plasma is then

$$n_X = \sqrt{\frac{EM}{0.85 \cdot V}} \approx 1400 \text{ cm}^{-3}. \quad (1)$$

This value is a lower limit on the density since the plasma might be concentrated in individual denser clumps, i.e., the volume filling factor could be less than unity. Very close or co-spatial to the X-ray emission material of lower temperatures ($\sim 10^4$ K) has been observed (e.g. [Fe II]), so we consider a filling factor of unity rather unlikely since some intermediate temperature material will connect both temperature components.

In the optical and near-IR direct density values from line ratios have been derived mainly for the outer part of the jet where densities of a few 10^3 cm^{-3} are found (e.g. $n_e = 7.6 \times 10^4$ cm^{-3}, Liseau et al. 2005). Densities up to 10^6 cm^{-3} have been derived for the inner $2''$ by Itoh et al. (2000) from an analysis of [Fe II] near-infrared lines. Note that the [Fe II] lines have a higher critical density than the [S II] lines usually used for the density measurement. High hydrogen densities have also been found close to the driving sources for a few other sources (e.g. Melnikov et al. 2009; Bacciotti et al. 2000).

Considering the thermal pressures of these two temperature components, we find that the lower limit on the thermal pressure of the X-ray emitting plasma ($T_X \approx 7 \times 10^6$ K) is

$$P_X = 2\, n_X k_B T_X \approx 3 \times 10^{-6} \text{ dyn/cm}^2 . \quad (2)$$

The high densities of the material observed in [Fe II] results in an approximate thermodynamic pressure equilibrium of both components, i.e., densities of a few times 10^6 cm^{-3} suffice to provide the required pressure at a temperature of $T \approx 10^4$ K. This would imply that the density within the jet increases by approximately two orders of magnitude within the innermost $5'' \hat{=} 1000$ AU (deprojected).

A conical outflow decreases its density by exactly two orders of magnitude from $0.5''$ to $5''$. However, HH 154 is likely not strictly conical since Fridlund et al. (2005) noted that the opening angle close to the driving source might be as large as 90°, which is consistent with the estimated lateral jet size of $0.5''$ by Pyo et al. (2002) at this distance. Therefore, the density decrease beyond $0.5''$ is probably less than for a conical outflow as an opening angle of only about 3° (see footnote [6]) does not suffice to decrease the density sufficiently for large inital opening angles. Thus, it is not clear if or where the "cold" jet component is in pressure equilibrium with the X-ray emitting plasma.

Another possibility is that the magnetic pressure supports the X-ray emitting volume against expansion. We estimate its strength by assuming a plasma-β of unity ($B^2 = 8\pi P_{gas}$) and find $B \approx 6$ mG . Such a value is reasonable close to the driving source (see Tab. 1 in Hartigan et al. 2007) and requires lower densities ($n_e \gtrsim 4 \times 10^4$ cm^{-3}) as pure pressure support if the magnetic field scales with the density as expected ($B \sim n^p$ with $p = 0.5 \ldots 1$) since measured magnetic fields in HH objects indicate 15 μG for $n = 100$ cm^{-3} (Hartigan et al. 2007). For the lower temperature material, an external magnetic field seems too weak to collimate the jet (Cabrit 2007), however, MHD self-collimation seems a reasonable scenario, thus the wound-up (helical) magnetic can lend pressure support for the X-ray emitting plasma largely inhibiting lateral expansion of the hot X-ray emitting material.

[6]The size of the Mach-disk of knot D located at a distance of $\sim 10''$ ($0.6''$, Fridlund et al. 2005) indicates the local size of the jet.

5.3. Plasma cooling

Three processes contribute to the cooling of a plasma: Radiative cooling, cooling by expansion and thermal conduction. The pressure work done by the plasma is $\delta W = p dV$ and the radiative losses are

$$\delta Q_{rad} = -n_e^2 V(t) \Lambda(T) dt\, , \quad (3)$$

where n_e is the electron density, V the volume and $\Lambda(T)$ is the cooling function. The conductive heat flux is given by

$$q_{cond} = -\kappa(T) \bigtriangledown T\, , \quad (4)$$

where the thermal conductivity according to Spitzer is

$$\kappa(T) = \kappa_0 \frac{T^{5/2}}{\ln \Lambda} \text{ erg s}^{-1} \text{ K}^{-1} \text{ cm} \quad (5)$$

with $\kappa_0 = 1.8 \times 10^{-5}$ and the Coulomb logarithm $\ln \Lambda$, which describes the collision properties of the plasma and is of order 10. When the mean free path length for energy exchange is of the same order as the thermal scale height, the conduction should be approximated by the saturated flux

$$q_{sat} = 5 \phi \rho c_s^3\, , \quad (6)$$

with $\phi \approx 0.3$ (e.g. Borkowski et al. 1989, ρ is the mass density and c_s is the local sound speed). For an estimate of the importance of the saturated flux, we assumed a linear temperature decrease. Under these circumstances the Spitzer value exceeds the saturated flux on spatial scales of about 10 AU for the cooling from $T_1 = 10^6$ K to $T_0 = 10^4$ K, i.e., the saturated flux should be used for these steep gradients ($n \approx 10^3$).

Thermodynamics states that the energy change of a plasma cell is described by

$$dU + \delta W = \delta Q = \delta Q_{rad} + q_{cond} \cdot A\, dt \quad (7)$$

with the internal energy $U = \alpha NkT$ ($\alpha = 3/2$ for a fully ionized plasma), the particle number N, the Boltzmann constant k, the temperature T and A is the surface area through which heat conduction proceeds. We use $p = 2n_e kT$ in the expression for the pressure work and follow Güdel et al. (2008) by writing eq. 7 as

$$\alpha \frac{dT}{T(t)} + \frac{dV}{V} = -\left(\frac{n_e \Lambda(T)}{2kT(t)} + \frac{\kappa_0}{2n_e VkT} \cdot A \frac{T^{5/2}}{\ln \Lambda} \nabla T \right) dt\, , \quad (8)$$

where we used $N_e = n_e \cdot V$ and note that this expression holds only in the presence of sufficiently small temperature gradients.

In order to estimate the relative importance of the three cooling terms, additional information is needed, in particular, the opening angle of the X-ray emitting jet, its density structure, the temperature gradient, the surface for the heat conduction, which would include the magnetic topology and the properties of the environment, e.g., its ionization. These quantities are not available for the X-ray emitting part of the jet. We therefore decided to give some order of magnitude estimates for the cooling times

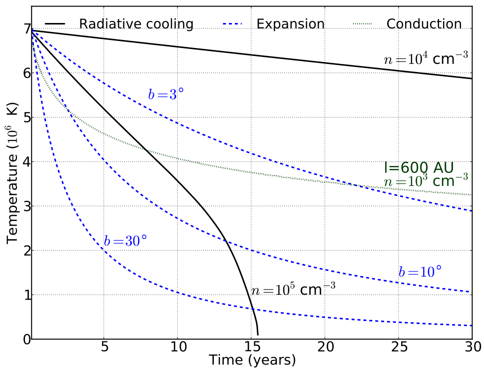

Fig. 8. Cooling curves for the different cooling processes.

of the individual processes ignoring contributions of the other ones. As we will see, there are distinct regions in the parameter space where each process seems to dominate, so we regard this approach reasonable.

Figure 8 shows the cooling curves for the different processes assuming different parameters for the jet. For radiative and conductive cooling, the mapping of time to distance in this figure depends on the actual, deprojected space velocity of the plasma. A rough estimate is 0.3″ yr^{-1}, which implies that today's inner X-ray emission will reach the position of today's outer emission in 15 years. Adiabatic cooling, on the other hand, does not depend of the outflow velocity but only on the initial cross-section of the plasma and on the opening angle.

5.3.1. Adiabatic cooling

Protostellar jets usually show an approximately conical structure at some distance from the driving sources so that the flow expands mainly perpendicular to the jet axis. In the limit of adiabatic cooling

$$T\, V^{\gamma-1} = \text{const} \tag{9}$$

holds. Since we do not observe local temperatures, we have to average the temperature, weighted by density[7], over the volume used to measure the temperature. We use the following approximation for the volume of the plasma cell

$$V = \pi l\,(r_0 + r\tan b)^2\ , \tag{10}$$

where $r(t) = v \cdot t$ is the position along the jet axis measured from the initial distance, while $r_0 = 0.25''$ is the initial jet radius at this position and $2 \cdot b$ the opening angle (l is the length of the cell along the jet axis). The initial cross-section is fixed and the temperature decrease depends only on the position along the outflow. From the size of the Mach disk about 10″ from the driving sources, we estimate an opening angle of 3 – 10° for the flow, where the separation of the working surface and the Mach disk argues for values closer to 3°. Different outflow velocities would change the curve for the expansion cooling in Fig. 8 but would not lead to another spatial temperature structure, because the dependence on v cancels out in the equations.

[7]Note that $EM = n^2\, V = n\, N$ with a constant number of particles N in each cell.

As described by Güdel et al. (2008), the expansion additionally reduces the density of the emitting plasma and thereby lowers the number of emitted photons more strongly than expected on the basis of the temperature decrease alone. For a consistency check, we calculated the expected number of photons at 3.5″ from the driving sources from the ratio of the emission measures at 0.5″ and 3.5″ and the drop in temperature. Assuming constant absorption, we expect a drop in photon number by approximately a factor of about 6 from 0.5″ to 3.5″ for an opening angle of 3°, which is approximately compatible with the observed value. The larger opening angle of 10° would reduce the photon number more strongly, i.e., the combination of the temperature and density decrease reduces the expected photon number by about 200 for the same distance.

5.3.2. Radiation cooling

We solved eq. 8 using the cooling function of Chianti version 6.0 (Dere et al. 1997, 2009) assuming half solar metallicity. Figure 8 shows two cooling curves for radiative cooling. According to eq. 8, the cooling time depends linearly on the density. It is clear that radiative cooling does not contribute significantly to the cooling as long as the density does not exceed $n \approx 10^4\,\text{cm}^{-3}$.

5.3.3. Conductive cooling

Magnetic fields are essential for the launching of jets, but even at greater distances, small magnetic fields (∼ 100 μG) influence the jet dynamics (Hartigan et al. 2007). They can also strongly suppress heat conduction perpendicular to the field lines even for weak fields (∼ 1μ G, see eq. 5-53 in Spitzer 1962). In the presence of turbulent magnetic fields, heat conduction might be suppressed by about two orders of magnitude or even enhanced relative to the Spitzer value (e.g. Narayan & Medvedev 2001; Cho et al. 2003; Lazarian 2006) depending on the scale of the turbulence. We regard it as plausible that heat conduction works most efficiently along the jet axis while it is suppressed by some kind of magnetic field (e.g. helical, Chrysostomou et al. 2007; Staff et al. 2010) perpendicular to the jet axis. The Spitzer value for the heat conduction assumes an ionized plasma, which might not be entirely true throughout the jet, however, a considerable amount of ionized material should be present close to the X-ray emitting plasma. Given these uncertainties, we estimate conductive cooling by

$$\tau \ = \ 2.6\times10^{-9}\frac{nl^2}{T^{5/2}}\,\text{s} \tag{11}$$

$$\approx\ 52\left(\frac{n}{1000\,\text{cm}^{-3}}\right)\left(\frac{l}{210\,\text{AU}}\right)^2\left(\frac{T}{3\times10^6\,\text{K}}\right)^{-5/2}\ \text{years} \tag{12}$$

given in Orlando et al. (2005). We show in Fig. 8 a cooling curve by numerically integrating the conductive cooling for a fixed density n and for cylindrical geometry ($V \approx A \cdot l$). The effect of the conductive cooling depends on the density of the plasma and on the temperature gradient, i.e., on the cooling length (we assumed 600 AU for a temperature decrease from 0.6 keV to 0.1 keV). The curve shown in Fig. 8 is intended to give a rough impression of this effect and we caution that the provided estimate for the conductive cooling might be off by orders of magnitude in some scenarios, e.g., for turbulent magnetic fields.

5.3.4. Cool conclusions

From Fig. 8 it is clear that cooling by expansion dominates over radiation. Whether conduction is important depends on the density, the temperature gradient and the magnetic field configuration. When no heat is transferred perpendicular to the jet axis, we expect adiabatic cooling to dominate. We will therefore focus on that cooling process in the following.

5.4. Trend in mean energy

Judging from the absorption value ($N_H \approx 1.4 \times 10^{22}$ cm^{-2}) close to the driving sources, the visual absorbing magnitude is approximately $A_V \approx 8$ mag (Vuong et al. 2003). Itoh et al. (2000) analyzed the [Fe II] 1.644 μm/1.257 μm line-ratio as an estimate for the evolution of the visual extinction along the jet axis and found a value of $A_V \approx 7$ for distances greater than 1″ from IRS 5. This is compatible with our estimate from the X-ray spectrum. Therefore, we expect that the correlation of A_V and N_H holds in the jet region. Closer to the driving sources the extinction increases up to $A_V \approx 21$. Fridlund et al. (2005) also derived A_V-values, which are slightly lower than the values of Itoh et al. (2000) for the optical knots located further downstream. They find that the extinction decreases slowly towards the outer knots where $A_V \approx 2-3$ is found. At the position of knot F which is closest to the driving sources, they estimate an absorption of $A_V > 4$.

Assuming that the absorbing column density decreases from $N_H = 1.4 \times 10^{22}$ cm^{-2} at 1″ from the driving sources to $N_H = 8 \times 10^{21}$ cm^{-2} at 5″, the plasma temperature still has to decrease from 0.7 keV to 0.4 keV in order to explain the decrease in the mean energy. We therefore conclude that the temperature decrease of the X-ray plasma significantly contributes to the softening of the photons beyond ≈ 1″. It is possible that emission is coming frp, the innermost 1″ where it is more strongly absorbed. For an upper limit on the temperature change along the flow axis, we fix the absorption to $N_H = 8 \times 10^{21}$ cm^{-2}, which requires, according to Fig. 5, that the plasma temperature decreases from approximately 1.7 keV to below 0.2 keV within 3″.

An opening angle of a few degrees reduces the plasma temperature along the outflow as required by the above estimates, consistent with the assumption that adiabatic cooling dominates the plasma cooling. As discussed in sect. 5.3.1 the reduction of photons along the jet axis is compatible with a shallow opening angle.

As we have no good estimate for the cooling time of the plasma, it is possible that cooling is very efficient and re-heating of the X-ray emitting plasma along the inner few arcsec is required in order to produce observed X-ray emission at larger distances from the driving sources. However, the temperature decrease along the jet axis remains virtually constant over 10 years of observation so that also the hypothetical re-heating must be relatively constant over this period of time. Large individual blobs with varying velocities, ejected every few years, would probably produce a more variable temperature structure. Smaller, unresolved internal shocks could, on the other hand, be present so that the cooling time of the plasma can be shorter than derived from the decrease in the mean energy.

5.5. The inner emission component

The most striking feature observed in all observations is the existence of a luminous X-ray emission region close to the driving source(s). The peak of this feature is approximately 0.5-1.0″ offset from L 1551 IRS 5 (R.A.(2000)=04^{h}31^{m}34^s.15, Decl.=18°08′05″.04) towards the south-west. Its luminosity and temperature remains virtually constant within a timespan of about nine years.

Therefore, it seems necessary to review the arguments which prohibit an association of this inner component with one or both of the central driving sources themselves. Essentially, these are (a) the astrometry and (b) the absorption. Concerning (a), the centroid of the inner component is placed at least 0.5″ from the location of radio sources in every of the three available *Chandra* observations. Although this is marginally compatible with our estimated astrometric accuracy, this is unlikely to be caused by a repeated incorrect pointing of the satellite since the centroids (using the photons in the inner $r = 1''$ circle) of the inner component match to within 0.3″ for all observations. As to (b), the interpretation of the scattered light and the non-detection of direct emission places a firm lower limit of $A_V \gg 20$ on the absorption towards IRS 5 (Stocke et al. 1988). This translates into an absorbing column density of $N_H \gg 4 \times 10^{22}$ cm^{-2}, at least three times higher than measured. The measured value, on the other hand, corresponds well to the one estimated for the inner jet from the near-infrared line-ratios and suggests that X-ray and near-infrared emission spatially coincide.

Bally et al. (2003) sketched a possible scenario in which scattered X-rays are responsible for the observed X-ray emission. However, these authors concluded that this option is less likely and we agree with their evaluation. The parameters required for this scattering scenario, e.g., densities of $n \sim 10^9$ cm^{-3}, are not strictly ruled out, but would be exceptional for protostellar jets. Furthermore, the trend in the mean energy also argues against the scattering scenario, because Thomson scattering is not very sensitive to the scattering angle and independent of the wavelength. Dust scattering, on the other hand, is by far not sufficient to explain the observations using the usual conversion factors.

We therefore associate this feature with the apparently stationary [Fe II] emission complex observed by Pyo et al. (2009, 2005, 2002). Their [Fe II] λ1.644 μm data, obtained over a timespan of four years, show an apparently stationary component close to the driving sources. Pyo et al. (2009) already proposed that the inner X-ray emission component is associated with the innermost [Fe II] emission peak, called PHK1 (distance to IRS 5: 1.1″). The total flux in [Fe II] ($\sim 5 \times 10^{-15}$ erg/s/cm^2) is within an order of magnitude comparable with the X-ray flux (0.5-10.0 keV: 4×10^{-15} erg/s/cm^2 or unabsorbed 3×10^{-14} erg/s/cm^2).

The [Fe II] emission at PHK1 is dominated by low velocity material with $v \sim -60 \cdots -150$ km/s (or deprojected $v = -85 \ldots 212$ km/s, for an inclination of $i \approx 45°$). Interestingly, the post-shock velocity of a shock with an initial velocity of v=700 km/s is 175 km/s, i.e., within the range of the low velocity component. Pyo et al. (2002, 2009) noted that the velocity dispersion of the low velocity [Fe II] emission decreases with increasing distance to the driving source, which they interpret as a collimation of the outflow. The large opening angle of the flow close to the driving sources and the shallow opening further downstream support this interpretation. Collimation might also be responsible for the X-ray production and would naturally explain their stationary appearance. Since the high-velocity [Fe II] material appears approximately where the X-ray emission disappears, it is tempting to associate this material with outflowing plasma not as strongly shocked as the X-ray emitting material. However, the total mass-loss derived for the X-ray component is lower than for the optical part of the jet so that it remains unclear whether the "absence" of highly blueshifted emission close to the driving sources is somehow connected to the existence of X-ray material, i.e., if a large fraction of shocked high-velocity material reaches X-ray emitting temperatures.

5.6. The extended or outer emission component

During the 2005 ACIS-I observation, an enhancement of photons two arcseconds downstream from the bulk of the X-ray emission is evident (Favata et al. 2006). We estimated in sect. 4.2.2 that the low number of counts in the corresponding region might be a statistical fluctuation. Nevertheless, it is still possible, if not even physically plausible, that the elongation differences are caused by a transient X-ray emitting knot, possibly comparable with other X-ray emitting knots within HH objects.

Concerning the position of this blob, its 2005 position coincides with one or all emission peaks in the "F"-complex (Bonito et al. 2008). The space velocities measured in this region range from $\sim$ 100 km s^{-1} to 500 km s^{-1} in optical forbidden emission lines (Fridlund et al. 2005). At this distance from the driving source the high-velocity component in [Fe II] becomes dominant over the low-velocity component, and velocities up to 500 km s^{-1} have been measured (Pyo et al. 2005). Furthermore, Pyo et al. (2005) noted that the outer high velocity [Fe II] component might exhibit time-variability at approximately the same time of the appearance of the X-ray knot. However, the F-complex did not change much during this time in its optical appearence (Bonito et al. 2008).

The distance traveled by this hypothetical knot between 2005 and 2009 would be approximately 0.6-3.0″ (100 km s^{-1} ... 500 km s^{-1}). In the corresponding regions zero or one photon are recorded during the 2009 ACIS-S exposure, which is more sensitive than the previous ACIS-I observation at low energies. A maximum of seven photons can be attributed to the 2005 "knot" so that the luminosity of this blob must have decreased during four years. For the interpretation of these phenomena, the cooling time of the X-ray emitting plasma is crucial but unfortunately not known with the required precision.

When the cooling time of the hot plasma is short compared to the travel time to the outer locations of X-ray emission, it is impossible that the material is only heated close to the driving sources and then just cools while it is flowing outwards. Internal shocks are a natural explanation for the re-heating, but the observations require a nearly constant decrease in shock velocity with increasing distance to the driving sources (see the trend in the mean energy, sect. 5.4).

If, on the other hand, the plasma is not significantly re-heated while flowing outwards (no internal shocks), either a variable mass outflow or a statistical fluctuation are responsible for the apparent knot. In any case, a rather constant temperature close to the driving sources is required, which translates to a constant shock velocity for shock heating. In both cases, a shallow opening angle is mandatory and magnetic fields probably suppress heat conduction efficiently. The decrease in plasma temperature along the flow reflects the cooling time of the plasma and explains, why no emission is detected at larger distances from the driving sources.

5.7. Comparison with DG Tau and other jet X-ray sources

The so-called TAX sources (Güdel et al. 2007b), which show spectra composed of two emission components with vastly different absorbing column densities, e.g. from an embedded star and a less embedded jet, show a striking similarity to HH 154. In particular in DG Tau, the majority of the X-ray emission from the jet is also located close to the driving sources *and* appears virtually constant over a timespan of several years. We associate the beehive proplyd and similar COUP sources with this group (Kastner et al. 2005). Equally striking, the position-velocity maps in [Fe II] (e.g. Pyo et al. 2003, 2009), which are available for DG Tau and HH 154, are remarkably similar. Both outflows exhibit a low velocity component close to the star, while the high velocity component is located further downstream. Other jet-driving sources like HL Tauri and RW Aurigae show a slightly different pattern in [Fe II] (Pyo et al. 2006) with the low velocity component at a larger distance from the stellar position.

An obvious difference between the X-ray jets of DG Tau and HH 154 is the different plasma temperature close to the driving source. However, the soft component of the beehive proplyd has approximately the same plasma temperature as HH 154. For DG Tau, the inner X-ray component is only marginally hotter than the outer one, while for HH 154 the outer jet seems to be cooler by a factor of two compared to the emission close to the driving source. Since adiabatic cooling decreases the temperature strongly along the flow, it seems unlikely that the same plasma found close to the driving source is also responsible for the outer X-ray component of the DG Tau X-ray jet and internal shocks cause the high temperatures further outwards.

Stelzer et al. (2009) recently detected the appearance of an X-ray knot after an FU Ori like outburst of Z CMa, i.e., X-ray emission located about 2000 AU from the driving source. This emission is much farther out than in HH 154, which can either indicate that the lifetime of such knots might be relatively long or that strong shocks also occur further outwards in the flow. As in Z CMa the X-ray emission in other HH objects is located further out along the jet. If the correlation of the X-ray region with one of the working surfaces in these outflows is an observational bias, such that X-rays between the knots are less likely to be recognized as associated with the HH object or if it is an intrinsic feature of the X-ray production mechanism is currently not clear.

In summary, two properties make X-rays from the protostellar jets identifiable, (a) a TAX-like spectrum and (b) X-ray emission displaced with respect to the driving source. Strictly speaking, HH 154 belongs to the TAX class of objects and the strong absorption of the driving sources makes the detection of extended emission possible. We speculate that the X-ray morphology of HH 154 also applies to the other TAX sources where the angular resolution is insufficient to resolve all details. As the outflow rate required to produce the observed X-rays in these objects is lower than estimated from the optical emission by a few orders of magnitude, it seems likely that such a high velocity component has escaped detection in other wavelength regimes, but is still powerful enough to lead to the observed X-ray fluxes.

6. Model implications

After the discovery of X-ray emission offset from the driving sources (IRS 5) by Favata et al. (2002) and Bally et al. (2003), a variety of models have been proposed in order to explain this phenomenon. In particular Bally et al. (2003) described an ensemble of possible explanations covering a broad range of possibilities including, e.g., X-rays from the driving source(s) reflected into the line of sight from the outflow cavity. Bonito et al. (2010a) performed detailed magneto-hydrodynamical simulations of a jet with a variable outflow velocity focusing on high velocity shocks within the outflow and the associated X-ray emission. These authors discuss four different scenarios for discussed in sect. 5.6 and depend crucially on the unknown cooling time of the X-ray emitting plasma.

6.1. A jet with random ejection velocity/Internal shocks

This is the model discussed by Bonito et al. (2010a,b). Their simulations can produce an emission complex close to the driving source, when a recently ejected faster blob overtakes a more slowly moving blob (cf. their Fig. 2). In the absence of strong cooling, the proper-motion of such a knot would be detectable with the available high resolution X-ray observations. Concerning the inner, apparently stationary source, the models of Bonito et al. (2010b) predict that the most probable position of a shock is close to the driving sources.

The virtually constant X-ray luminosity and the relation to the constant [Fe II] emission argues against a strong variation of the shock velocity or location. One solution for these discrepancies is a relatively regularly modulated jet so that a constant luminosity might be mimicked by the superposition of a roughly constant number of smaller shocks formed close to the driving source. The trend in the mean energy would then reflect the cooling of these smaller individual blobs, while they travel along the outflow (e.g., see also the sub-radial blobs modeled by Yirak et al. 2009). Another possibility is that variations in the shock properties are hidden by the low photon numbers and the inner X-ray emission is caused by larger knots shocked close to the driving source. The constant appearance would then not reflect a constant outflow but would rather be a chance coincidence.

In this model the absence of X-ray emission farther downstream would be explained either by a lower density or a low temperature of the plasma inhibiting its detection. The opening angle of the optical jet is roughly consistent with this picture. It requires, however, that strong shocks at larger distances from the driving source are less probable than close to the driving sources, which is true for the models of Bonito et al. (2010a). In case of a short cooling time the decrease of the plasma temperature reflects a decreasing shock velocity with increasing distance to the driving sources, which would provide another explanation for the non-detection of X-ray emission farther downstream. In any case, the observations clearly show that the heating to X-ray temperatures is a function of the position along the flow.

6.2. Base/collimation shock

Guided by the first *Chandra* observation, Bally et al. (2003) proposed that some kind of stationary base-shock can explain the observed X-rays, either independently for each driving source or at the envelope of both sources. In these scenarios, the magnetic fields can collimate the outflow and can also support the jet against the thermodynamic pressure of the hot X-ray emitting plasma.

This scenario requires lower velocities than the internal shock model, but still higher than detected in available spectra. The "deflection" angle might be relatively large ($\sim 45°$) as the opening angle close to the driving sources might also be large so that flow velocities of 10^3 km s^{-1} suffice for the X-ray production. Also, the concentration of the X-rays within a rather small volume close to the driving sources and the virtually constant X-ray luminosity are a natural consequence of this scenario. The base-shock scenario does not inhibit jet mass flux variations and is consistent with the observations as long as the amplitude of these variations is small enough. For sufficient clumpiness and blob ejection cadence, the base-shock model and the internal shock model become indistinguishable and share the possibility for small amplitude time variability.

Concerning the location of the base-shock, it seems pleasing to attribute the brightest X-ray spot to the location of the base-shock consistent with the [Fe ɪɪ] observations of Pyo et al. (2009). However, the increasing absorbing column, which seems to cause the hardening of the photons in the innermost part of the flow, can absorb the soft X-rays closer to the driving sources. Thus, it is possible that the true location of the shock region is hidden behind a larger absorbing column and located closer to the driving source.

The trend in the mean energy is also a natural outcome of this scenario, when the plasma is heated to X-ray emitting temperatures close to the driving sources and cools while flowing outwards. Adiabatic cooling, providing an upper limit on the cooling time, is approximately consistent with the observed trend in the mean energy.

6.3. Precessing jet

Jet precession seems to be required for some of the observed jets (e.g. HH 34 Masciadri et al. 2002). The precession times are usually rather long ($\gtrsim 10^3$ yrs), therefore, the change in outflow direction for HH 154 would be small between the 2001 and the 2009 *Chandra* observations. Still, some kind of a drilling effect might be present. A constant flow hitting different parts of the envelope would lead to a constant appearance of the inner emission component. As the opening angle ($\sim 90°$) close to the source is probably large compared to the expected precession angle, we regard it as less likely that the direction change of the outflow is responsible for the X-ray emission.

6.4. Stellar wind

The solar wind has roughly the temperature and velocity observed for HH 154's X-ray emission. We can imagine that during the early stellar evolution the outflow rates of stellar winds are much higher than for the present-day Sun and that the same process leading to the collimation of the slower outflow components collimates the stellar wind. A stellar wind might be important for the angular momentum problem. but cannot be responsible for outflow rates above 10^{-9} $M_\odot$/year due to the resulting excessive X-ray emission (Decampli 1981; Matt & Pudritz 2008). However, the outflow-rate required for the observed X-ray emission is orders of magnitudes lower and Gómez de Castro & Verdugo (2007) found evidence for a stellar driven wind for RY Tau. These authors suggest that the superposition of many individual small-scale outflows from the stellar surface leads to observed morphology of the FUV lines. Therefore, a stellar wind, while not responsible for the main outflow, might provide the required high temperature plasma close to the driving source. This stellar wind would not require high outflow velocities for the shock heating since it is already of approximately the correct temperature when launched. However, the association of X-ray emission with shocked material at other wavelengths makes this explanation less likely but would be another possibility explaining the constant appearance.

7. Summary

Our new, third epoch *Chandra* observation clearly shows that the process responsible for the X-ray emission in HH 154 is constant over at least one decade. The position, the luminosity and temperature of the X-ray emission are virtually the same in all observations. Whether differences between the observations are statistical fluctuations or intrinsic differences in the flow cannot be definitely decided due to the low count statistics. From the trend of the mean energy along the jet axis, we show that the plasma is cooler at larger distances from the driving source.

We discus several models and find that a standing shock most naturally explains the observed morphology given the constant total X-ray luminosity. The location of the X-ray emission, where the outflow is likely collimated, and its stationary appearance argue for this model. Depending on the details of the plasma cooling, the trend in the mean energy can be naturally explained in this model. The features of the X-ray emission can also be explained in terms of a pulsed jet, where internal shocks cause an apparent stationary X-ray source as the most probable location of an X-ray emitting shock is close to the driving source. The trend in the mean energy might then reflect lower shock velocities or the cooling of the plasma depending on the detailed cooling times of the X-ray emitting plasma. The existence of knots within protostellar jets is usually attributed to time-variable outflows, therefore, such a model is attractive, but it requires a rather regularly modulated flow, since the position, the temperature and the luminosity appear constant. Variability at larger distances from the driving sources might be present and can be explained either by local shocks or variations of the mass loss rate.

A comparison of our new results for HH 154 with other X-ray emitting jets, in particular with DG Tau, the only nearby jet X-ray source where multi-epoch observations are available, shows that soft X-ray photons close to the driving source are not unique to HH 154. Therefore, the necessary heating apparently takes place very close to the driving source within the outflow. With an increasing number of X-ray observations it becomes increasingly clear that the origin of the X-rays is tightly connected to the flow properties within the innermost few 10 AU, either due to inhomogeneities in the outflow or by the collimation process.

New ensitive X-ray observations of HH 154 with a higher cadence are required to decide whether variations on shorter time scales are present and could therefore discriminate between the base-shock and the internal shock model.

Acknowledgements. This work has made use of data obtained by *Chandra*, from the *Chandra* data archive and from the XMM-Newton data archive. P.C.S. acknowledges support from the DLR under grant 50OR0703. H.M.G. acknowledges support from Chandra under grant GO6-7017X This research has made use of the SIMBAD database, operated at CDS, Strasbourg, France

References

Anders, E. & Grevesse, N. 1989, Geochim. Cosmochim. Acta, 53, 197
Arnaud, K. A. 1996, in Astronomical Society of the Pacific Conference Series, Vol. 101, Astronomical Data Analysis Software and Systems V, ed. G. H. Jacoby & J. Barnes, 17–+
Bacciotti, F., Mundt, R., Ray, T. P., et al. 2000, ApJ, 537, L49
Bally, J., Feigelson, E., & Reipurth, B. 2003, ApJ, 584, 843
Bonito, R., Fridlund, C. V. M., Favata, F., et al. 2008, A&A, 484, 389
Bonito, R., Orlando, S., Miceli, M., et al. 2010a, ArXiv e-prints
Bonito, R., Orlando, S., Peres, G., et al. 2010b, A&A, 511, A42+
Bonito, R., Orlando, S., Peres, G., Favata, F., & Rosner, R. 2004, A&A, 424, L1
Borkowski, K. J., Shull, J. M., & McKee, C. F. 1989, ApJ, 336, 979
Cabrit, S. 2007, in Lecture Notes in Physics, Berlin Springer Verlag, Vol. 723, Lecture Notes in Physics, Berlin Springer Verlag, ed. J. Ferreira, C. Dougados, & E. Whelan, 21–+
Campbell, B., Persson, S. E., Strom, S. E., & Grasdalen, G. L. 1988, AJ, 95, 1173
Cho, J., Lazarian, A., Honein, A., et al. 2003, ApJ, 589, L77
Decampli, W. M. 1981, ApJ, 244, 124
Dere, K. P., Landi, E., Mason, H. E., Monsignori Fossi, B. C., & Young, P. R. 1997, A&AS, 125, 149
Dere, K. P., Landi, E., Young, P. R., et al. 2009, A&A, 498, 915
Devine, D., Reipurth, B., & Bally, J. 1999, AJ, 118, 972
Favata, F., Bonito, R., Micela, G., et al. 2006, A&A, 450, L17
Favata, F., Fridlund, C. V. M., Micela, G., Sciortino, S., & Kaas, A. A. 2002, A&A, 386, 204
Ferreira, J., Dougados, C., & Cabrit, S. 2006, A&A, 453, 785
Fridlund, C. V. M., Bergman, P., White, G. J., Pilbratt, G. L., & Tauber, J. A. 2002, A&A, 382, 573
Fridlund, C. V. M. & Liseau, R. 1998, ApJ, 499, L75+
Fridlund, C. V. M., Liseau, R., Djupvik, A. A., et al. 2005, A&A, 436, 983
Gehrels, N. 1986, ApJ, 303, 336
Gómez de Castro, A. I. & Verdugo, E. 2007, ApJ, 654, L91
Güdel, M., Briggs, K. R., Arzner, K., et al. 2007a, A&A, 468, 353
Güdel, M., Skinner, S. L., Audard, M., Briggs, K. R., & Cabrit, S. 2008, A&A, 478, 797
Güdel, M., Telleschi, A., Audard, M., et al. 2007b, A&A, 468, 515
Günther, H. M., Matt, S. P., & Li, Z.-Y. 2009, A&A, 493, 579
Hartigan, P., Frank, A., Varniére, P., & Blackman, E. G. 2007, ApJ, 661, 910
Hartigan, P., Morse, J., & Bally, J. 2000, AJ, 120, 1436
Hayashi, M. & Pyo, T. 2009, ApJ, 694, 582
Itoh, Y., Kaifu, N., Hayashi, M., et al. 2000, PASJ, 52, 81
Kastner, J. H., Franz, G., Grosso, N., et al. 2005, ApJS, 160, 511
Lazarian, A. 2006, ApJ, 645, L25
Liseau, R., Fridlund, C. V. M., & Larsson, B. 2005, ApJ, 619, 959
Lynds, B. T. 1962, ApJS, 7, 1
Masciadri, E., de Gouveia Dal Pino, E. M., Raga, A. C., & Noriega-Crespo, A. 2002, ApJ, 580, 950
Matt, S. & Pudritz, R. 2008, in Astronomical Society of the Pacific Conference Series, Vol. 384, 14th Cambridge Workshop on Cool Stars, Stellar Systems, and the Sun, ed. G. van Belle, 339–+
Melnikov, S. Y., Eislöffel, J., Bacciotti, F., Woitas, J., & Ray, T. P. 2009, A&A, 506, 763
Narayan, R. & Medvedev, M. V. 2001, ApJ, 562, L129
Orlando, S., Peres, G., Reale, F., et al. 2005, A&A, 444, 505
Pravdo, S. H., Feigelson, E. D., Garmire, G., et al. 2001, Nature, 413, 708
Pyo, T., Hayashi, M., Kobayashi, N., et al. 2002, ApJ, 570, 724
Pyo, T., Hayashi, M., Kobayashi, N., Terada, H., & Tokunaga, A. T. 2009, ApJ, 694, 654
Pyo, T., Hayashi, M., Kobayashi, N., et al. 2006, ApJ, 649, 836
Pyo, T., Hayashi, M., Kobayashi, N., et al. 2005, ApJ, 618, 817
Pyo, T., Kobayashi, N., Hayashi, M., et al. 2003, ApJ, 590, 340
Raga, A. C., Noriega-Crespo, A., & Velázquez, P. F. 2002, ApJ, 576, L149
Raga, A. C., Riera, A., & González-Gómez, D. I. 2010, A&A, 517, A20+
Rodríguez, L. F., D'Alessio, P., Wilner, D. J., et al. 1998, Nature, 395, 355
Rodríguez, L. F., Porras, A., Claussen, M. J., et al. 2003, ApJ, 586, L137
Schneider, P. C. & Schmitt, J. H. M. M. 2008, A&A, 488, L13
Skrutskie, M. F., Cutri, R. M., Stiening, R., et al. 2006, AJ, 131, 1163
Smith, R. K., Brickhouse, N. S., Liedahl, D. A., & Raymond, J. C. 2001, ApJ, 556, L91
Snell, R. L., Bally, J., Strom, S. E., & Strom, K. M. 1985, ApJ, 290, 587
Snell, R. L., Loren, R. B., & Plambeck, R. L. 1980, ApJ, 239, L17
Spitzer, L. 1962, Physics of Fully Ionized Gases, ed. Spitzer, L.
Stelzer, B., Hubrig, S., Orlando, S., et al. 2009, A&A, 499, 529
Stocke, J. T., Hartigan, P. M., Strom, S. E., et al. 1988, ApJS, 68, 229
Strom, K. M., Strom, S. E., & Vrba, F. J. 1976, AJ, 81, 320
Vuong, M. H., Montmerle, T., Grosso, N., et al. 2003, A&A, 408, 581
Yirak, K., Frank, A., Cunningham, A. J., & Mitran, S. 2009, ApJ, 695, 999

8. The nature of the soft X-ray source in DG Tauri

P.C. Schneider, J. H. M. M. Schmitt
Astronomy & Astrophysics, 488, L13 (2008)

A&A 488, L13–L16 (2008)
DOI: 10.1051/0004-6361:200810261

Astronomy & Astrophysics

LETTER TO THE EDITOR

The nature of the soft X-ray source in DG Tauri

P. C. Schneider and J. H. M. M. Schmitt

Hamburger Sternwarte, Gojenbergsweg 112, 21029 Hamburg, Germany
e-mail: [cschneider;jschmitt]@hs.uni-hamburg.de

Received 26 May 2008 / Accepted 23 June 2008

ABSTRACT

The classical T Tauri star DG Tau shows all typical signatures of X-ray activity and, in particular, harbors a resolved X-ray jet. DG Tau's jet is one of the most well studied jets of young stellar objects, having been observed for more than 25 years by a variety of instruments. We demonstrate that its soft and hard X-ray components are separated spatially by approximately 0.2 arcsec by deriving the spatial offset between both components from the event centroids of the soft and hard photons utilizing the intrinsic energy-resolution of the *Chandra* ACIS-S detector. We also demonstrate that this offset is physical and cannot be attributed to an instrumental origin or to low counting statistics. Furthermore, the location of the derived soft X-ray emission peak coincides with emission peaks observed for optical emission lines, suggesting that both soft X-rays and optical emission have the same physical origin.

Key words. stars: individual: DG Tauri – stars: winds, outflows – X-rays: stars – stars: pre-main sequence

1. Introduction

The evolution of protostars to young stellar objects (YSOs) is accompanied by accretion from a circumstellar envelope and disk as well as the loss of angular momentum by a substantial, often jet-like mass-outflow perpendicular to the disk (e.g. Königl & Pudritz 2000); however, neither the launching mechanism nor the collimation process have been unambiguously identified. The jet of DG Tau is among the most well studied jets of YSOs, and these observations have placed tight constraints on the nature of the relevant processes, e.g. the detection of rotation in the outer regions of the DG Tau jet (Bacciotti et al. 2002) constrained the launch radius of the outflow.

DG Tau is a classical T Tauri star (CTTS), whose basic properties were summarized by Güdel et al. (2007). Its mass-outflow (a few 10^{-7} $M_\odot$ yr^{-1} extending out to $\sim 10''$ $\approx$ 2300 AU) was first resolved by Mundt & Fried (1983). Most observations of DG Tau's outflow were carried out in forbidden emission line regions (FELR), which trace material at temperatures of $\sim 10^4$ K and densities below $\sim 10^7$ cm^{-3}. These studies indicated that at distances larger than $\sim 0.5''$ from the central source the forbidden line emission is concentrated in individual blobs moving at velocities of $\sim$300 km s^{-1} (projected $\sim 0.3''$ yr^{-1}) approximately along the jet axis (Pyo et al. 2003). The structure of the innermost region of the DG Tau system is subject to permanent variations. Several studies revealed evidence for material of different speeds and morphology (e.g. Kepner et al. 1993; Bacciotti et al. 2000; Takami et al. 2002), indicating an evolution on time scales of years. The material in the vicinity of the star is probably denser than in the more distant jet component (Solf & Böhm 1993). In particular, the jet shows an onion-like structure where the higher velocity material is embedded in more slowly moving material (Bacciotti et al. 2002). The favored heating mechanism for the jet emission is internal shocks, heating up the material to temperatures of $\sim 10^4$ K (Lavalley-Fouquet et al. 2000).

As many (if not all) CTTS, DG Tau is an X-ray source, first detected by Feigelson & Decampli (1981). From the X-ray point of view the source is unusual in two aspects. First, DG Tau is the only stellar X-ray source harboring a resolved X-ray jet (Güdel et al. 2008), which can be traced out to a distance of $\sim 5''$ from the central source with a luminosity of about 10% of the central soft X-ray component. Second, the X-ray properties of DG Tau resemble that of the class of "two-absorber-X-ray (TAX) sources" (Güdel et al. 2007, 2008). X-ray spectra of TAX sources are basically the sum of two thermal components, differing not only in mean temperature but – in contrast to most other X-ray spectra – also in absorbing column density. In DG Tau, the emission regions of the soft and the hard components appear to be disjoint spatially. In an *XMM-Newton* observation, Güdel et al. (2007) found an increase in the hard component's count rate during a flare, while the soft component remained constant; they proposed therefore, supported by the spectral properties of the soft component, an interpretation of the soft component as internal shocks in a jet close to the star. Motivated by the indications that the soft X-ray component in DG Tau might be spatially detached from the hard X-ray component, we performed a detailed position analysis of both components utilizing the superb angular resolution of the *Chandra* telescope.

2. Observations, data processing, and data analysis

The available *Chandra* data of DG Tau cover a total exposure time of 90 ks split into 4 individual observations performed between 2004 and 2006 (see Table 1 of Güdel et al. 2008, for a summary). The details of these observations were presented by Güdel et al. (2008). Our data reduction was completed using CIAO Version 4.0, along the lines of the *Chandra* analysis threads with the aim to derive accurate source positions. We define a soft (0.3–1.1 keV) and a hard (1.7–7.0 keV) spectral component and list their relevant properties in Cols. 3 and 4 of Table 1; because of the TAX property of DG Tau, the mutual contamination of the components is quite small.

The *Chandra*-calibration team states a $0.1''(1\sigma)$ accuracy for relative positions on the ACIS S3 detector [1]. This implies that an

[1] http://cxc.harvard.edu/cal/docs/cal_present_status.html#rel_spat_pos

Table 1. Offsets for the individual observations.

Obs-ID	Offaxis (arcmin)	Soft photons	Hard photons	Offset (arcsec)	Position angle (degree)
4487	1.43	138	191	0.23	225
6409	0.55	67	112	0.20	215
7247	0.55	65	49	0.13	191
7246	0.55	133	187	0.20	215

offset between the central source and X-ray emission arising in the inner part of the optically resolved jet is – at least in principle – measurable, given the fact that the stellar emission component is thought to be strongly absorbed at soft X-ray energies below 1 keV. We, therefore, derived individual positions for the above defined soft and hard components and calculated their respective centroids with sub-pixel resolution. The most precise determination of source positions is complicated by the fact that the superb point-spread function of the *Chandra* mirrors is slightly undersampled by the ACIS-S detector. To compensate for the effect of this undersampling, various strategies, such as sub-pixel event repositioning (Li et al. 2004), can be pursued during the data processing and data analysis. During pipeline processing, the nominal photon positions are randomly distributed within a given detector pixel (±0.25″). Alternatively, no randomization (cf., Feigelson et al. 2002) or re-randomization schemes can be applied. As a conservative approach we used the archival data with standard randomization to minimize possible aliasing effects, and verified that our results (and our conclusions) do not depend on the type of the randomization chosen.

To determine source positions, we experimented with the standard source-detection tools `wavdetect` and `celldetect`. The `celldetect` algorithm uses different photons (the "search region" is always a box in the projected image which is not necessarily centered on the centroid) and the `wavdetect` algorithm reverts to binned data, thus both approaches are not optimized to find the most accurate source position. Therefore we developed our own iterative source position determination algorithm. Starting with an approximate "by eye" position, we extracted all photons within a 0.75″ radius around this position to determine a new centroid; with this new position photons were then reextracted and the entire process continued until convergence. This method should operate well for a symmetric point response function, which applies in the central FOV. We note that the soft component's size might actually deviate from that expected for a point-like source by approximately 0.5″, while a size of ≥1″ can be excluded at above the 90% confidence level. However, the signal-to-noise (SNR) of the available data does not enable statistically robust results to be derived.

The "very faint"-mode of the observations leads to a low probability of finding a background photon in our search region, which is below 30% for the longer exposures. A single photon shifts the derived source position by less than 0.03″, so that any background is essentially negligible in our analysis.

During the analysis, we kept the 4 individual exposures separate. Merging the individual exposures can degrade the spatial resolution because the absolute astrometric accuracy of *Chandra* (∼0.4″(1σ)) is worse than its relative accuracy. To account for this effect, we reprojected the individual exposures so that the centroid of the hard component of DG Tau was aligned in all observations. We coadded the images to be able to derive higher signal-to-noise data as a cross-check; we are aware, however, that the positions of the soft X-ray emission might not be constant throughout the observation period of almost two years.

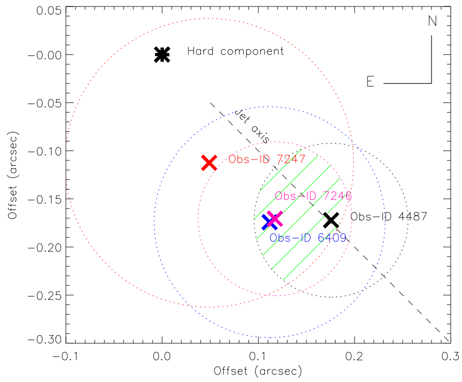

Fig. 1. Relative spatial offset of the soft X-ray component. The hard component is centered at (0, 0). The circles indicate the 90% confidence interval taken from Table 2 and Obs-ID 3730. The shaded area is included in the 90% confidence ranges of all observations.

3. Results

3.1. Soft and hard source positions

In Fig. 1, we show the computed separations of the soft and the hard X-ray centroid for all four observations of DG Tau and their estimated error radii. All derived positions were shifted in order to align the position of the hard component. As is clear from Fig. 1, all observations exhibit a (sub-pixel) offset between the soft and the hard X-ray components. For the three well exposed observations (cf., Table 1), we find similar offsets with a separation of ∼0.2″, while the fourth observation (Obs-ID 7247) shows a smaller offset, but in a similar direction, and - considering the low count statistics – still compatible with the other observations. A total offset of 0.21″ is also obtained if the centroids in the coadded event-files are considered, which equals the best-fit value derived by using all individual observations with the errors estimated in Sect. 3.3. The position angles of the measured DG Tau offsets yield a best fit offset angle of ∼218°, which compares well with the position angle of ∼225° for the jet orientation in the optical (e.g. Eislöffel & Mundt 1998).

3.2. Is it instrumental?

To investigate whether the observed offset between soft and hard source positions can be attributed to instrumental effects, we retrieved a number of observations from the *Chandra* archive taken with ACIS-S3 in the VFAINT-mode (Obs-ID 3730 is FAINT-mode). The retrieved observations are listed in Table 3. For these targets, we then performed the same analysis as for the DG Tau data and computed offsets between the soft and hard source positions. In Fig. 2, we show the derived offset statistics, where we distinguish between the "good" data sample (off-axis angle <1.5′ and >50 cts) and the "poor" data sample (off-axis angle <3′ and >25 cts); we note that in this nomenclature our DG Tau is "good" data. Figure 2 clearly shows that DG Tau's offset is extremely unusual, and in fact none of the investigated data sets and in particular none of the "good" data sets shows an offset comparable to that observed in DG Tau.

We investigated the energy dependence of the point response function by calculating the centroids of precomputed synthetic PSF-images provided by the CIAO-tool `mkpsf` for the DG Tau source position; we found that the centroid position changes by less than 1/100 pixel between the images for the hardest (7 keV) and the softest photons (0.3 keV), even for Obs-ID 4487, which

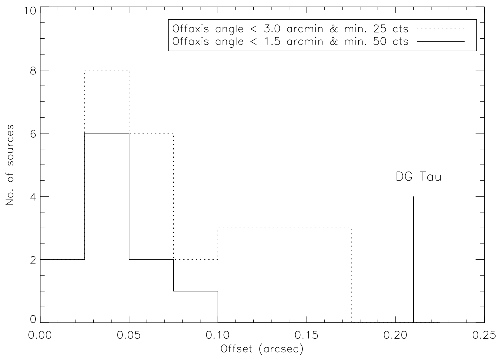

Fig. 2. Statistics of the comparison observations.

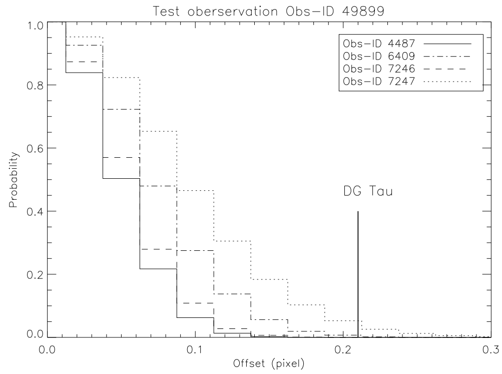

Fig. 3. Distribution of distances between the soft and the hard X-ray component for point-like sources with simulated count statistics matching the circumstances of the DG Tau observations.

Table 2. Probabilities derived from the comparison observations. The 90% limit refers to the seperation that only 10% of the trials exceed and the probability is the value for finding the measured or a larger offset.

Comparison observation	DG Tau observation	$d <$ for 90%	Probability %
3730	4487	0.08″	<0.1
	6409	0.12″	0.4
	7246	0.08″	<0.1
	7247	0.15″	21.2
4470	4487	0.11″	<0.1
	6409	0.15″	1.2
	7246	0.12″	<0.1
	7247	0.19″	32.3

has the largest off-axes angle. Performing Marx 4.3 simulations[2] that include a model of the individual mirror shells strengthened this finding. Then we further restricted the energy ranges of the test-exposures with a high count-statistics such as Obs-ID 3730, 4470, 49899, and 626 to the outer edges of the energy bands, e.g. 0.3–0.7 keV and 3.0–7.0 keV, to check whether the offset becomes larger. A positive result would imply that the centroid position is dependent on the energy range used. However, the measured separations differ only slightly from the previous results, and remain, in any case, far smaller than our DG Tau offsets. Finally, we split the hard X-ray component of DG Tau, which represents the coronal emission in our interpretation, into two groups; the offsets between the mean positions of theses two groups are consistent within ~0.1″ margin of error, which increased when the hard component is divided into two. The position angle also differs from that of the separation of the hard and the soft component. In summary, we conclude that no evidence supports the idea that the measured offset can be attributed to an instrumental effect.

3.3. Is it statistical?

We investigated the statistical errors in the soft and hard photon centroid positions. To assess the statistical scatter in the source positions, we artificially reduced the number of photons in the high count statistics test observations (cf., Table 3) by selecting randomly the same number of "source" photons as observed in the individual DG Tau observations in the desired energy range, and computed the source centroid positions and their offsets. An example of the simulated offset distribution (using 10^4 realizations) is shown in Fig. 3 and the relevant properties of the distributions are summarized in Table 2. As is obvious from Fig. 3 and the numbers in Table 2, statistical fluctuations are an extremely unlikely cause of the observed DG Tau offset.

3.4. Offset significance and uncertainties for DG Tau

Neither the studied comparison sources nor our simulations show an offset between the soft and the hard photon centroids sufficiently large to explain the observed offsets in DG Tau. The probability of measuring an offset larger than 0.2″ is below ~0.01 for the observations of longer exposure times (Obs-OD 4487, 6409, 7246), if both sources are at the same position. We note that the measured position angle between soft and hard position correlates with the optically known jet-direction. Using an estimate of the measured position angle distribution of ±30° about the jet-direction (cf., Table 1), the probability that the measured position angle is located in the same range for all observations is only 7.7×10^{-4}, assuming that they are distributed uniformly. Thus, formally, we estimate a probability of less than 10^{-8} that the observed offset distribution is obtained by chance and therefore conclude that any systematic errors are far smaller than the observed offsets and that the errors in our measurements are dominated by counting statistics.

4. Discussion

By considering the measured offset of 0.2″ between the soft and the hard X-ray centroid position as physical, we can convert this offset into a physical distance of 45 AU from the central source, assuming a distance of 140 pc and a disk inclination of 38° (Eislöffel & Mundt 1998). This distance is an order of magnitude larger than reasonable launching regions of the jet (~1 AU, Anderson et al. 2003), and our results therefore favor strongly the interpretation that the X-ray emission observed close to the star is originating from internal shocks of the jet, as proposed by Güdel et al. (2007). Internal shocks are incidentally also the preferred heating mechanism for the optically observed FELRs. With this interpretation, the total X-ray luminosity of the jet is an order of magnitude higher than that of the *Chandra*-resolved part of the jet (Güdel et al. 2008), although even then its luminosity is far smaller than the optical jet luminosity; for example, Lavalley-Fouquet et al. (2000) derived a luminosity, for the first emission peak of the [O I]-line, of $1.1 \times 10^{-4}\ L_{\odot}$, which is a factor of ~40 higher than the energy-loss by X-ray emission, suggesting that only a small amount of the outflowing material reaches X-ray temperatures. We model the X-ray jet by a cylinder of radius r and1.5 height d; the base of the cylinder is located

[2] http://space.mit.edu/ASC/MARX/

Table 3. Comparison observations.

Obs-ID	Source	Off-axis (′)	Min. counts	Offset (″)
4470	Gl 569 A	0.5	1565	0.03
49899	Prox Cen	0.6	1040	0.02
971	TWA-5	0.3	568	0.03
3730	GJ 3275	0.6	492	0.02
6416	NGC 1977 311	2.9	436	0.04
626	HD 113703 B	0.7	400	0.05
6417	NGC 1977 311	2.8	205	0.07
4476	GJ1245 A	0.5	118	0.03
626	HD 113703 C	0.7	99	0.08
4489	2MASS 05352360-0628244	2.63	94	0.11
6417	CSV 6218	2.8	88	0.17
4510	NGC6791 KU B16	0.9	86	0.05
6416	V* V372 Ori	0.7	81	0.04
4476	GJ1245 B	0.5	63	0.04
4485	1WGA J2203.9-5647	1.7	56	0.16
5427	HD 179949	0.3	49	0.08
627	HD 129791B	1.7	45	0.13
4510	NGC6791 SBG 9315	1.4	44	0.11
6121	HD 179949	0.6	43	0.06
7247	2MASSs J0426573+260628	1.7	41	0.07
630	CXOSEXSI J175823.5+663950	1.5	36	0.16
6417	JW 94	1.5	34	0.06
6120	HD 179949	0.3	31	0.04
4488	FS Tau	0.8	31	0.14
4487	2MASSs J0426573+260628	1.9	31	0.13
6417	V* V372 Ori	0.8	29	0.12
6416	Parenago 1606	1.4	25	0.08

at the shock region, where the material is heated to some temperature T, and the shocked material flows through this cylinder with some post-shock velocity v. We assume that the shocked material cools predominantly by radiation with a cooling time τ_c given by $\tau_c = 3k_BT/(n\Lambda(T))$, where n is the plasma density, T the (post-shock) temperature, $\Lambda(T)$ the cooling function, and k_B Boltzmann's constant. The cooling distance d, i.e., the height of the cylinder, is then given by $d = \tau_c \cdot v = 3k_BTv/(n \cdot \Lambda(T))$. We further know the total emission measure EM of the X-ray emitting plasma and write

$$EM = f \cdot n^2 \cdot A \cdot d = 3f \cdot n \cdot \pi r^2 \cdot v k_B T/\Lambda(T), \quad (1)$$

where f denotes an unknown filling factor of the hot plasma. The mass outflow rate $\dot{M}_{X-ray}$ of the X-ray emitting plasma can be computed from

$$\dot{M}_{X-ray} = m_H\ f\ n \cdot \pi r^2 \cdot v = m_H \Lambda(T) EM/(3k_BT), \quad (2)$$

i.e. the mass outflow rate of the X-ray emitting material is only determined by the observed quantities T and EM. Our spectral fit provides a mean temperature of $T \sim 3.4$ MK for the shocked plasma and $EM \sim 3.5 \times 10^{52}$ cm^{-3} (APEC-models, metallicity at 0.3 solar) compatible with the values given by Güdel et al. (2008). With these numbers we find an outflow rate of $1.3 \times 10^{-11}\ M_\odot$/yr using $\Lambda(T) \approx 2 \times 10^{-23}$ erg cm^{3}s^{-1}. This value is indeed orders of magnitude smaller than the outflow rate of the high velocity material only ($4 \times 10^{-9}\ M_\odot$/yr, Lavalley-Fouquet et al. 2000). Are such values physically reasonable? We note that the soft X-ray component is more or less point-like if we disregard for the time being the extended jet component described by Güdel et al. (2008). Given the distance of 140 pc towards DG Tau, this implies that the region d_{max} has the approximate size of 112 AU (one ACIS pixel). If we estimate the outflow speed of the shocked material to be approximately 300 km s^{-1}, which is on the one hand the speed of the high-velocity material measured in FELRs and on the other hand approximately the speed required to produce the observed soft X-ray temperature by means of the strong shock formula (the optically observed shocks have speeds of only up to 100 km s^{-1}, Lavalley-Fouquet et al. 2000) we can then derive $n > n_{min} = 3k_BTv/(d_{max} \cdot \Lambda(T)) = 1.3 \times 10^6$ cm^{-3}. Using these values of n_{min} and d_{max} to calculate the emission measure, we estimate the effective outflow cross sectional area $f\pi r^2 \approx 1 \times 10^{25}$ cm^2 or $f\pi r^2 \approx 6 \times 10^{-2}$ AU^2. The launch and collimation distance of the jet in DG Tau is believed usually to be approximately 1 AU. Therefore, the filling factor of the X-ray emitting material must be small and we envisage a scenario of hot X-ray plasma with a small filling factor, immersed in cooler material with a far larger filling factor. A fraction of the shocked material is clearly observed radiating in the resolved jet at a distance of 5″ to DG Tau at essentially the same X-ray temperature as the "inner jet". The cooling time of this material may be sufficiently large to enable the material to move the distance required; this would descrease the density and the filling factor by one and two orders of magnitude, respectively, in comparison to the values above. We prefer, however, an interpretation in which the resolved jet is possibly "re-shocked" material. At any rate, only a minor fraction of the outflowing material in the "inner jet" experiences shocks at $\sim$300 km s^{-1} or more, while the densities and mean velocities of the hot ($T \sim 3 \times 10^6$ K) and the cool ($T \sim 10^4$ K) material are similar to within factors of a few.

5. Summary

Our detailed analysis of the spatial distribution of the X-ray emission of DG Tau shows that the soft and the hard X-ray emission can be spatially separated, which is consistent with the suggestion of Güdel et al. (2007). The measured separation is 0.21″ ≈ 48 AU and the X-ray jet of DG Tau is therefore not only located at large distances (up to 5″) but also close to the stellar emission. If we identify the hard X-ray component with coronal emission from the stellar surface, which is suggested by its stronger absorption compared to the soft component, then the position of the soft X-rays coincides with a region in the DG Tau jet where enhanced emission in the FELRs is observed. Only a small fraction of the total mass-loss and the radiative loss is needed to explain the observed X-rays, and therefore only a small fraction of the outflowing material appears to reach X-ray emitting temperatures. Unfortunately, the available observations do not allow any detailed studies of the spectral features of the soft X-ray component, and therefore a grating observation of DG Tau would provide deeper insights into the true nature of the soft X-ray component's emission process.

Acknowledgements. This work has made use of data obtained from the *Chandra* data archive. P.C.S. acknowledges support from the DLR under grant 50OR703.

References

Anderson, J. M., Li, Z.-Y., Krasnopolsky, R., & Blandford, R. D. 2003, ApJ, 590, L107
Bacciotti, F., Mundt, R., Ray, T. P., et al. 2000, ApJ, 537, L49
Bacciotti, F., Ray, T. P., Mundt, R., Eislöffel, J., & Solf, J. 2002, ApJ, 576, 222
Eislöffel, J., & Mundt, R. 1998, AJ, 115, 1554
Feigelson, E. D., & Decampli, W. M. 1981, ApJ, 243, L89
Feigelson, E. D., Broos, P., Gaffney, III, J. A., et al. 2002, ApJ, 574, 258
Güdel, M., Telleschi, A., Audard, M., et al. 2007, A&A, 468, 515
Güdel, M., Skinner, S. L., Audard, M., Briggs, K. R., & Cabrit, S. 2008, A&A, 478, 797
Kepner, J., Hartigan, P., Yang, C., & Strom, S. 1993, ApJ, 415, L119
Königl, A., & Pudritz, R. E. 2000, Protostars and Planets IV, 759
Lavalley-Fouquet, C., Cabrit, S., & Dougados, C. 2000, A&A, 356, L41
Li, J., Kastner, J. H., Prigozhin, G. Y., et al. 2004, ApJ, 610, 1204
Mundt, R., & Fried, J. W. 1983, ApJ, 274, L83
Pyo, T.-S., Kobayashi, N., Hayashi, M., et al. 2003, ApJ, 590, 340
Solf, J., & Böhm, K. H. 1993, ApJ, 410, L31
Takami, M., Chrysostomou, A., Bailey, J., et al. 2002, ApJ, 568, L53

9. X-raying the AU Microscopii debris disk

P.C. Schneider, J. H. M. M. Schmitt
Astronomy & Astrophysics, 516, A8 (2010)

A&A 516, A8 (2010)
DOI: 10.1051/0004-6361/201014038

Astronomy & Astrophysics

X-raying the AU Microscopii debris disk

P. C. Schneider and J. H. M. M. Schmitt

Hamburger Sternwarte, Universität Hamburg, Gojenbergsweg 112, 21029 Hamburg, Germany
e-mail: christian.schneider@hs.uni-hamburg.de

Received 11 January 2010 / Accepted 24 March 2010

ABSTRACT

AU Mic is a young, nearby X-ray active M-dwarf with an edge-on debris disk. Debris disk are the successors to the gaseous disks usually surrounding pre-main sequence stars which form after the first few Myrs of their host stars' lifetime, when – presumably – also the planet formation takes place. Since X-ray transmission spectroscopy is sensitive to the chemical composition of the absorber, features in the stellar spectrum of AU Mic caused by its debris disk can in principle be detected. The upper limits we derive from our high resolution *Chandra* LETGS X-ray spectroscopy are on the same order as those from UV absorption measurements, consistent with the idea that AU Mic's debris disk possesses an inner hole with only a very low density of sub-micron sized grains or gas.

Key words. circumstellar matter – stars: individual: AU Microscopii – stars: coronae – X-rays: stars – protoplanetary disks

1. Introduction

The disks around young stars undergo dramatic changes during the first ~10 Myr after their host stars' birth, when the gas content of the disk largely disappears (Alexander 2008; Meyer et al. 2007; Hernández et al. 2006), leaving behind a so-called debris disk. The Kuiper belt and the asteroid belt are the solar system's analogs of stellar debris disks. The main components of an optically thin debris disk are small grains with about sub-micrometer sizes, larger bodies in the cm range and, possibly, planets, which are thought to form in the same time-span. The initial composition of the material in the debris disks after the transition phase is not well known. Collisions of already formed smaller bodies replenish the dust in the "older" debris disks, while it is not clear, whether this is also the source of the initial dust in the debris disk or whether it is remnant proto-planetary dust.

1.1. AU Mic and its activity

AU Mic is a 12^{+8}_{-4} Myr old M1 dwarf at a distance of about 10 pc, which belongs to the β Pic moving group (e.g. Barrado y Navascués et al. 1999; Zuckerman et al. 2001). AU Mic is one of the brightest nearby X-ray emitters ($\log L_X \approx 29.3$) and shows strong flaring activity, making AU Mic a valuable target for flare studies as shown by e.g. UV observations (Robinson et al. 2001).

At X-ray wavelengths AU Mic has been observed many times. The first *Chandra* observation provided the highest resolution spectrum, but was limited to the wavelength range below ~25 Å (Linsky et al. 2002). The XMM-*Newton* observation of AU Mic in 2000 was simultaneous with UV and VLA observations revealing several flares (Smith et al. 2005; Mitra-Kraev et al. 2005; Ness et al. 2003, for line fluxes). Furthermore, AU Mic was the target of FUSE and Hubble Space Telescope STIS observations (e.g. Pagano et al. 2000; Robinson et al. 2001; Del Zanna et al. 2002), aiming at the determination of the temperature structure of its chromosphere and corona.

1.2. AU Mic and its debris disk

The first indications for cold material around AU Mic go back to IRAS data, which exhibit excess emission at 60 μm (Mathioudakis & Doyle 1991; Song et al. 2002). A clear infrared excess at 850 μm in the spectral energy distribution (SED) of AU Mic was detected by Liu et al. (2004), clearly pointing to the existence of a debris disk. By assuming an optical thin disk at a single temperature, Liu et al. (2004) derived a mass of 0.01 $M_\oplus$ and a temperature of 40 K for the disk. These values have been confirmed by Rebull et al. (2008) from Spitzer data (see also Chen et al. 2005). Metchev et al. (2005) also confirmed the dust mass of about 0.01 $M_\oplus$ composed of grains in the submicron regime by modelling the optical, near-IR and SED data.

Optical observations by Kalas et al. (2004), initiated shortly after Liu et al. (2004), clearly showed the presence of a debris disk around AU Mic with a radial extent of at least 210 AU and almost perfectly edge-on. The disk has then been subsequently studied at optical wavelengths with, e.g., the Hubble Space Telescope (HST) and adaptive optics, making it one of the most well studied debris disks. The models derived by Krist et al. (2005) from their HST observation restrict the disk inclination to $i \gtrsim 89°$; they also confirmed the small-scale brightness variations detected by Kalas et al. (2004). These disk inhomogeneities can be readily explained by the existence of orbiting planets, however, no clear signatures of a planet have been found to date (Hebb et al. 2007; Metchev et al. 2005).

Two studies aimed at the detection of circum-stellar gas in the AU Mic disk. By their non-detection of far-UV H_2 absorption, Roberge et al. (2005) derived an upper limit on the gas column density along the line of sight of $N_{H_2} < 10^{19}$ cm^{-2}. The detection of H_2 in fluorescence enabled France et al. (2007) to derive a column density of 3×10^{15} cm^{-2} $< N_{H_2} < 2 \times 10^{17}$ cm^{-2} (T_{H_2} = 800 K and 2000 K, respectively). Comparing their H_2 value with the the CO results of Liu et al. (2004), they conclude that H_2 contributes less than about 1/30th to the total disk mass. The H absorption mainly traces interstellar rather than circumstellar material and has a column of $N_H = 2.3 \times 10^{18}$ cm^{-2}

(Wood et al. 2005), thus corresponding to within a factor of five to the Mg II absorption measurements of Redfield & Linsky (2002, $N_{\rm Mg} = 1.6 \times 10^{13}$ cm^{-2}), assuming solar abundances and Mg II to be the dominant Mg species (Slavin & Frisch 2002).

1.3. Disk models

Krist et al. (2005) used three-dimensional models of the scattering cross-section densities throughout the disk to interpret their HST images. They find that in the inner disk region (12 AU < r < 49 AU) the observations can be explained by a relatively uniform scattering cross-section density (forward scattering particles with an albedo of 0.5) in approximate correlation with the non-flaring disk model of Metchev et al. (2005). Augereau & Beust (2006) inverted the visible and near-IR scattered light profiles to study the grain properties and find that the scattered light is reflected at grains with sizes mainly between 0.1 μm and 1 μm. However, they require only about 1/20th of the total disk mass to account for the scattered light.

The dynamics of the grains were included by Strubbe & Chiang (2006) into their models and led them to explain the observations with a "birth ring" at about 40 AU, where larger planetesimals of about decimetre size are located. By collisions of these planetesimals the submicron sized grains are produced, which then, depending on their size, the radiation pressure, the gas content of the disk and the stellar wind, are expelled from the system or dragged into AU Mic. Strubbe & Chiang (2006) conclude that AU Mic's debris disk is dominated by destructive grain-grain collisions and that the inner part of the disk is largely void of submicron sized grains. These small grains mainly populate the outer part of the disk and result in the blueish appearance of a debris disk relative to the star, since submicron sized grains provide the largest fraction of the scattered light (Metchev et al. 2005). In contrast to the scattered light, the IR excess is caused by larger bodies because the mass of the submicron sized grains is too low to account for the observed emission (Fitzgerald et al. 2007). Augereau & Beust (2006) already noticed the need to increase their disk mass derived from the scattered light to reproduce the SED. The void of small grains in the inner part of the disk is consistent with the polarisation data of Graham et al. (2007) and the near-IR data of Fitzgerald et al. (2007), who derived an upper limit on the mass of submicron sized grains in the inner zone of the disk of $10^{-4}\ M_\oplus$.

2. The role of X-rays

The disk models strongly suggest that AU Mic is directly shining through its disk, therefore, absorption features related to the disk should in principle be present in the observed spectrum. AU Mic 's strong X-ray emission make this system a prime target to search for X-ray absorption features from a circum-stellar disk. The dominance of dust lets us expect a substantial amount of carbon in AU Mic 's disk, and thus we examine the influence of carbon on an X-ray transmission spectrum.

2.1. X-ray transmission in the disk of AU Mic

X-ray transmission spectra contain absorption features directly related to individual elements and, therefore, can be used to probe the elemental composition of an absorber (e.g. Nicastro et al. 2005; Williams et al. 2007). In particular, X-ray transmission spectroscopy allows an assessment of the carbon column density in the disk of AU Mic . In Fig. 1 we therefore illustrate

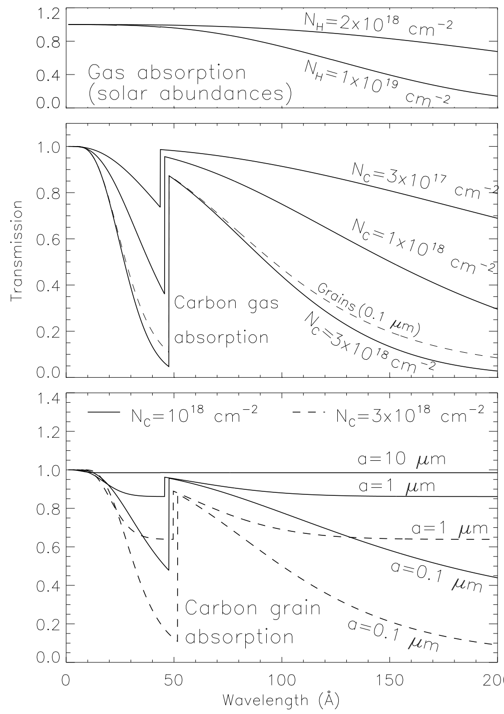

Fig. 1. X-ray transmission curves for different absorbers using `bamabs` from the PINTofALE-package based on the data of Balucinska-Church & McCammon (1992). *Top*: Absorption by cold gas with solar abundances. *Middle panel*: Gaseous carbon absorption. *Bottom*: Absorption by carbon grains. The individual curves are slightly shifted along the x-direction to maintain clarity. The C-K edge is located at 43.6 Å. For the grain absorption, the column density gives the total number of carbon atoms along the line of sight. Therefore, the number of grains in the line of sight depends on the grain-size, i.e., varies between the transmission curves for a fixed column density. For comparison, the dashed line in the gas absorption panel describes the transmission of carbon grains with $N_{\rm C} = 3 \times 10^{18}$ cm^{-2}.

the effects of X-ray absorption on the transmission curves for different column densities and the resulting soft X-ray spectrum near the carbon K-edge and out to 200 Å , i.e., in the band pass exclusively accessible to the *Chandra* LETGS. We specifically consider the case of cold gas absorption with solar abundances (Fig. 1, top panel), the case of a pure carbon absorber with various column densities (Fig. 1, middle panel), and the case of carbon absorbers locked up in various grain sizes (Fig. 1, bottom panel); clearly, for an absorber significantly composed of grains, self-shielding within the grains becomes important for the calculation of its transmission properties (see Appendix A, in Wilms et al. 2000). From Fig. 1 (bottom panel) it is clear that graphite grains with sizes around 0.1 μm are ideal to derive column densities from the carbon absorption edge, because they are so small that self-shielding is unimportant; the derived column density represents (almost) the number column density of carbon. With increasing grain sizes, the absorption features approach that of grey absorbers and grains with sizes in excess of 10 μm are virtually completely grey at X-ray wavelengths with only a marginal reduction of transmission. Therefore, the correspondence of absorption edge depth and column density holds strictly only for gas and small grains, while it breaks down for unknown grain sizes (in particular for sizes $\gtrsim 0.3\ \mu$m).

Figure 1 also illustrates that it is virtually impossible to reconstruct the elemental composition of an absorber from the reduced transmission outside the absorption edges. The shape of the reduced transmission at longer wavelengths can be mimicked by choosing appropriate column densities for almost every composition, e.g., the differences in transmission between a pure oxygen or a pure helium absorber in the *Chandra* LETGS wavelength range longwards of 50 Å is less than 10%. Note that only very few narrow absorption lines are available in the case of (low ionised) disks. In particular the 1s-2p transitions of oxygen (23.5 Å) and carbon (~44.8 Å, estimated from the Kα energy) are available (Wilms et al. 2000; Henke et al. 1993).

In the case of an absorber with solar abundances the absorption due to H, He and O reduces strongly the transmission around the absorption edge of C, however, the flux ratio between both sides of the edge depends only on the actual carbon column density. For a column density of $N_{\rm H} = 10^{21}$ cm^{-2} assuming cold gas with solar abundances, the transmission is reduced by a factor of 20, but the transmission at the low energy side of the C–K edge is about twice that of the high energy side, yet the resulting low flux level makes it virtually impossible to measure the depth of the C–K edge. Therefore, using the carbon absorption edge requires carbon to be strongly enhanced in the absorber so that it contributes significantly to the absorption without the overall reduced transmission by other elements.

2.2. The mass column density of AU Mic

The range of possible disk masses and hence column densities for AU Mic is relatively narrow. The different methods independently point to a total disk mass of 0.01 $M_\oplus$ ($\approx 6 \times 10^{25}$ g, cf., Sect. 4.1 in France et al. 2007; Fitzgerald et al. 2007), however, the distribution of this disk mass between small grains and larger bodies and their locations are not particularly well constrained. The most recent disk models including the grain dynamics attribute less than a tenth of the total mass to small grains, while most of the mass is stored in larger bodies with sizes up to ~10 cm. In order to test these scenarios we calculate the mass column density by distributing 0.01 $M_\oplus$ uniformly within the inner zone of the Krist et al. (2005) model (10 AU–50 AU, $h \approx 2$ AU), i.e., the zone where the dust causing the infrared excess should be located. The mass column density σ is given by

$$\sigma = \frac{M}{V}d = \frac{M}{\pi h(r_{\rm o}^2 - r_{\rm i}^2)} \cdot (r_{\rm o} - r_{\rm i}) = \frac{M}{\pi h(r_{\rm o} + r_{\rm i})} \approx 7 \times 10^{-4} {\rm g/cm^2}\,, \quad (1)$$

where M is total disk mass within 50 AU, V is the volume occupied by the disk, d is the line of sight and $r_{\rm o}$ and $r_{\rm i}$ are the outer and inner radii of the considered region, assuming no significant contribution of larger bodies.

As discussed above, the associated X-ray absorption features depend on the chemical composition of the disk and the grain sizes and shapes. Although Roberge et al. (2006) found that in the β Pic disk the chemical composition might deviate from solar by factors of a few with carbon being overabundant, we assume for the AU Mic disk that H and He are virtually absent and that the mass is stored in the remaining elements with solar abundances. This implies that ~15% of the mass is stored in carbon atoms. The number density of carbon atoms in the line of sight is then

$$N_{\rm C} = X_{\rm C}\frac{\sigma}{m_{\rm C}} \approx 0.15 \frac{7 \times 10^{-4} {\rm g/cm^2}}{12 \times 1.66 \times 10^{-24} {\rm g}} = 5 \times 10^{18} {\rm cm^{-2}}, \quad (2)$$

where $X_{\rm C}$ is the mass-fraction of carbon (15%) and $m_{\rm C}$ is the mass of a carbon atom.

From Fig. 1 it is clear that such column densities should impose strong feature on the transmission spectrum detectable with a *Chandra* LETGS observation.

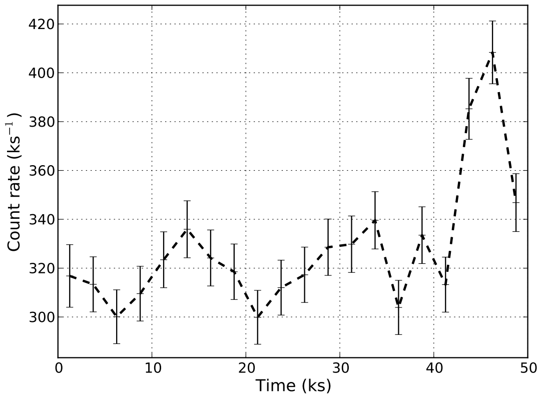

Fig. 2. LETGS zeroth order X-ray lightcurve of AU Mic. Time represents the time after the start of the observation (MJD = 54643.506).

3. Observations, data reduction and immediate results

3.1. Observation and data reduction

Au Mic was observed on 30 June 2008 with the *Chandra* LETGS (Obs-ID 8894). The total exposure time was 50 ksec and the data reduction was carried out using CIAO 4 (Fruscione et al. 2006). The photon detector of the LETGS is the HRC-S, a microchannel plate, which does not provide sufficient energy resolution to separate the individual diffraction orders superposed on the same detector area. Therefore, to allow an analysis of the data with standard tools like XSPEC (Arnaud 1996), we constructed new response matrices including up to ninth diffraction order contributions following the instructions given in the CIAO threads[1] (see Appendix A). Line fluxes were obtained using `CORA` which accounts for the Poisson character of the data (Ness & Wichmann 2002).

We experimented with the "standard" filters (light, medium and heavy) and with the new `Gain Map and Pulse-Height` filter[2]. Around the carbon edge, the difference in the background fraction is only a few percent between the light and medium filter while significant for the new filter; we list the corresponding values in Table 2. The figures and numbers given in the text pertain to the standard light filter, unless otherwise noted.

3.2. Global plasma properties

In Fig. 2 we show the zeroth order X-ray count rate of AU Mic vs. time; obviously, the light curve is more or less constant

[1] http://cxc.harvard.edu/ciao/threads/hrcsletg_orders/
[2] http://cxc.harvard.edu/contrib/letg/GainFilter/

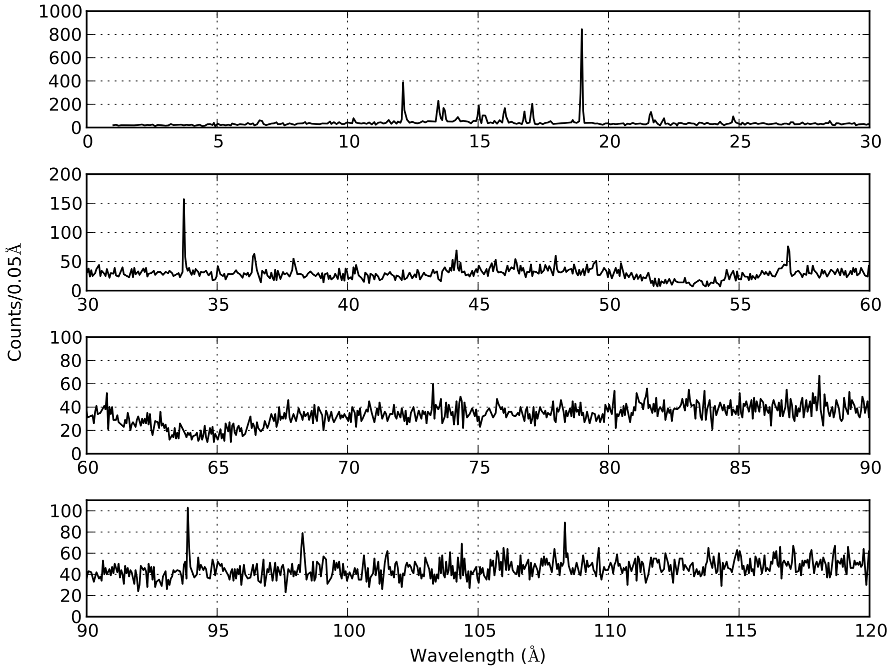

Fig. 3. The measured spectrum in the spectral range relevant for the analysis. Shown is the sum of the positive and the negative diffraction order.

during the first 40 ksec of the observations, afterwards there is a small flare-like increase. We do not treat this increase separately but analyse the observation in total. In Fig. 3 we show the recorded LETGS spectrum up to 120 Å; sub-regions will be shown individually in the next sections. AU Mic 's X-ray spectrum is typical of an active star, showing the strong Ne emission features and a strong OVIII Ly$_\alpha$ line; the carbon Ly$_\alpha$ line is also quite strong. The OVII triplet between 21.6 and 22.1 Å as well the Fe XVII feature at 15.03 Å are relatively weak as well as all features attributable to N; we do point out the emission lines between 90 and 120 Å attributable to highly ionised iron. We used XSPEC to fit the X-ray spectrum using a combination of three APED models (variable abundances, Smith et al. 2001) with one absorption component. The increasing background at longer wavelengths make these bins less useful for the spectral analysis. We therefore restrict the wavelength range to values between 5 Å and 35 Å. Using the full wavelength range does not influence the two low temperature components; only the best fit temperature of the high temperature component doubles. This is mainly driven by a single, somewhat strangely shaped Fe XX line at 132.85 Å. Furthermore, the abundances of Mg, Al, Ca and Ni (low FIP) were coupled to that of Fe in order to decrease the number of free parameters. The thus obtained fit results (listed in Table 1) show the inverse FIP effect usually found in M-dwarfs (Robrade & Schmitt 2005). The temperature structure and the abundances compare well with a fit performed with the XMM-*Newton* RGS-data of AU Mic (Obs-ID 0111420101).

Table 1. Coronal properties of AU Mic .

Property	Value
N_H	2×10^{18} cm^{-2}
kT_1	0.29 ± 0.02 keV
EM_1	$7.5^{+1.7}_{-1.5} \times 10^{51}$ cm^5
kT_2	$0.67^{+0.04}_{-0.03}$ keV
EM_2	$11.0^{+3.1}_{-2.6} \times 10^{51}$ cm^5
kT_3	$1.49^{+0.61}_{-0.28}$ keV
EM_3	$5.6^{+1.5}_{-1.6} \times 10^{51}$ cm^5
Element	Abundance
C	0.9 ± 0.3
N	0.8 ± 0.3
O	0.5 ± 0.2
Ne	$1.3^{+0.3}_{-0.1}$
Si	0.3 ± 0.1
S	$0.1^{+0.2}_{-0.1}$
Fe	$0.19^{+0.06}_{-0.04}$

Notes. Abundances are given relative to that of Asplund et al. (2009) and 90% errors are given.

4. Absorption at the carbon edge

The carbon K-edge at 43.6 Å (284 eV, i.e., the energy needed to expell a K-shell electron from an isolated carbon atom) is a promising absorption feature in the *Chandra* LETGS wavelength band. In this region, the line emission is relatively small compared to continuum emission. The oxygen edge, located at 23.1 Å (536 eV), is also a good candidate, but with an enhanced line-to-continuum ratio. This increases the errors since the prediction of the line emission is not possible with the required precision. Unfortunately, the UV/Ion shield of the HRC-S also contains a large amount of carbon ($N_C \approx 10^{18}$ cm^{-2}) leading to an instrumental feature very similar to that of expected interstellar/circum-stellar carbon absorption. Still, the high continuum fraction of the first order emission around the C–K edge makes this region more promising than the O–K edge.

Table 2. Contributions at the C–K edge (summed continuum and line emission).

Contribution	Wavelength range 30–43 Å		44–48 Å	
Light filter:				
Total counts	6495		2593	
First order emission	1546	23.8%	1014	39.1%
Higher order contribution	569	8.8%	172	6.6%
Background	4251	65.4%	1287	49.6%
`Gain Map and Pulse-Height` **filter:**				
Total counts	4582		1939	
First order emission	1467	32.0%	949	48.9%
Higher order contribution	565	12.3%	173	8.9%
Background	2376	51.9%	705	36.4%

Notes. Listed are the total counts of the complete model (sum of positive and negative diffraction order). Top is the result from the standard light filtering and in the bottom the corresponding values for the new `Gain Map and Pulse-Height` filtering are shown.

4.1. The model

As is obvious from Fig. 1 the height of the C edge does depend sensitively on the carbon column density (and on the grain sizes). Therefore our basic idea to measure the height of that edge is as follows: We divide the wavelength range around the C edge into a low (44–48 Å) and a high energy band (30–43 Å) and sum up the counts in these two bands to increase the signal. By comparing these two count numbers with models containing specific amounts of carbon absorption the best fit carbon column density can be found.

We do not extend the wavelength range to longer wavelengths since these longer wavelength bins are close to the detector gap at 50 Å of the negative diffraction order, where the data is less reliable. We also exclude the immediate region around the edge and around the 1s-2p carbon absorption line (~44.8 Å) because of the relatively little known fine-structure of the carbon absorption edge. Exclusion of a larger wavelength region around the edge does not change the results significantly (see Fig. 7). Increasing the amount of carbon in the line of sight, changes the flux-ratio between the low and high band; since the the change in transmission in the low energy band is comparably small, we normalise our model to match the low energy band. Therefore we carry out only a differential analysis.

For our modelling of the recorded spectrum above and below the carbon edge we consider the following four components as contributors to the counts around the C–K edge.

1. The continuum emission.
2. The superimposed line emission.
3. The higher diffraction orders which cannot be filtered out due to the low intrinsic energy resolution of the photon detector (HRC-S).
4. The enhanced background of the LETGS due to a wiring error of the micro-channel plate detector.

In the following we describe our modelling of the individual components and discuss their accuracy; the given errors pertain to the higher energy side of the edge while the numbers in brackets correspond to the lower energy side. Since the models are normalised to match the low energy side of the edge, an error at this side will also influence the number of predicted counts at the high energy side of the edge (by roughly the same amount). Figure 4 shows the complete model and the individual model contributions are shown in Fig. 5.

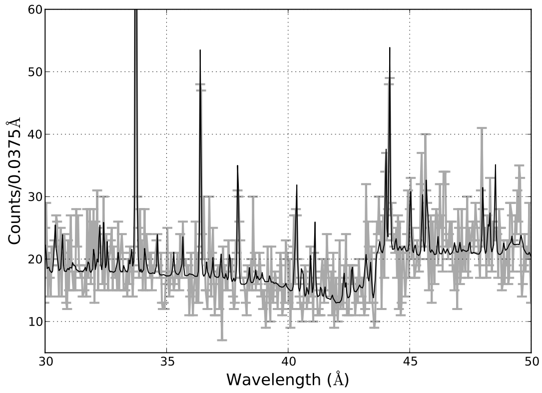

Fig. 4. Model and data around the C–K edge (sum of both diffraction orders).

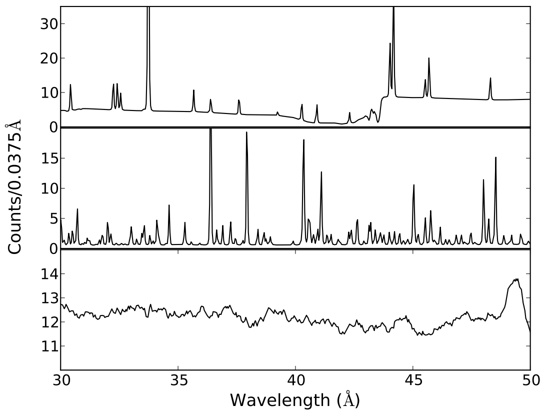

Fig. 5. The different contributions to the measured counts around the C–K edge. *Top*: First order emission. *middle*: Higher order contribution. *bottom*: Background.

The continuum is the simplest component since its shape around the C–K edge does not change noticeably for reasonable changes in the plasma properties. The main spectral components are known from our global spectral modelling, but changing, for example, the temperature by about 50%, changes the number of counts left of the carbon edge by less than 2% (50 cts), while preserving the counts at the right side of the edge by choosing an appropriate normalisation.

The treatment of emission lines is less straightforward. We estimate that contribution of the first diffraction order emission lines is not predictable with a better than 10% accuracy. Therefore, a region of 0.2 Å around each strong line (based on our XSPEC/APED emission model) was excluded from the two energy bands thus removing ~98% of the line flux of these strong lines. Only 65% and 73% of the available bins are therefore used in the 30–43 Å and 44–48 Å range, respectively. As a consequence, the ratio between line and continuum emission is below 10% in the high and low band. In addition, the remaining counts from unresolved lines are predicted from the emission model and are added to the model as a correction; these numbers turn out to be 50 and 35, respectively. Taking this numbers as a conservative estimate of the error, the impact of these lines on

A&A 516, A8 (2010)

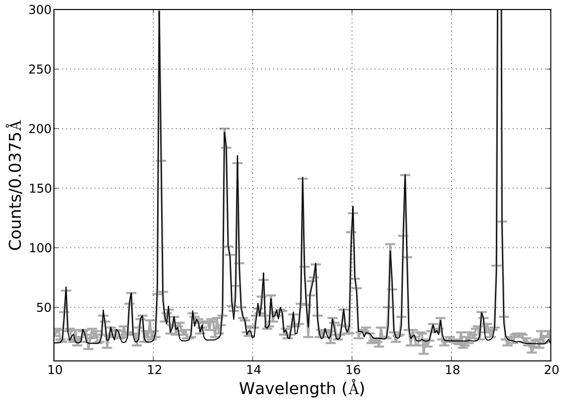

Fig. 6. Data and model for the sum of the positive and the negative diffraction order. Note that the model is not based on a physical model (except for the continuum and the absorption).

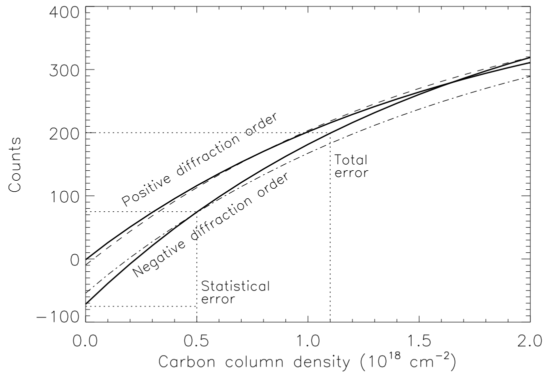

Fig. 7. Number of missing (positive count number) or overpredicted photons (negative count number) as a function of the assumed carbon absorption column density in the model. The flattening of the curves indicates that the flux will, eventually, be completely absorbed in the considered wavelengths range for even higher column densities. The dashed line is the average of the positive and negative order using the new `Gain Map and Pulse-Height` filtering. The dashed-dotted line is the result using the wavelength ranges 30–42 Å and 45–48 Å. The statistical errors reflects only first order errors. For a discussion of the errors see Sect. 4.2.

the derived carbon column density is quite small, therefore, also the influence of "unknown" lines ought to be small.

The third diffraction order of the LETGS is the strongest higher order contribution to the region around the C–K edge, since the second diffraction order is suppressed by the grating design. Unfortunately, AU Mic being an active star, the Ne IX and Ne X lines are quite strong, and their third order components are easily discernible in our LETGS spectrum (cf. middle panel in Fig. 5). However, first and third order are always measured simultaneously, thus, by fitting the stronger (identifiable) lines independently in the wavelength range shorter than the C–K edge provides the desired description of the higher order contamination. The selection of the lines is based on the APED model (see Sect. 3), the *Chandra* HETGS spectrum of AU Mic and on the lines visible in the Capella spectrum (Capella is a calibration target of the LETGS, thus providing about 400 ks of data and has an approximately comparable temperature structure as AU Mic). Note that this method is unaffected by the uncertainties of the spectral model. Figure 6 shows the model of the wavelength range which provides the strongest contamination at the carbon edge; 97% of the photons in this range are included in the model. Taking the remaining 3% as a measure for the accuracy of the higher order model, these 3% correspond to only 12 (4) photons not contained in the higher order model between 30 Å and 48 Å. We can therefore neglect this effect on the derived carbon column density compared to the other factors like the statistical noise or a potential error in the higher order diffraction efficiencies, which would for a 10% error[3] result in an error on the 30 count level (6 cts).

The last component to consider is the background. Fortunately, the background is relatively uniform in the wavelength range between 30 Å and 48 Å. Since the bins in the "line-free" regions are all summed up, the impact of the short-scale variation should be further reduced. The largest problem of the background in this analysis is the enlarged count number leading to an increased statistical uncertainty which amounts to about 50 (30) counts. Since the models are tuned to match the longer wavelength side of the edge, the combined statistical error is ~75 counts at the high energy side of the edge.

[3] http://asc.harvard.edu/cal/

4.2. The influence of carbon absorption

Varying the absorbing carbon column density changes the transmission curve in the whole wavelength range (see Fig. 1). Therefore, it is necessary to re-adjust the continuum-level and the amplitudes of the emission lines for the higher order contribution to construct a new best fit model. The influence of the carbon absorption on the low-energy side of the edge is relatively small (cf. Fig. 1), therefore, we tuned the models so that this region matches the data by varying the continuum normalisation of the model. The normalisations of the models with zero absorption and $N_{\mathrm{C}} = 2 \times 10^{18}$ cm^{-2} differ by about 20%. Due to the strong line emission (there are not many wavelength regions without line emission at shorter wavelengths) and the refitting of these lines, this does not noticeably change the fit-quality in the shorter wavelength region. Having thus fixed our model to account for the number of counts at the low-energy side of the carbon edge, we can compute the model counts on the high energy side of the carbon edge as a function of the assumed carbon column density and hence, by comparison with the observation, the missing model counts, since increasing the carbon column density leads to a more and more relatively reduced model count number below the edge. The dependence of this number of missing counts in the model on the assumed carbon absorption is graphically displayed in Fig. 7. Depending on the accepted accuracy of our model we can read off the maximum number of carbon atoms along the line of sight assuming gaseous absorption (i.e. no self-shielding). If grains cause the absorption, a larger number of carbon atoms in the line of sight is required to produce the same number of missing counts. Explaining gaseous absorption with $N_{\mathrm{C}} = 10^{18}$ cm^{-2} requires a 1.3 times higher number of carbon atoms in the line of sight for 0.1 μm sized grains, a 1.9 times higher number for 0.3 μm and an almost 5 times higher number for 1.0 μm grains.

Collecting the errors attached to the individual model components, we estimate an overall error of approximately 200 (80) counts. We cannot simply add the error of both sides of the edge, since it is rather unlikely that the same error-source results in an erroneously increased number of counts at one side of the edge while, at the same time, underestimating the counts at the other side of the edge. Therefore, we conclude that a robust estimate of the error is about 200 counts or $N_C \lesssim 10^{18}$ cm^{-2} (for pure carbon gas).

The result shown in Fig. 7 suggests only a small amount of carbon-atoms along the line of sight ($N_C \sim 10^{17}$ cm^{-2}), which might be supported by a slight deficit in counts around the carbon 1s-2p absorption line. However, this is probably only a statistical effect since this effect is reduced by using the stronger `Gain Map and Pulse-Height` background filtering (see dashed line in Fig. 7).

5. Constraining the total absorption

The method described above offers the ability to directly constrain the column density of carbon in the line of sight. It is, on the other hand, not useful to set tight contrains on the "total" absorbing column density since only a narrow wavelength range is inspected. Emission lines located at largely different wavelengths better utilise the large wavelength coverage of the LETGS. Usage of a single element and ionisation stage reduces the dependence on the reconstruction of the abundances and the temperature structure of the corona.

A good candidate for such a study is Fe XVIII with lines at 14.21 Å (blend of 14.2060 and 14.2085 Å), 16.08 Å (blend of 16.0760 and 16.0913 Å), 93.92 Å and 103.94 Å. Assuming that all these lines are produced in the same environment, the relative fluxes of these ions depend only weakly on the temperature structure; the dependence on the density is virtually negligible for densities around $n_e \sim 10^{10}$ cm^{-3} as usually found in stellar coronae (e.g. Ness et al. 2002). Unfortunately the stronger Fe XVIII lines at shorter wavelength are blended. While the 14.21 Å lines do posses only small contributions from the 14.17 Å Fe XXI line and the Fe XVIII doublet at 14.26 Å, the 16.08 Å is blended by the strong O VIII doublet at 16.00 Å and a Fe XIX line at 16.11 Å, which amounts to about a fourth of the Fe XVIII emission for the temperatures in question. The derived fluxes of the short wavelength lines are comparable to the available HETGS data (Obs-ID 17).

The Chianti package (Dere et al. 1997; Landi et al. 2006) was used to predict relative line fluxes. To investigate the temperature dependence of the relative fluxes, a Gaussian fit of the emission measure distribution (EMD) of Appendix C was performed. The line ratios were then calculated for Gaussian EMDs with different peak temperatures and widths, e.g. the peak temperature was changed up to $\Delta \log(T) = 0.4$ (see Fig. 8). The measured fluxes (sum of both LETGS orders) of the above lines together with predicted ratios (the 14.21 Å line normalised to 1.0) are listed in Table 3.

From the difference between predicted and measured counts the required hydrogen column density (assuming solar abundances) can be calculated. The resulting ranges are listed in Table 3, they include the uncertainty in the reconstruction of the temperature and the statistical error. The influence of the adopted temperature structure is small compared to the statistical errors. Comparison of the line fluxes from the standard filtering and that of the new `Gain Map and Pulse-Height` filtering shows that both values agree well. However, the upper limits from these fluxes are higher than that from the light filtered data since their line fluxes at longer wavelength are lower ($N_H < 11{\times}10^{18}$ cm^{-2}).

Summing the line fluxes of the short wavelengths lines and combining the upper limits of the two long wavelength lines

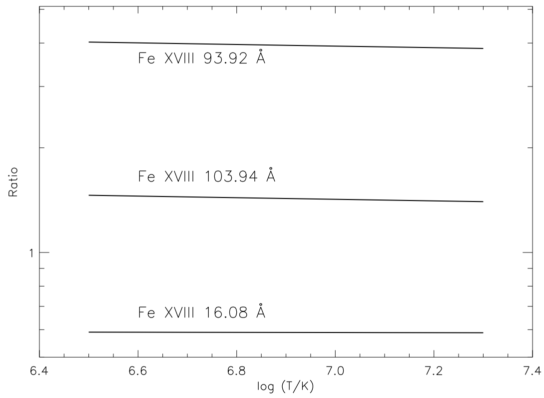

Fig. 8. Ratio of the line-fluxes to the Fe XVIII 14.21 Å line using Gaussian-like emission measure distributions with a width of $\log(T/\mathrm{K}) = 0.5$.

improves the upper limit to $N_H < 4 \times 10^{18}$ cm^{-2} (1σ). Instead of using one single ion, we checked the ratio of the two strongest Fe lines at short and long wavelengths (Fe XVII 15.02 Å and Fe XX 132.85 Å). Their ratio depends more strongly on the temperature structure with predicted ratios (132.85 Å/15.02 Å) between 1.0 ($\log T = 6.5$) and 2.0 ($\log T = 7.3$) for a shallow EMD ($\Delta T = 0.5$). However, their resulting upper limit is only slightly higher ($N_H < 6 \times 10^{18}$ cm^{-2}) than that from the Fe XVIII lines.

The X-ray absorption at wavelengths of around 100 Å is caused mainly by He atoms. The upper limit on He from the observed line fluxes is $N_{He} < 6 \times 10^{18}$ cm^{-2} assuming that the absorption is caused exclusively by He and $N_H < 14{\times}10^{18}$ cm^{-2} for a pure Hydrogen absorber. Similarly, upper limits on the abundance of other absorbing elements can be derived under the assumption that they are the only absorbing species.

The analysis of the absorption towards Capella by Gu et al. (2006) using a comparable method has an error of about a factor of five lower which is consistent with the larger data base available for Capella which is a calibration target of the *Chandra* LETGS.

6. Discussion

Neither the edge based method nor the line based method are able to find significant absorption along the line of sight towards AU Mic. For both methods, the statistical error overwhelms the error caused by the incomplete models. This is clear by inspection of Table 3 for the line based method but is also true for the edge analysis. The detectable carbon column density from an analysis of the edge height is $5\ldots50 \times 10^{17}$ cm^{-2} for artificial stars with X-ray fluxes within a range of five around that of AU Mic (50 ks LETGS exposure). This value decreases only slowly for even higher X-ray fluxes and "saturates" at $N_C \approx 3{\times}10^{17}$ cm^{-2} due to the potential error in the higher order contribution (see Appendix B). The edge-method provides a direct upper limit on the carbon content of the disk without any assumption on the absorber. Its limit is about that provided by the line based method assuming that only carbon is in disk, i.e., calculating the maximum carbon column density allowing the detection of the line-flux from the long wavelengths Fe XVIII lines.

Table 3. Strong Fe XVIII lines and measured fluxes.

Wavelength	Measured flux	Measured flux[a]	Ratio to	Predicted	Corresponding	Corresponding
	(10^{-5}ph/cm^2/s)		14.21 Å		N_H (10^{18} cm^{-2})	N_C (10^{17} cm^{-2})
14.21	6.3 ± 1.4	6.3 ± 1.4	–			
16.08	5.7 ± 1.3	6.3 ± 1.0	0.9 ± 0.3 (1.0± 0.3)	0.6[b]		
93.92	28.9 ± 3.7	25.8 ± 3.3	4.6 ± 1.1 (4.1 ± 1.1)	3.9 ± 0.3	0–7	0–8
103.94	11.1 ± 3.4	9.7 ±2.7	1.8 ± 0.7 (1.5 ± 0.5)	1.4 ±0.1	0–8	0–10

Notes. The values for the new `Gain Map and Pulse-Height` filtering are also given. Their corresponding ratios are given in brackets in the ratio column while the values in the columns for the corresponding absorbing column densities are based on the standard filter. [(a)] New `Gain Map and Pulse-Height` filter; [(b)] plus 0.2 blend.

Two measurements of H (atomic and molecular) restrict the total hydrogen column density in the line of sight towards AU Mic to $N_H \lesssim 4\times10^{19}$ cm^{-2} (mainly H_2, Roberge et al. 2005). From this value, only 2×10^{18} cm^{-2} are atomic hydrogen (Wood et al. 2005). Note that the conversion of molecular hydrogen to N_H in stellar disks is uncertain (e.g., Kamp et al. 2007), while molecular hydrogen is orders of magnitude less abundant than atomic hydrogen in the nearby interstellar medium ($d < 200$ pc; Lehner et al. 2003). The location of the fluorescent H_2 detected by France et al. (2007) is not necessarily along the line of sight and leaves space for an additional H_2 not contributing to the fluorescent H_2 emission.

X-rays are sensitive to both, atomic and molecular, hydrogen. H_2 absorption is about 2.8 times stronger than that of a single H atom (Wilms et al. 2000). Furthermore, the X-ray absorption is insensitive to the excitation state of H_2. Therefore, the 5σ upper limit from the UV measurement ($N_{H_2} < 17\times10^{18}$ cm^{-2}) corresponds to about $N_H \lesssim 50\times10^{18}$ cm^{-2} in soft X-rays; the same order as the upper limit derived from the line fluxes assuming a pure hydrogen absorber. The X-ray upper limit on H also includes H_2 in the line of sight located in the inner and outer part of the disk which might have different excitation stages and therefore complements the upper limit of Roberge et al. (2005). Furthermore, the detected line fluxes at $\lambda \gtrsim 100$ Å can be translated to upper limits on other elements restricting the gas / small grain content of the disk, e.g., that of carbon in gaseous form and small grains ($s \lesssim 0.3\,\mu$m, see Table 3).

7. Summary

We analysed the impact of absorption caused by AU Mic's debris disk on its observed X-ray spectrum resulting in three upper limits on the column densities for hydrogen, helium and carbon:

- $N_H < 2.8\times10^{19}$ cm^{-2} (pure H absorption)
- $N_{He} < 1.2\times10^{18}$ cm^{-2} (pure He absorption)
- $N_C < 10^{18}$ cm^{-2} (pure C absorption).

Assuming an absorber with solar abundances, the upper limit is $N_H < 10^{19}$ cm^{-2}, which is about a factor of five higher than the pure interstellar value. The statistical error caused by counting statistics and the high background prevents to set lower limits, while the presented methods are in principle more sensitive.

Both upper limits are consistent with the idea that the AU Mic disk is optically thin in the radial direction as proposed by recent analyses from optical and infrared measurements, and in line with current disk models, which assume that the inner part of the disk is almost void of small grains. The debris of the collisions of planetesimals in the "birth-ring" populate mainly the outer part of the disk, where their density is so low that they escape a detection in this X-ray observation. In the inner part of the disk larger grains hold the mass as predicted by birth-ring scenarios.

Roberge et al. (2005) state that they find weak signs of H_2 absorption on the order of 10^{18} cm^{-2} in their UV data. To reach this level with the *Chandra* LETGS setup, longer integration times are required. For Capella, a calibration target of the LETGS, the $N_H \sim 10^{18}$ cm^{-2} range is accessable. However, it seems unlikely to reach down to $N_H \sim 10^{17}$ cm^{-2} with the present instrumentation as would be required to safely distinguish a hypothetical circum-stellar H_2 component in the $N_H \sim 10^{18}$ cm^{-2} range from the interstellar atomic H absorption.

Appendix A: Higher order response matrices for XSPEC

The response matrices contain the probabilities describing how the detector will respond on a photon with a given energy. Including the higher diffraction orders therefore requires to add additional probabilities at two, or more times the rest wavelength. Since the resolution grows with the order number, the energy grid needs to be refined accordingly. The FITS-specification for response files (CAL/GEN/92-002) already includes the concept of wavelength groups which are ideal to reduce the size of the final response matrix.

Appendix B: Carbon detectability

To estimate the detectability of carbon absorption from the edge height, we need to quatify the different error contributions as a function of the source count-rate. Concerning the error due to unknown unresolved first order emission lines and uncertainties in the temperature structure, we regard a correlation with the statistical error as realistic, since better data quality enables a more precise temperature reconstruction and, in turn, a better model for the emission lines around the carbon edge. However, the detailed dependence on the source count-rate might be more complicated. The higher order contribution scales with the source flux; therefore, its error scales also linearly with the first order flux since calibration uncertainties dominate the error. Figure B.1 shows the minimum detectable carbon column density for different source fluxes assuming a pure carbon disk. It shows that column densities below 3×10^{17} cm^{-2} can only be achieved for stars that are at least one order of magnitude X-ray brighter than AU Mic and with a hypothetical 500 ks observation. However, the existence of other elements in the disk increases the detectable column density due to the absorption of the first order flux around the carbon edge. Furthermore, without knowing the composition of the disk, the extra absorption changes the continuum slope around the carbon edge and therefore increased the uncertainty in the carbon column density.

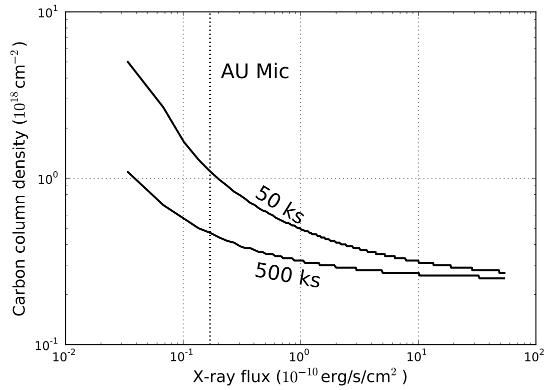

Fig. B.1. The detectable carbon column density by measuring the jump height at the carbon edge as a function of the X-ray flux (0.1 keV–2.0 keV). Here, a pure carbon disk is assumed. The two lines represent a 50 ks and a 500 ks exposure with the LETGS. The same temperature structure as AU Mic is assumed which determines the higher order contribution around the carbon edge. The vertical dotted line indicates the X-ray flux of AU Mic.

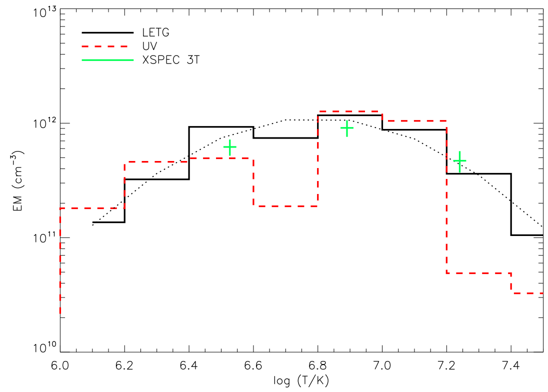

Fig. C.1. The reconstructed emission measure distribution. The dotted line indicates the Gaussian fit to the EMD.

Table C.1. Strong lines and measured fluxes.

Ions	Wavelength	Flux (10^{-5}ph/cm^2/s)
Si XIII	6.65	4.5 ± 0.7
Ne X	10.24	6.3 ± 1.0
Ne IX	11.54	6.3 ± 1.0
Ne X	12.13	44.1 ± 2.1
Ne IX	13.45	32.8 ± 1.9
Ne IX	13.54	11.2 ± 1.3
Ne IX	13.70	22.9 ± 1.6
Fe XVIII	14.21	6.3 ± 1.4
Fe XVII	15.01	18.0 ± 1.4
Fe XIX/O VIII	15.18	6.4 ± 1.1
Fe XVII/Fe XX	15.26	8.4 ± 1.1
O VIII	16.01	17.6 ± 1.5
Fe XVIII	16.08	5.7 ± 1.3
Fe XVII	16.78	12.1 ± 1.2
Fe XVII	17.10	30.2 ± 1.9
O VIII	18.97	110.3 ± 3.3
O VII	21.61	29.2 ± 2.3
O VII	21.79	10.0 ± 1.6
O VII	22.10	19.4 ± 2.0
N VII	24.79	16.6 ± 2.0
C VI	33.73	33.9 ± 2.9
Fe XVIII	93.89	28.9 ± 3.7
Fe XVIII	103.92	11.1 ± 3.4
Fe XIX	108.33	26.2 ± 4.3
Fe XX	118.66	14.1 ± 4.2
Fe XX	121.85	17.0 ± 5.0
Fe XXI	128.75	<16.2
Fe XX	132.85	37.7 ± 8.6
Fe XXII	135.78	27.6 ± 7.9

Appendix C: The emission measure distribution

The large wavelength coverage of the LETGS offers the ability to quantify the emission measure distribution (EMD) in the corona. Using the lines listed in Table C.1, we reconstructed the EMD using the PintOfAle (Kashyap & Drake 2000) package. Our result compares well with the result obtained using the line fluxes measured in the UV wavelength range by Del Zanna et al. (2002). We also experimented with the Chianti package (Dere et al. 1997; Landi et al. 2006) and found that the results are strongly influenced by numerical problems due to the shallow temperature coverage of the observed lines. However, both methods give rather similar results.

It is clear, that most of the emission is produced in the temperature range $6.4 < \log(T/\mathrm{K}) < 7.2$. We also show in Fig. C.1 the location of the three temperature components from the XSPEC fit with APEC models (variable abundances). For an estimate of the error in the relative linefluxes in Sect. 5 we fitted the emission measure distribution with a single Gaussian. We can then change the centroid and the width of the Gaussian to analyse the impact of an error in the reconstructed temperature distribution on the relative linefluxes.

Acknowledgements. We thank Dr. P. Predehl (MPE) for kindly providing the opportunity to observe AU Mic with the *Chandra* LETGS. This work has made use of data obtained from the *Chandra* and XMM-*Newton* data archives. CHIANTI is a collaborative project involving the NRL (USA), RAL (UK), MSSL (UK), the Universities of Florence (Italy) and Cambridge (UK), and George Mason University (USA). PCS acknowledges support from the DLR under grant 50OR703.

References

Alexander, R. 2008, New Astron. Rev., 52, 60
Arnaud, K. A. 1996, in Astronomical Data Analysis Software and Systems V, ed. G. H. Jacoby, & J. Barnes, ASP Conf. Ser., 101, 17
Augereau, J.-C., & Beust, H. 2006, A&A, 455, 987
Asplund, M., Grevesse, N., Sauval, A. J., & Scott, P. 2009, ARA&A, 47, 481
Balucinska-Church, M., & McCammon, D. 1992, ApJ, 400, 699
Barrado y Navascués, D., Stauffer, J. R., Song, I., & Caillault, J. 1999, ApJ, 520, L123
Chen, C. H., Patten, B. M., Werner, M. W., et al. 2005, ApJ, 634, 1372
Del Zanna, G., Landini, M., & Mason, H. E. 2002, A&A, 385, 968
Dere, K. P., Landi, E., Mason, H. E., Monsignori Fossi, B. C., & Young, P. R. 1997, A&AS, 125, 149
Fitzgerald, M. P., Kalas, P. G., Duchêne, G., Pinte, C., & Graham, J. R. 2007, ApJ, 670, 536
France, K., Roberge, A., Lupu, R. E., Redfield, S., & Feldman, P. D. 2007, ApJ, 668, 1174
Fruscione, A., McDowell, J. C., Allen, G. E., et al. 2006, in SPIE Conf. Ser., 6270
Graham, J. R., Kalas, P. G., & Matthews, B. C. 2007, ApJ, 654, 595
Gu, M. F., Gupta, R., Peterson, J. R., Sako, M., & Kahn, S. M. 2006, ApJ, 649, 979
Hebb, L., Petro, L., Ford, H. C., et al. 2007, MNRAS, 379, 63
Henke, B. L., Gullikson, E. M., & Davis, J. C. 1993, Atomic Data and Nuclear Data Tables, 54, 181
Hernández, J., Briceño, C., Calvet, N., et al. 2006, ApJ, 652, 472
Kalas, P., Liu, M. C., & Matthews, B. C. 2004, Science, 303, 1990

Kamp, I., Freudling, W., & Chengalur, J. N. 2007, ApJ, 660, 469
Kashyap, V., & Drake, J. J. 2000, Bull. Astron. Soc. India, 28, 475
Krist, J. E., Ardila, D. R., Golimowski, D. A., et al. 2005, AJ, 129, 1008
Landi, E., Del Zanna, G., Young, P. R., et al. 2006, ApJS, 162, 261
Lehner, N., Jenkins, E. B., Gry, C., et al. 2003, ApJ, 595, 858
Linsky, J. L., Ayres, T. R., Brown, A., & Osten, R. A. 2002, Astron. Nachr., 323, 321
Liu, M. C., Matthews, B. C., Williams, J. P., & Kalas, P. G. 2004, ApJ, 608, 526
Mathioudakis, M., & Doyle, J. G. 1991, A&A, 244, 433
Metchev, S. A., Eisner, J. A., Hillenbrand, L. A., & Wolf, S. 2005, ApJ, 622, 451
Meyer, M. R., Backman, D. E., Weinberger, A. J., & Wyatt, M. C. 2007, in Protostars and Planets V, ed. B. Reipurth, D. Jewitt, & K. Keil, 573
Mitra-Kraev, U., Harra, L. K., Güdel, M., et al. 2005, A&A, 431, 679
Ness, J.-U., Schmitt, J. H. M. M., Audard, M., Güdel, M., & Mewe, R. 2003, A&A, 407, 347
Ness, J.-U., Schmitt, J. H. M. M., Burwitz, V., et al. 2002, A&A, 394, 911
Ness, J.-U., & Wichmann, R. 2002, Astron. Nachr., 323, 129
Nicastro, F., Mathur, S., Elvis, M., et al. 2005, ApJ, 629, 700
Pagano, I., Linsky, J. L., Carkner, L., et al. 2000, ApJ, 532, 497
Rebull, L. M., Stapelfeldt, K. R., Werner, M. W., et al. 2008, ApJ, 681, 1484
Redfield, S., & Linsky, J. L. 2002, ApJSS, 139, 439
Roberge, A., Weinberger, A. J., Redfield, S., & Feldman, P. D. 2005, ApJ, 626, L105
Roberge, A., Feldman, P. D., Weinberger, A. J., Deleuil, M., & Bouret, J.-C. 2006, Nature, 441, 724
Robinson, R. D., Linsky, J. L., Woodgate, B. E., & Timothy, J. G. 2001, ApJ, 554, 368
Robrade, J., & Schmitt, J. H. M. M. 2005, A&A, 435, 1073
Slavin, J. D., & Frisch, P. C. 2002, ApJ, 565, 364
Smith, K., Güdel, M., & Audard, M. 2005, A&A, 436, 241
Smith, R. K., Brickhouse, N. S., Liedahl, D. A., & Raymond, J. C. 2001, ApJ, 556, L91
Song, I., Weinberger, A. J., Becklin, E. E., Zuckerman, B., & Chen, C. 2002, AJ, 124, 514
Strubbe, L. E., & Chiang, E. I. 2006, ApJ, 648, 652
Williams, R. J., Mathur, S., Nicastro, F., & Elvis, M. 2007, ApJ, 665, 247
Wilms, J., Allen, A., & McCray, R. 2000, ApJ, 542, 914
Wood, B. E., Redfield, S., Linsky, J. L., Müller, H.-R., & Zank, G. P. 2005, ApJS, 159, 118
Zuckerman, B., Song, I., Bessell, M. S., & Webb, R. A. 2001, ApJ, 562, L87

Part III

Conclusion

10. Summary and Outlook

Star formation is a particularly interesting epoch in the life of a star. It determines virtually all later stages and has a wealth of observable phenomena.

10.1 Summary

The observations presented in this thesis concern stellar sources of different evolutionary stages and demonstrate the power of X-ray observations for the study of individual aspects of the star formation process. From the evolutionary perspective, the work covers the range from Class 0-I protostars to WTTS. My summary starts with the youngest protostars observed in this thesis and subsequently proceeds to the older ones.

10.1.1 The early stages of stellar evolution

In ch. 5 the second nearest high-mass star forming region Cep A was analyzed for X-ray emission from protostars and from shocks associated with their powerful outflows. The objects in this region are in a very early stage of their stellar evolution, and their emission is strongly absorbed. Therefore, radio and infrared observations are the only other wavelength ranges allowing to study these objects. However, their additional information mostly does not suffice to unambiguously assign the X-ray emission to a protostar or jet shocks. This is particularly true for HW 2 which is the central and most massive object in this region and which remained undetected in X-rays. This high-mass ($M \approx 15\,M_\odot$) protostar possesses a high-velocity jet emanating perpendicular to its circumstellar disk (see recent results by Torrelles et al. 2011). Moreover, we found two X-ray sources at opposite locations precisely along its jet axis. Whether the X-ray emission indeed pertains to jet shocks or rather traces young stellar objects remains unclear. We also found several other X-ray emitting sources with luminosities above roughly $L_X \gtrsim 10^{30}\,\mathrm{erg\,s^{-1}}$ and relatively high plasma temperatures, i.e., consistent with an activity level in line with their most active but more evolved counterparts. Furthermore, we detected a new point-like X-ray source whose position matches the jet axis of HH 168 better than any other source in the region and which might therefore be the driving source of HH 168. The final result of our analysis is a consistent scenario of this region including the nature of the radio sources and the X-ray sources.

10.1.2 Protostellar jets

Jets from deeply embedded sources

The massive HH object 168 is located in the vicinity of the Cep A star forming region. X-ray emission from this object was discovered in an XMM-Newton observation. In ch. 6 we analyzed the first $Chandra$ observation of this object. Our analysis clearly revealed the diffuse character of the X-ray emission, albeit with individual concentrations of X-ray emission roughly related to radio sources and Hα peaks within the HH object. We showed that the X-ray emission with a temperature of $kT \approx 0.6\,\mathrm{keV}$ is not located close to the current bow shock but displaced against the outflow direction towards the driving source. The total X-ray luminosity of $L_X \approx 1.7 \times 10^{30}\,\mathrm{erg/s}$ stayed constant between the two available X-ray observations. We derived minimum plasma densities of $n_e \approx 1\ldots10\,\mathrm{cm^{-3}}$ depending on which part of the X-ray emission is considered. These low densities allow long radiative cooling times. We therefore discussed several scenarios possibly leading to the observed morphology as the current position of the X-ray emission probably does not indicate ongoing shocks. We concluded that the X-ray emission is remnant of internal shocks which happened earlier in the outflow history. The required high velocity outflow component might stem from episodic events ejecting high velocity blobs. Recent observations with the *Spitzer* satellite show emission lines from highly ionized species indicating a similar hot plasma component located close to the X-ray emission (Green et al. 2011). Their findings confirm our derived X-ray morphology.

The second protostellar jet analyzed for the nature of the X-ray emission is HH 154. In contrast to HH 168, the driving source is known to consist of a multiple system with at least two protostars of sub-solar masses. Our third epoch observation was intended to investigate the temporal evolution of this X-ray emission. The two available observations indicated X-ray emission continuously coming from the region closest to the driving sources with the most apparent differences at larger distances. Our detailed analysis of the X-ray emission of HH 154 presented in ch. 7 indeed showed that the total X-ray luminosity of HH 154 is constant over almost one decade without any significant change in the inferred plasma temperature of about $kT \approx 0.6\,\mathrm{keV}$. We find that the position of the majority of the X-ray emission appears stationary and that the trend of decreasing photon energy with increasing distance to the driving source also persists. We compared the trend in the mean photon energy to the evolution of the absorbing column density along the jet and showed that the X-ray emitting plasma is cooler at larger distances to the driving sources. While the stationary appearance can in principle be mimicked by the superposition of individual knots, we find that a standing shock more naturally explains the observations. Observations at other wavelengths show that the majority of the X-ray emission is located close to the region where collimation apparently takes place, which further strengthens our suggestion that a standing shock is responsible for the X-ray emission.

Jets from further evolved sources

The classical T Tauri star DG Tau drives an energetic X-ray emitting jet. The X-ray emission located outside of the stellar PSF was detected by Güdel et al. (2005) and further analyzed in Güdel et al. (2007b, 2008). The unusual X-ray spectrum extracted around the stellar position consists of a hot strongly absorbed component and a weakly absorbed soft component, which led Güdel et al. (2005) to suggest that this emission is also related to the jet. This suggestion is supported by the different temporal behavior of both central X-ray components (Güdel et al. 2007b). Our detailed analysis of the photon positions of this inner X-ray emission component presented in ch. 8 reveals a small but significant offset of $0.2''$ between the soft and the hard X-ray photons. Furthermore, the offset was aligned with the jet axis and persists over the two years of observations. The latter point, confirmed by the new $Chandra$ Large Program devoted to the study DG Tau's X-ray emission, is of particular interest as it is not compatible with simple models predicting that individual knots are ejected, shock-heated and moving along the jet axis. Therefore, the nature of this inner X-ray emission complex is still not clear. However, the apparent similarity with HH 154 led us to conclude that some kind of base or collimation shock is responsible for the continuous heating to X-ray emitting temperatures (see ch. 7). This conclusion is supported by the rather similar appearance of both jets in high resolution [Fe II] observations. Nevertheless, the investigation of this phenomenon is ongoing, and I will return to this topic in the outlook.

Protostellar jets summary

It seems that, at least observationally, two different types of X-ray emission from these jets exist:

1. Concentrated, but possibly still extended X-ray emission close to the driving source. This emission appears stationary over years without the proper motion usually observed for the optical knots. The luminosity of this inner X-ray emission almost rivals that of faint protostars ($\log L_X \sim 28\ldots29$).

2. Diffuse X-ray emission co-spatial with emission of cooler plasma , located at larger distances from the driving source(s). New results indicate that this component shows proper motion.

While the origin of the latter X-ray emission is consistent with shock heating by an episodic outflow component with a very high velocity, this is not obvious for the first kind of X-ray emission. Nevertheless, it might be true as well.

10.1.3 The circumstellar environment of young stars

The gaseous disk around CTTS vanishes in the course of their evolution towards the main sequence, and WTTS possess only very little circumstellar gas. This gas, however, is extremely important for the structure of the disk as well as for the dynamics of grains and, therefore, also for the formation of planetesimals. Thus, it is of special interest to measure the gas content within the disks around WTTS. In contrast to the detection of the excess IR emission from the grains, the detection of the gas is not an easy task because its intrinsic emission is faint. For edge-on disks, absorption spectroscopy can be used. X-ray absorption spectroscopy is sensitive to the gas and small grains content of the absorber and in principle also able to reveal its chemical composition. AU Mic represents the prime – and probably the only feasible – target for an X-ray absorption study of a debris disk. AU Mic is close to the sun, is X-ray bright *and* possesses an edge-on disk. Our analysis of AU Mic's X-ray spectrum presented in ch. 9 shows that the upper limit on the amount of gas in the line of sight is $N_H \lesssim 3 \times 10^{19}\,\mathrm{cm}^{-2}$. We can also pose an upper limit on the carbon content of the disk of about $N_C \lesssim 10^{18}\,\mathrm{cm}^{-2}$. These values are consistent with results from other wavelength ranges and in particular, approximately similar to UV H_2 absorption measurements. On the other hand, this result complements other measurements as it is sensitive not only to H_2 but to all atoms in the line of sight, given that the atoms are not locked into bodies larger than a few tenth of a μm. Therefore, it represents a stringent upper limit on the gas/small-grain content of the disk. While the sizes and the dynamics of the grains in the disk are not directly assessable, our result strongly points towards a disk dominated by destructive grain-grain collisions. The debris of these collisions is then expelled from the system, and the inner part of the disk is almost devoid of small grains and gas.

10.2 Outlook

The use of X-rays for the study of phenomena associated with star formation is widespread.

Debris disks and X-rays

With the currently available instrumentation, the application of X-ray absorption spectroscopy to the edge-on debris disk of AU Mic (see ch. 9) will probably not experience further improvements. Increasing the exposure time will not significantly increase the sensitivity to the column density. Furthermore, additional suitable targets are not available. On the other hand, it might be possible to use X-ray scattering by dust grains in the disk to investigate the structure of debris disks. However, this seems problematic for AU Mic as the detection of dust scattering usually requires column densities of $N_H > 10^{21}\,\mathrm{cm}^{-2}$. Such a value is ruled out by our analysis by two orders of magnitude. The analysis of debris disks, however, is extremely important to understand the evolution and formation of planetary systems. It is currently not clear what causes the inner disk clearing: Is it due to the formation of large bodies in the disk, is it due to evaporation (X-rays) or is it due to other processes? The study of these phenomena will likely proceed by infrared observations as the contrast between disk and star is largest in this wavelength range. Programs like GAS in Protoplanetary Systems (GASPS with the $Herschel$ satellite, Mathews et al. 2010) or Cores to Disks (c2d Lahuis et al. 2007) address the evolution from gaseous disks to dusty disks.

X-rays from protostars

X-ray emission of young stellar objects is an active field of research and has already proven to provide deep insights into magnetic activity of protostars such as the ubiquitous hard X-rays emission. This emission is probably associated with a small scale magnetic field and potentially early dynamo action. Surveys of star forming regions, such as the $Chandra$ Orion Ultra Deep Project (COUP, Getman et al. 2005) and the XMM-Newton Extended Survey of the Taurus molecular cloud (XEST, Güdel et al. 2007a), provided a virtually complete census of T Tauri stars and associated CCD spectra. The knowledge of X-ray and also magnetic properties of younger Class 0/I sources is less profound. As indicated in sect. 1.3 the highest accretion rates are expected during the earliest evolutionary stages. However, these epochs are also characterized by a dense circumstellar environment which hampers the observation of soft X-rays probably associated with the accretion process or jet emission. Hunting for serendipitous X-ray emission from these objects is biased towards objects with low absorbing column densities. An unbiased sample of the X-ray emission properties of protostars including Class 0-I objects is currently not within reach. Nevertheless, X-ray studies of very young star forming regions such as Cepheus A (ch. 5) continue to detect early protostars in X-rays. This may eventually address the evolution of the X-ray properties in the early evolutionary stages without volume complete samples.

X-rays from protostellar jets

Some of the work in this thesis is devoted to the nature of soft X-ray emission from protostellar jets. A particularly missing ingredient are near-simultaneous observations in other wavelengths ranges. The jet evolution within a timeframe of a few years makes a comparison with these complementary observations complicated as they were usually obtained too long before the X-ray observations. Therefore, a more detailed picture will evolve if all observations are performed within a reasonably short time span. Such studies are just beginning with the observations of DG Tau ranging from IR to X-rays within about one year. The interpretation of the recent X-ray data of DG Tau in the context of the new observations in other wavelength ranges is ongoing. We have obtained PMAS data[1] of DG Tau shortly before the new $Chandra$ observations and I have already begun with their analysis. Moreover, I have successfully applied for new HST FUV observations scheduled for spring 2011. Further X-ray observations of apparently stationary but jet related X-ray sources will show whether the apparent stationary character of the X-ray emission close to the driving source indeed represents a special class of X-ray emission from protostellar jets.

Furthermore, we have just obtained new $Chandra$ X-ray data of HH 2, the first detected X-ray emitting HH object, and I will begin with their analysis as soon as possible. This observation will constrain the temporal evolution of the X-ray emission in a comparable way as multi-epoch observations have for the optical part of the jet emission. This will allow to address the heating mechanism of the X-ray emitting plasma.

Mid/Far-IR Spitzer observations of the Cep A star forming region revealed the presence of many lines tracing plasma of similar temperature as the X-ray emission (Green et al. 2011). Further steps into this direction may avoid the problem of absorption that observations of soft X-rays suffer from.

Concluding this work, I am confident that further investigation of the X-ray emission from protostellar jets will, firstly, reveal a more precise understanding of the heating process and, secondly, that this knowledge will allow to precisely locate the origin of the associated high-velocity component. The highest outflow velocities pertain the innermost part of the star-disk system. Therefore, it is reasonable to assume that the ultimate cause of the protostellar X-ray emission is related to the inner region where stellar and disk magnetic fields might interact.

[1] Integral field spectroscopy between 6000 Å and 7000 Å.

Bibliography

Getman, K. V., Flaccomio, E., Broos, P. S., et al. 2005, ApJS, 160, 319

Green, J. D., Watson, D. M., Bergin, E., et al. 2011, ApJ, 726, L1+

Güdel, M., Briggs, K. R., Arzner, K., et al. 2007a, A&A, 468, 353

Güdel, M., Skinner, S. L., Audard, M., Briggs, K. R., & Cabrit, S. 2008, A&A, 478, 797

Güdel, M., Skinner, S. L., Briggs, K. R., et al. 2005, ApJ, 626, L53

Güdel, M., Telleschi, A., Audard, M., et al. 2007b, A&A, 468, 515

Lahuis, F., van Dishoeck, E. F., Blake, G. A., et al. 2007, ApJ, 665, 492

Mathews, G. S., Dent, W. R. F., Williams, J. P., et al. 2010, A&A, 518, L127+

Torrelles, J. M., Patel, N. A., Curiel, S., et al. 2011, MNRAS, 410, 627

Acknowledgements

I want to thank different people for their support during the course of this doctoral thesis.

First of all I want to thank my advisor Prof. Jürgen Schmitt for his advice, his encouragement and support on all questions.

Further thank to my collaborator Hans M. Günther for his contribution to my articles and proposals, his advice on various issues and for deepening my interest in protostellar jets.

I also thank Jan Robrade for all his profound advice and a very enjoyable time at the Hamburger Sternwarte and abroad; probably one of the funniest roommates one can imagine.

Further, I thank my colleagues Stefan Czesla, Sebastian Schröter and Uwe Wolter for sharing their experience and ideas.

I would also like to thank all other members of the Hamburger Sternwarte for having a nice time.

Further thank goes to my family for their loving support, especially to my sister.

Finally I thank Julia for her love, for always supporting me and for just being there.

I acknowledge support by the Deutsches Zentrum für Luft- und Raumfahrt (DLR) under grant DLR 50OR0703.